

1996

# Pattern recognition and image processing of infrared astronomical satellite images

Lun Xiong He  
*Iowa State University*

Follow this and additional works at: <https://lib.dr.iastate.edu/rtd>

 Part of the [Astrophysics and Astronomy Commons](#), [Computer Sciences Commons](#), [Electrical and Electronics Commons](#), [Environmental Monitoring Commons](#), and the [Remote Sensing Commons](#)

## Recommended Citation

He, Lun Xiong, "Pattern recognition and image processing of infrared astronomical satellite images " (1996). *Retrospective Theses and Dissertations*. 11373.  
<https://lib.dr.iastate.edu/rtd/11373>

This Dissertation is brought to you for free and open access by the Iowa State University Capstones, Theses and Dissertations at Iowa State University Digital Repository. It has been accepted for inclusion in Retrospective Theses and Dissertations by an authorized administrator of Iowa State University Digital Repository. For more information, please contact [digirep@iastate.edu](mailto:digirep@iastate.edu).

## **INFORMATION TO USERS**

**This manuscript has been reproduced from the microfilm master. UMI films the text directly from the original or copy submitted. Thus, some thesis and dissertation copies are in typewriter face, while others may be from any type of computer printer.**

**The quality of this reproduction is dependent upon the quality of the copy submitted. Broken or indistinct print, colored or poor quality illustrations and photographs, print bleedthrough, substandard margins, and improper alignment can adversely affect reproduction.**

**In the unlikely event that the author did not send UMI a complete manuscript and there are missing pages, these will be noted. Also, if unauthorized copyright material had to be removed, a note will indicate the deletion.**

**Oversize materials (e.g., maps, drawings, charts) are reproduced by sectioning the original, beginning at the upper left-hand corner and continuing from left to right in equal sections with small overlaps. Each original is also photographed in one exposure and is included in reduced form at the back of the book.**

**Photographs included in the original manuscript have been reproduced xerographically in this copy. Higher quality 6" x 9" black and white photographic prints are available for any photographs or illustrations appearing in this copy for an additional charge. Contact UMI directly to order.**

# **UMI**

**A Bell & Howell Information Company  
300 North Zeeb Road, Ann Arbor MI 48106-1346 USA  
313/761-4700 800/521-0600**



**Pattern recognition and image processing of infrared astronomical  
satellite images**

by

Lun Xiong He

A dissertation submitted to the graduate faculty  
in partial fulfillment of the requirements for the degree of  
**DOCTOR OF PHILOSOPHY**

Department: Electrical and Computer Engineering  
Major: Electrical Engineering (Communications and Signal Processing)  
Major Professor: John P. Basart

Iowa State University

Ames, Iowa

1996

Copyright © Lun Xiong He, 1996. All rights reserved.

**UMI Number: 9635322**

---

**UMI Microform 9635322  
Copyright 1996, by UMI Company. All rights reserved.**

**This microform edition is protected against unauthorized  
copying under Title 17, United States Code.**

---

**UMI**  
300 North Zeeb Road  
Ann Arbor, MI 48103

**Graduate College  
Iowa State University**

**This is to certify that the doctoral dissertation of**

**Lun Xiong He**

**has met the dissertation requirements of Iowa State University**

Signature was redacted for privacy.

**Major Professor**

Signature was redacted for privacy.

**For the Major Department**

Signature was redacted for privacy.

**For the Graduate College**

**DEDICATION**

*To my parents with love*

*and*

*To Boyun with love*

## TABLE OF CONTENTS

<b>DEDICATION</b> . . . . .	iii
<b>LIST OF TABLES</b> . . . . .	viii
<b>LIST OF FIGURES</b> . . . . .	x
<b>ACKNOWLEDGMENTS</b> . . . . .	xvii
<b>ABSTRACT</b> . . . . .	xix
<b>CHAPTER 1. INTRODUCTION</b> . . . . .	1
Introduction . . . . .	1
Why Can Infrared Detect Low Temperature Objects? . . . . .	2
Infrared Astronomical Satellite (IRAS) Mission . . . . .	4
Cirrus Emission . . . . .	8
<b>CHAPTER 2. IRAS MORPHOLOGICAL FILTER DESIGN (EARLY</b>	
<b>VERSION)</b> . . . . .	13
The ASB Sieving Process . . . . .	18
Reconstruction of Original Image from the Growth Maps . . . . .	20
Cirrus Characterization and Removal . . . . .	23
Generalization of method . . . . .	25
Some Problems with the Filter Design . . . . .	27

<b>CHAPTER 3. SELF-CONSISTENT FILTER DESIGN USING CLASSIFICATION</b> . . . . .	<b>29</b>
Introduction . . . . .	29
Classification in General . . . . .	30
K-means Method . . . . .	33
The procedure . . . . .	33
Fractional norm . . . . .	34
Entropy . . . . .	36
Relations between the entropy and fractional norm . . . . .	38
Cirrus Characterization by K-means Method . . . . .	39
Classification with the growth not modified . . . . .	41
Classification with growth partially normalized along the growth layer . . . . .	46
Approximate Linearity of Sieving Process . . . . .	48
Method of One-Type-of-Cirrus . . . . .	52
Equal CI area method revisited . . . . .	52
Non-overlapping method . . . . .	58
Multi-Cirrus Filtering . . . . .	62
Automated Adjustment of Partial Normalization Factor . . . . .	64
Reliability of the Sources Detected from the Filtering . . . . .	71
Reliability of the Shape for a Source . . . . .	72
Summary . . . . .	77
<b>CHAPTER 4. GRANULOMETRY AND UNI-DIRECTIONAL SIZE INFORMATION EXTRACTION</b> . . . . .	<b>82</b>
Structuring Element Decomposition . . . . .	82

Granulometry . . . . .	83
Uni-directional Size Information Extractors . . . . .	88
<b>CHAPTER 5. GENERALIZED HIT-OR-MISS TRANSFORM AND RELATED NON-LINEAR FILTERS . . . . .</b>	<b>94</b>
Parameterized Erosion and Closing . . . . .	95
Generalized (dynamic) hit-or-miss transform . . . . .	96
$\gamma$ -erosion and $\gamma$ -closing . . . . .	97
Parameterized Gray-scale Erosion and Closing . . . . .	103
The $\gamma$ -Sieving Process and Bi-directional SIEs . . . . .	107
<b>CHAPTER 6. WAVELET ANALYSIS . . . . .</b>	<b>111</b>
Continuous Wavelet Transform . . . . .	113
Semi-continuous Wavelet Transform . . . . .	116
Discrete Wavelet Transform . . . . .	117
Size Information Extraction by Continuous Wavelet . . . . .	118
Scaling Functions . . . . .	120
<b>CHAPTER 7. WAVELET SIZE INFORMATION EXTRACTORS</b>	<b>123</b>
Cirrus Characterization and Removal . . . . .	124
Other Extraction Methods Using Wavelets . . . . .	131
Iterative wavelet . . . . .	133
Predictive wavelet . . . . .	136
<b>CHAPTER 8. JUSTIFYING SIZE INFORMATION EXTRACTORS</b>	<b>140</b>
Linearity of Size Information Extractor . . . . .	141

Spatial Discrimination of SIE . . . . .	145
Orthogonality of SIEs . . . . .	148
<b>CHAPTER 9. SUMMARY AND FUTURE WORK . . . . .</b>	<b>150</b>
Summary of Major Contribution . . . . .	150
Future Work . . . . .	165
<b>APPENDIX A. SET THEORY AND MATHEMATICAL MOR-</b>	
<b>PHOLOGY . . . . .</b>	<b>166</b>
<b>APPENDIX B. FLUXES AND <i>FWHMS</i> FOR THE POINT AND</b>	
<b>SLIGHTLY EXTENDED SOURCES BY VARIOUS METHODS</b>	<b>187</b>
<b>BIBLIOGRAPHY . . . . .</b>	<b>193</b>

## LIST OF TABLES

Table 3.1:	The overall deviation for different classes . . . . .	46
Table 3.2:	The population of Class 1 when partially normalized using different parameters . . . . .	47
Table 3.3:	The eigenvalues of the resemblance matrix and overall resem- blance using different partial normalization factors . . . . .	47
Table 3.4:	The CI area ratio with morphology method . . . . .	56
Table 9.1:	The errors for the fluxes and FWHMs of the point and slightly extended sources determined by various methods . . . . .	165
Table B.1:	The fluxes and FWHMs of the point and extended sources after filtering Figure 3.5 using Gaussian SEs with equal CI area method. The row and column format of the table follows the row and column grid structure of the source in Figure 3.5	188
Table B.2:	The fluxes and FWHMs of the point and extended sources af- ter filtering Figure 3.5 using Gaussian SEs with non-overlapping method . . . . .	189

<b>Table B.3:</b>	<b>The fluxes and FWHMs of the point and extended sources after filtering Figure 3.5 using Gaussian SEs with multi-cirrus filtering . . . . .</b>	<b>189</b>
<b>Table B.4:</b>	<b>The fluxes and FWHMs of the point and extended sources after filtering Figure 3.5 using hemispherical SEs with equal CI area method . . . . .</b>	<b>190</b>
<b>Table B.5:</b>	<b>The fluxes and FWHMs of the point and extended sources after filtering Figure 3.5 using cylindrical SEs with equal CI area method . . . . .</b>	<b>190</b>
<b>Table B.6:</b>	<b>The fluxes and FWHMs of the point and extended sources after filtering Figure 3.5 using Gaussian SEs with sequential sieving . . . . .</b>	<b>191</b>
<b>Table B.7:</b>	<b>The fluxes and FWHMs of the point and extended sources after filtering Figure 3.5 using normal wavelet method . . . .</b>	<b>191</b>
<b>Table B.8:</b>	<b>The fluxes and FWHMs of the point and extended sources after filtering Figure 3.5 using iterative wavelet method . . .</b>	<b>192</b>
<b>Table B.9:</b>	<b>The fluxes and FWHMs of the point and extended sources after filtering Figure 3.5 using predictive wavelet method . .</b>	<b>192</b>

## LIST OF FIGURES

Figure 1.1:	The energy distribution of a black-body with $T = 10,000K$ .	3
Figure 1.2:	The Infrared Astronomical Satellite . . . . .	5
Figure 1.3:	The focal plane of IRAS . . . . .	6
Figure 1.4:	IRAS images of field I363: (a) $\lambda = 12 \mu m$ ; (b) $\lambda = 25 \mu m$ ; (c) $\lambda = 60 \mu m$ ; and (d) $\lambda = 100 \mu m$ . . . . .	10
Figure 2.1:	The image of ISSA field I029 at $\lambda = 100\mu m$ . . . . .	19
Figure 2.2:	Several growth maps of the image in Figure 4.1: structuring elements (a) between widths 5 and 7 pixels; (b) between 15 and 17 pixels; (c) between 25 and 27 pixels; and (d) between 35 and 37 pixels . . . . .	21
Figure 2.3:	Reconstructed image using step weighting function with: (a) $K = 2$ ; (b) $K = 4$ ; (c) $K = 8$ ; and (d) $K = 16$ . . . . .	24
Figure 2.4:	The average cirrus growth . . . . .	25
Figure 2.5:	The equal CI area method . . . . .	27
Figure 2.6:	The image of Figure 2.1 filtered by the ASB filter . . . . .	28
Figure 3.1:	The differences between $1/k$ norm and $k$ -norm . . . . .	36
Figure 3.2:	The entropy maximizes at $d1 = d2 = 0.5$ . . . . .	37

Figure 3.3:	The areas for different classes using morphology shown in white: (a) Class 1; (b) Class 2; (c) Class 3; and (d) Class 4 . . . . .	42
Figure 3.4:	The growths for five classes using morphology, the error bars represent standard deviation . . . . .	43
Figure 3.5:	The image of ISSA field I029 at $\lambda = 100 \mu m$ superposed at 16 locations (white dots in a square grid format) with: (a) point source (FWHM = 4.20 arc minutes); and (b) extended source (FWHM = 7.49 arc minutes) . . . . .	51
Figure 3.6:	The filtered results using equal CI area method of: (a) Figure 2.1; (b) Figure 3.5(a) ; and (c) Figure 3.5(b) . . . . .	55
Figure 3.7:	The non-overlapping method . . . . .	60
Figure 3.8:	The filtered image of Figure 2.1 using the non-overlapping method . . . . .	61
Figure 3.9:	The filtered image of Figure 2.1 using multi-cirrus filters . . .	65
Figure 3.10:	The distribution of population of different classes for field I029 with $\beta = 0, 0.25, 0.5, 0.75,$ and $1.0$ . . . . .	67
Figure 3.11:	The distribution of population of different classes for field I390 with $\beta = 0, 0.25, 0.5, 0.75,$ and $1.0$ . . . . .	68
Figure 3.12:	The filtered images of ISSA field I390 with $\beta$ as: (a) 0.25; (b) 0.5; (c) 0.75; and (d) 1.0 . . . . .	70
Figure 3.13:	The point source at the position of Dwingeloo 1 (framed at the center) . . . . .	73
Figure 3.14:	The filtered result of field I363 using equal CI area method .	74

Figure 3.15: The POSS plate containing the dust finger in IRAS field I363 75

Figure 3.16: A square-like source (a) superposed on I029 to obtain (b) . . 78

Figure 3.17: The filtered result of Figure 3.16(b) by equal CI area method 79

Figure 3.18: An ellipse-like source (a) superposed on I029 to obtain (b) . . 80

Figure 3.19: The filtered result of Figure 3.18(b) by equal CI area method 81

Figure 4.1: Granulometry: (a) hemispheric structuring elements; and (b) cylindrical structuring elements . . . . . 85

Figure 4.2: Classification results of sieving processes with: (a) hemispheric SEs; and (b) cylindrical SEs . . . . . 86

Figure 4.3: The filtered image of Figure 2.1 with hemispheric structuring elements using the equal CI area method . . . . . 87

Figure 4.4: The filtered image of Figure 2.1 with cylindrical structuring elements using the equal CI area method . . . . . 89

Figure 4.5: The growths of different classes of sequential sieving process . 92

Figure 4.6: The filtered image of Figure 2.1 by sequential sieving process, Gaussian SEs, equal CI area method, and sigmoidal noise weighting . . . . . 93

Figure 5.1: Illustrations of  $\mathcal{E}_\gamma$  with  $\gamma = 1^-, 0.5$  and  $0^+$ : (a) letter  $X$  represents the set  $X$ , circle  $B$  represents the structuring element; (b)  $\mathcal{E}_{1^-}(X, B)$  which is actually erosion; (c)  $\mathcal{E}_{0.5}(X, B)$ ; and (d)  $\mathcal{E}_{0^+}(X, B)$  which is the same as dilation . . . . . 99

Figure 5.2: An image from the IRAS database: (a) original; and (b) corrupted by spike noise . . . . . 105

**Figure 5.3:** The  $\gamma$ -erosion of Figure 5.2(b) with a  $3 \times 3$  flat structuring element: (a)  $\gamma = 0^+$ ; (b)  $\gamma = 1/9$ ; (c)  $\gamma = 3/9$ ; and (d)  $\gamma = 4/9$  109

**Figure 5.4:** The  $\gamma$ -closing of Figure 5.2(b) with a  $3 \times 3$  flat structuring element: (a)  $\gamma = 0^+$ ; (b)  $\gamma = 1/9$ ; (c)  $\gamma = 3/9$ ; and (d)  $\gamma = 4/9$  110

**Figure 6.1:** The dilated version of a function  $(1 - x^2)e^{-x^2/2}$  with  $b = 0$ , and  $a = 0.5, 1$ , and  $2$  . . . . . 115

**Figure 6.2:** The Fourier transform of dilated version of function  $(1 - x^2)e^{-x^2/2}$  with  $b = 0$ , and  $a = 0.5, 1$ , and  $2$  . . . . . 116

**Figure 6.3:** The illustrations of  $|\hat{\phi}_{-1}|^2$ ,  $|\hat{\Phi}_1|^2$ , and  $H_i$  with  $i = -1, 0$ , and  $1$  122

**Figure 7.1:** Several size information maps of the image in Figure 2.1 using the wavelet transform: (a) between  $i = 2$  and  $3$ ; (b) between  $i = 6$  and  $7$ ; (c) between  $i = 10$  and  $11$ ; and (d) between  $i = 15$  and  $16$  . . . . . 125

**Figure 7.2:** Reconstructed images using step function with: (a)  $K = 4$ ; (b)  $K = 8$ ; (c)  $K = 12$ ; and (d)  $K = 16$  . . . . . 126

**Figure 7.3:** The areas for different classes using wavelet: (a) Class 1 and 2 shown as white area; (b) Class 3 shown as white; (c) Class 4 shown as white; (d) Class 5 shown as white . . . . . 129

**Figure 7.4:** The growths for five classes using the wavelet transform . . . 130

**Figure 7.5:** The filtered image of Figure 2.1 using multi-cirrus filtering with the wavelet method . . . . . 132

**Figure 7.6:** The growths for five classes using iterative wavelet . . . . . 134

Figure 7.7:	The filtered image of Figure 2.1 using multi-cirrus filtering with iterative wavelet method . . . . .	135
Figure 7.8:	The growths for five classes using predictive wavelet . . . . .	138
Figure 7.9:	The filtered image of Figure 2.1 using multi-cirrus filtering with predictive wavelet method . . . . .	139
Figure 8.1:	A prototype peak $f(x) = -k x $ . . . . .	142
Figure 8.2:	Accumulative size information by various extractors at $x = 0$	144
Figure 8.3:	Differential size information by various extractors at $x = 0$	144
Figure 8.4:	Differential size information by various extractors at $x = 10$	146
Figure 8.5:	Accumulative size information represented spatially by various extractors . . . . .	147
Figure 8.6:	Differential size information represented spatially by various extractors . . . . .	147
Figure 9.1:	The image of ISSA field I029 at $\lambda = 100\mu m$ . . . . .	154
Figure 9.2:	The filtered results of Figure 9.1 using equal CI area method	155
Figure 9.3:	The filtered results of Figure 9.1 using non-overlapping method	156
Figure 9.4:	The filtered results of Figure 9.1 using multi-cirrus filtering method . . . . .	157
Figure 9.5:	The filtered image of Figure 9.1 with hemispheric structuring elements using the equal CI area method . . . . .	158
Figure 9.6:	The filtered image of Figure 9.1 with cylindric structuring elements using the equal CI area method . . . . .	159

Figure 9.7: The filtered image of Figure 9.1 by sequential sieving process, Gaussian SEs, equal CI area method, and sigmoidal noise weighting . . . . . 160

Figure 9.8: The filtered image of Figure 9.1 using multi-cirrus filtering with the normal wavelet method . . . . . 161

Figure 9.9: The filtered image of Figure 9.1 using multi-cirrus filtering with the iterative wavelet method . . . . . 162

Figure 9.10: The filtered image of Figure 9.1 using multi-cirrus filtering with the predictive wavelet method . . . . . 163

Figure A.1: Operations between sets  $A$  (solid-lined rectangle) and  $B$  (dashed-lined rectangle): (a)  $A \cap B$  (shaded); (b)  $A \cup B$  (shaded); (c)  $A^c$  (whole set is  $E$ , the dashed-lined rectangle; result is shaded); and (d)  $A - B$  (shaded) . . . . . 169

Figure A.2: Translation, homothetic and reflection of sets. The origin  $0$  is denoted as  $0$ ,  $X_h$  is the translation of  $X$  by  $h$ ,  $\tilde{X}$  is the reflection of  $X$ , and  $2Y$  is the homothetic of  $Y$  with a factor of 2 . . . . . 171

Figure A.3: Hit-or-miss transform of  $X$  (dashed lined) with structuring elements  $B = (B^1, B^2)$  (shaded). The result is shown as solid lines . . . . . 172

Figure A.4: Erosion (a) and dilation (b) of  $X$  by  $B$ . The results are shown as solid lines,  $X$  as shaded area . . . . . 174

**Figure A.5:** (a) Homothetic of  $X \ominus B$  (small dotted-lined circle) by a factor  $\lambda$  (small solid-lined circle) is equivalent to homethetic of  $X$  and  $B$  followed by erosion; and (b) dilation of  $X$  by  $B \oplus \check{B}'$  (solid lines) is equivalent to dilation by  $B$  (dotted lines) and then dilation by  $B'$  (solid lines) . . . . . 177

**Figure A.6:** A photograph of composite material . . . . . 179

**Figure A.7:** The  $W$  fibers (circles) are painted black . . . . . 180

**Figure A.8:** Figure A.7 is thresholded . . . . . 180

**Figure A.9:** Using opening to remove small particles . . . . . 181

**Figure A.10:** Subtraction of Figure A.8 by Figure A.9 to obtain voids . . . 182

**Figure A.11:** Applying opening on Figure A.10, we remove circular traces of  $W$  fibers . . . . . 182

**Figure A.12:** Top-surface (a) and umbra (b) transforms of set  $X$  . . . . . 184

**Figure A.13:** Gray-scale erosion (a) and dilation (b) of  $f(x)$  by  $g(x)$  . . . . 186

## ACKNOWLEDGMENTS

At the time finishing my dissertation, I feel that I owe a “thank you” to many people. These people are academic and research advisors, academic colleagues, friends in my personal life, and my beloved ones.

First of all, I thank Professor Alan I. Goldman. Without his help, I wouldn't have the opportunity to come to Iowa State University. He has always helped me when I needed him. I thank my academic advisors Professor John P. Basart and Professor Philip N. Appleton, for their patient guidance. I especially thank Professor Appleton for his friendship, and for the help he has given to my family. I also thank Dr. Jeffrey A. Pedelty, for his FORTRAN codes. Without them, I would have spent many more hours on MasPar computer programming. I thank Dr. Vassilis Charmandaris for many helps on IRAF and MasPar. I thank Joe Eitter, for showing me equipment at Fick Observatory. Thanks are also due Joseph Metzger, for his help with the MasPar parallel computers.

My dissertation would not be completed without thanking the encouragement from my friends: Cheng Tang, Wenhua Huang, Guoxin Xie, Bei Zhang, Qiming Li, Xiaosha Wang, Stephan Kycia, Xia Hua, Feng Lu, and Lei Zhang. Special thanks are due Qiming Li, for reading and criticizing an early version of this dissertation, and for his valuable suggestions. I really learned from them that *a friend in need*

*is a friend indeed.* Also, I would like to thank my colleagues, Bing Wang, Sheng-Fa Chuang, and Sung-Chi Tsou, for beneficial discussions with them, especially Bing Wang for the discussion about wavelets.

I can not forget my committee, for so many times I bothered them about the schedules for preliminary and final examinations, especially to Professor Noel Cressie. I thank Professor Noel Cressie, Professor Jennifer Davidson, Professor Julie Dickerson, and Professor Satish Udpa, for their suggestions made during both preliminary and final examinations, for their patience with my rescheduling the examinations so many times.

Without mentioning NASA, this dissertation would not be complete. Because of the financial support from NASA, I am able to complete this project. I thank Eva Kinstle for doing my Letter of Intent so many times, for her prompt notification when each Letter of Intent was to expire. I also thank the secretaries from both the departments of Electrical Engineering, and Physics & Astronomy, to Pam Myers, Linda Clifford, Wilma Bucklin, Patsy Wisecup, Lori Hockett, Joyce Smith, Erlene Mooney, Shirley Calhoun, Danhong Yang, and Sam-Kiang Chang.

I also thank IPAC-JPL for letting me use their database NED for searching extragalactic sources.

Thanks are due to my wife, Boyun, for her encouragement and patience in all these years and due to my parents, for their encouragement always. I also thank my sisters and their families for all their support.

**ABSTRACT**

The Infrared Astronomical Satellite (IRAS) images with wavelengths of  $60 \mu m$  and  $100 \mu m$  contain mainly information on both extra-galactic sources and low-temperature interstellar media. The low-temperature interstellar media in the Milky Way impose a “cirrus” screen of emission in IRAS images, especially in images with  $100 \mu m$  wavelength. This dissertation deals with the techniques of removing the “cirrus” clouds from the  $100 \mu m$  band in order to achieve accurate determinations of point sources and their intensities (fluxes). We employ an image filtering process which utilizes mathematical morphology and wavelet analysis as the key tools in removing the “cirrus” foreground emission. The filtering process consists of extraction and classification of the size information, and then using the classification results removal of the cirrus component from each pixel of the image. Extraction of size information is the most important step in this process. It is achieved by either mathematical morphology or wavelet analysis. In the mathematical morphological method, extraction of size information is done using the “sieving” process. In the wavelet method, multi-resolution techniques are employed instead.

The classification of size information distinguishes extra-galactic sources from cirrus using their averaged size information. The cirrus component for each pixel is then removed by using the averaged cirrus size information. The filtered image

contains much less cirrus. Intensity alteration for extra-galactic sources in the filtered image are discussed. It is possible to retain the fluxes of the point sources when we weigh the cirrus component differently pixel by pixel. The importance of the uni-directional size information extractions are addressed in this dissertation. Such uni-directional extractions are achieved by constraining the structuring elements, or by constraining the sieving process to be sequential.

The generalizations of mathematical morphology operations based on the dynamic hit-or-miss transform are presented in this dissertation. The generalized erosion ( $\gamma$ -erosion) bridges traditional erosion and dilation. It also enriches the morphological operators available in the field of signal and image processing. Traditional closing is generalized into  $\gamma$ -closing, which bridges traditional closing and opening. Properties of  $\gamma$ -erosion and  $\gamma$ -closing are discussed. The sieving process is generalized based on  $\gamma$ -closing, and is bi-directional, with the polarity directly related to the parameter  $\gamma$ . The size information extractors of morphological methods and wavelet methods are justified quantitatively using a prototype peak with fixed slope. The non-linearity of the sieving process is analyzed. It is shown that the sieving process can approach an approximate linearity at positions where the input signal has sharp peaks (i.e., the slopes are large). The spatial discriminating properties of the size information extractors are also very important.

## CHAPTER 1. INTRODUCTION

### Introduction

Infrared radiation plays a very important role in astronomy for its outstanding ability to detect low temperature objects [Allen 1975]. In 1983, the US, UK, and Netherlands jointly launched the first infrared telescope (Infrared Astronomical Satellite; for short IRAS) [Neugebauer 1984a; 1984b] capable of mapping the sky at infrared wavelengths between 12 and  $100\mu m$ <sup>1</sup>. The IRAS mission successfully recorded data over 96% of the sky. The 12 and 25  $\mu m$  data contain information mainly on stars in our galaxy (Milky Way). However, the IRAS data with wavelengths 60 and 100  $\mu m$  contain information on extra-galactic sources, nebulae, and low temperature interstellar media in the Milky Way. The low temperature interstellar media in our own galaxy impose a “cirrus” screen of emission onto the data [Low *et al.* 1984]. The cirrus emission is most serious in the galactic plane, at a wavelength of 100  $\mu m$ . This emission has hampered the studies of faint extra-galactic sources, therefore, a technique to remove the screening effects of cirrus is desired.

---

<sup>1</sup> $1\mu m = 10^{-6}m$

## Why Can Infrared Detect Low Temperature Objects?

Infrared radiation was first observed by Sir William Herschel when he studied the amount of heat transferred by different colored light in the spectrum of visible light [Allen 1975]. It has a wavelength ranging from 1  $\mu m$  to 1  $mm$  which is longer than that of the visible light.

All material emits electromagnetic radiation at all frequencies by virtue of temperature, but this radiation usually is not in thermal equilibrium. Thus, the distribution of energy density with respect to the frequency or wavelength is related to the temperature of the material (if it has uniform temperature) and the composition, geometry, and other properties of the material. Because of these affecting factors, the analysis of the thermal radiation is quite complicated. To simplify the problem, physicists suggested a model in which the radiation is related to the temperature only. This model is the black-body radiation.

If we consider the radiation within an opaque enclosure with the walls maintained at a uniform temperature  $T$ , the radiation and walls would reach thermal equilibrium. To study the radiation inside, one cuts a small hole in the wall of the enclosure. If this hole is very small, the equilibrium inside the enclosure is not significantly disturbed. This is the well-known black-body problem [Elliott 1993; Allen 1975].

For black-body radiation, the distribution of energy density per unit volume at interval  $[\lambda, \lambda + d\lambda]$  at temperature  $T$  is

$$\rho(\lambda, T) d\lambda = \frac{8\pi hc}{\lambda^5} \cdot \frac{1}{e^{hc/\lambda k_B T} - 1} d\lambda. \quad (1.1)$$

where  $c = 2.998 \times 10^8$   $m/s$  is the speed of light in vacuum,  $k_B = 1.381 \times 10^{-23}$   $J \cdot K^{-1}$ , the Boltzmann constant.

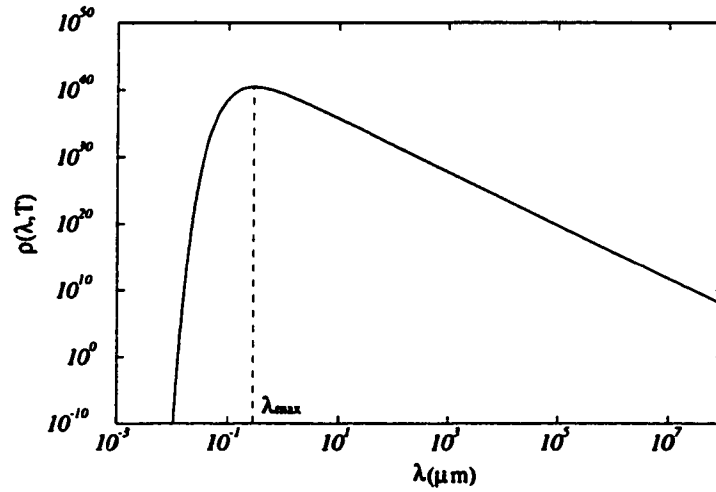


Figure 1.1: The energy distribution of a black-body with  $T = 10,000K$

Figure 1.1 shows a typical view of the plot of  $\rho(\lambda, T)$  versus  $\lambda$ . This distribution is zero when wavelength is zero or infinity. It has a maximum at some wavelength  $\lambda_{max}$ . Note that the scales in Figure 1.1 are logarithmic. If linearly scaled, it is easy to see that the energy radiated is concentrated around  $\lambda_{max}$ . The parameter  $\lambda_{max}$  is an indicator of the temperature  $T$ , because they are related by

$$\lambda_{max}T = 2898 \mu m \cdot K. \quad (1.2)$$

Therefore, if a black-body has low temperature,  $\lambda_{max}$  would be longer. For a black-body with temperature of 290 K, the radiation peaks around a wavelength of 10  $\mu m$ . For a black-body with temperature of 29 K, the radiation peaks at 100  $\mu m$ .

Usually, a star has a temperature between 3,000 K and 10,000 K [Allen 1975; Kaufmann 1978]. By the relation in Equation (1.2), we know that the radiation from black-bodies with temperatures of stars is concentrated from 0.3  $\mu m$  to 1  $\mu m$ , i.e., in the visible light region. Compared to the discussion in the last paragraph, we see

that far-infrared (such as a wavelength of  $100\ \mu\text{m}$ ) is able to detect low temperature black-bodies.

Of course, the objects in the universe are not really blackbodies. Nevertheless, infrared radiation detected is mainly from low-temperature objects. During the night, if the sky is clear, our eyes sense the dominating visible light from the shining stars. With an infrared telescope, however, we see emission more from the objects with lower temperatures.

### **Infrared Astronomical Satellite (IRAS) Mission**

The Infrared Astronomical Satellite (IRAS, see Figure 1.2 for its photograph) launched in 1983 [Neugebauer *et al.* 1984a; 1984b; Beichman *et al.* 1988] was originally designed to perform a reliable survey of the entire sky in the infrared. But it turned out to be a more successful mission than expected. It discovered new comets, asteroids, protostars, galaxies, far-IR emitting stars, interstellar dust, star formation, interacting galaxies, quasar formation, and so on [David and Dooling 1984; Neugebauer *et al.* 1984b].

The success of IRAS can be viewed from its design, data collection, on-board processing, ground processing, and so on [Beichman *et al.* 1988; Wheelock *et al.* 1994a]. The design of IRAS is discussed in detail in *IRAS Catalogue, Volume 1, Explanatory Supplement* [Beichman *et al.* 1988]. The observations were carried out by a focal plane assembly which consisted of infrared and visible detectors, cold detectors and associated masks, filters and field optics. Figure 1.3 shows the layout of the focal plane assembly, with the detectors shown as rectangles. The number above each detector is the index. The focal plane assembly has 62 infrared and 8



Figure 1.2: The Infrared Astronomical Satellite

visible channels. The infrared detectors were further divided into 8 modules. Each module belongs to one of the four color bands (with wavelengths of 12, 25, 60, and 100  $\mu m$ ). Each color band has two modules. For more information, please refer to Beichman *et al.* [1988].

The signals from the detectors were then pre-amplified, processed, and transferred to spacecraft on-board computer. The data were then stored in the spacecraft and later transmitted to a ground station. The data processing includes nuclear pulse circumvention circuitry [Emming *et al.* 1983] which removes sharp pulses caused by cosmic rays and charged particles hitting the detector, additional amplification, low-pass filters to limit frequency response and reduce high-frequency noise, and digitization using a 16-bit analog to digital converter. The digitized data were further sampled at 16, 16, 8, and 4 Hz at 12, 25, 60, and 100  $\mu m$ , respectively. In order to save storage space in the spacecraft, the data were transformed into the difference between successive 16-bit values of the scan. The transformed data were further compressed into 8-bit values.

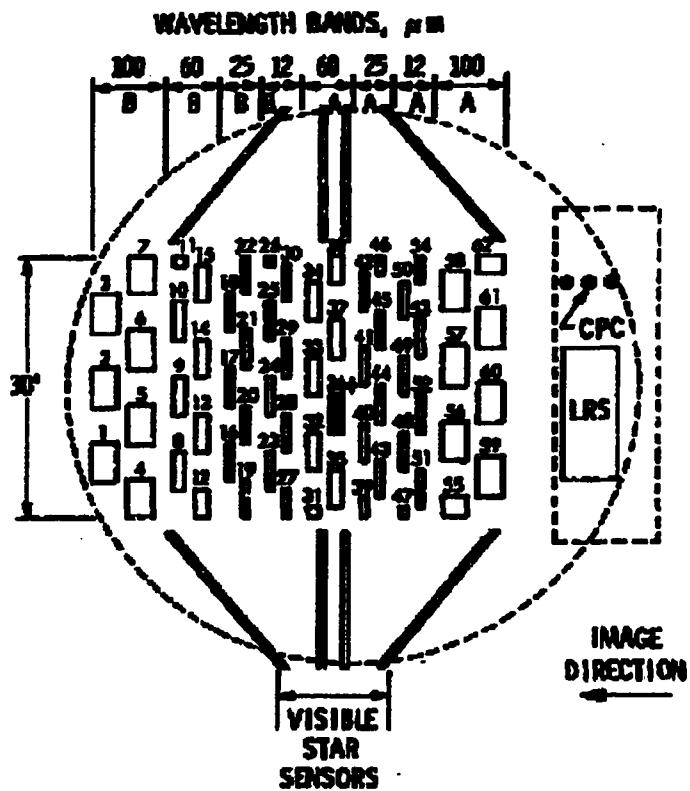


Figure 1.3: The focal plane of IRAS

To obtain accurate maps of the total sky brightness, observations of diffuse emission by IRAS needed to be free of background due to local objects such as Sun and Earth shines, satellites flying nearby, planets in the Solar System, asteroids, and comets. Such effects were separated from the data by multiple detections of the same distant sky through different regions of the Solar System. Multiple observations were also able to remove particle radiation.

Multiple observations included seconds-confirmation, hours-confirmation, and weeks-confirmation. Point sources and small extended sources detected with zero-sum square-wave filters [Beichman *et al.* 1988] went through seconds-confirmation by checking whether at least another detector in the same color band had the same detection. A successful seconds-confirmation detection then went through hours-confirmation. A successful hours-confirmation resulted in a refined position and a refined flux for each band where possible. A successful hours-confirmation went through weeks-confirmation, which resulted in a refined position for the source.

Together with the IRAS Point Source Catalog, IPAC (Infrared Processing Analysis Center) released an original extended emission atlas, named SkyFlux, before 1988. SkyFlux images gave a view of infrared emission with high angular resolution and high sensitivity. In the process of producing IRAS original products, large improvements in sensitivity and photometric accuracy were obtained. The IRAS Sky Survey Atlas (ISSA) was the result of the improved process [Wheelock *et al.* 1994a, 1994b].

ISSA was obtained by selecting high-quality data meeting criteria based on observing conditions and performance of individual detectors. Weighted averages of the data were used to mosaic data from multiple survey scans of the same region into

single digital images. Consistency between the scans of hours-confirming coverage was checked by human scanning of different images. Significantly discrepant data were removed from the image.

The data in the image was corrected for the effects of the transfer function of the telescope, transferred to relative photometric units, corrected for the zodiacal foreground, and destriped of the detector effects (such as its transfer functions). This procedure produced images with high sensitivity. The ISSA was designed to give relative intensity, rather than absolute intensity. Therefore, care needs to be taken when attempting absolute flux calculation. For details about how to calibrate relative flux into absolute flux, please refer to [Rieke *et al.* 1985; Beichman *et al.* 1988].

ISSA contains images for 430 fields, each with a size of  $500 \times 500$  pixels at  $1.5'$  per pixel, i.e., the field size is  $12.5^\circ \times 12.5^\circ$ . Each field has four bands, and each band has four images, with three of them being Hours CONformation images (HCON-1, HCON-2, and HCON-3), and the fourth one being the coadded image by the previous three (HCON-0). The total number of the images in ISSA is 6880. In this dissertation, we dedicate our work to the study of “infrared cirrus”, and do not deal with the algorithm for coadding the HCON images. Thus, only coadded images are used. In most of the cases, we show images at  $100 \mu m$  since we are most interested in the cirrus in that band.

### Cirrus Emission

“Infrared cirrus” is due to the thermal emission of the interstellar dust from within the Solar System and from within the Milky Way [Low *et al.* 1984]. The

name was taken from the cirrus clouds on the Earth because of the similarity of their morphologies. The astronomical cirrus clouds impose a screening foreground on our view toward objects outside the Milky Way. It hampers the study of object identification and flux measurements of extra-galactic objects. The cirrus emission is more serious at far-infrared regions (60 and 100  $\mu m$ ). Figure 1.4 shows the field I363 at wavelengths of 12, 25, 60, and 100  $\mu m$ , centered at a galactic latitude of  $-15.38^\circ$ , and a galactic longitude of  $96.43^\circ$ . Note that the images at 12 (Figure 1.4(a)) and 25  $\mu m$  (Figure 1.4(b)) contain negligible cirrus emission. However, the images at 60 and 100  $\mu m$  have very serious cirrus contaminations.

Some cirrus clouds are positionally associated with the concentration of gas and dust [Low *et al.* 1984]. Some cirrus, are cold clouds which may be new parts of the outer Solar System or new structures within the interstellar medium [Low *et al.* 1984]. The dust is more concentrated in the Galactic plane, producing much stronger infrared emission there. About two thirds of the energy radiated at 100  $\mu m$  in the Galactic plane comes from the diffuse medium (atomic, molecular, and ionized component), the other one third comes from well-identified luminous sources [Puget *et al.* 1987].

Analysis of the infrared cirrus has been done by many astronomers. One of the models fits a minimum of two dust components [Cox and Mezger 1987]. One component is cold dust with a temperature between 14 and 25 K, corresponding to diffuse atomic and molecular hydrogen gases. Another component is warm dust with a temperature between 30 and 50 K located in a HII region with dense cloud cores. Desert *et al.* [1988] also modeled components of hydrogen in order to search for molecular clouds.

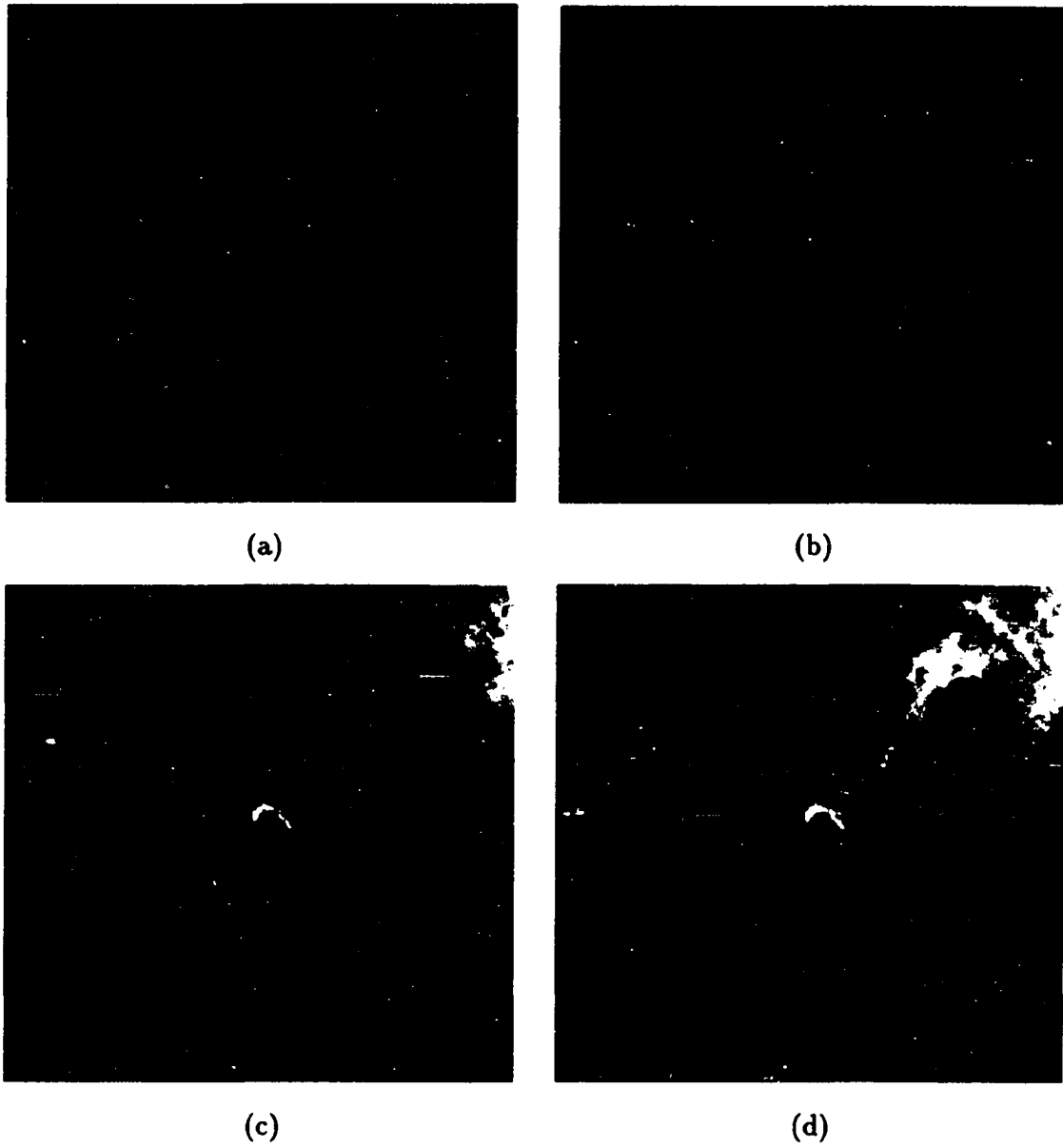


Figure 1.4: IRAS images of field I363: (a)  $\lambda = 12 \mu m$ ; (b)  $\lambda = 25 \mu m$ ; (c)  $\lambda = 60 \mu m$ ; and (d)  $\lambda = 100 \mu m$

Estimation of the cirrus components was also made by means of image processing techniques. A morphological filter based on a “sieving” process was proposed and implemented by Appleton, Siqueira, and Basart [Appleton *et al.* 1993; Siqueira 1989]. This sieving process extracts size information using the image processing technique called mathematical morphology. Such a filter was applied to the M81 field (I414) and removed most of the cirrus from the image, leaving the point sources. This filter was further improved [He *et al.* 1994a, 1995] by incorporating classification techniques into the design, which makes the filter self-consistent for each field.

In this dissertation, I first describe in Chapter 2 the work that Appleton *et al.* had done before I joined the project. Problems of their filter design approach are discussed in detail. Then, in Chapter 3, I introduce a classification scheme (k-means) into the filter design process, such that the filter is designed based on the classification result of the size information, making the filter self-consistent. The size information extracted is pre-processed by partial normalization before classification. Such a partial normalization enables the same classification algorithm to be used for all the fields (such as fields close to the poles and fields in the Galactic plane). The intensity retention of the filtering process is also discussed. It is possible to retain the fluxes for extended sources and point sources by weighting the cirrus differently pixel by pixel, with the weight related to the closeness of the pixel to cirrus. In Chapter 4, I discuss how to limit size information to positive value, and reduce computing time using structuring element decomposition and granulometry.

In Chapter 5, more size information extractors are introduced in the form of a generalized sieving process. This generalization is based on the generalized hit-or-miss transform. First, erosion and closing are to be generalized into what I call  $\gamma$ -erosion

and  $\gamma$ -closing. The parameter  $\gamma$  lies between 0 and 1, representing the degree of its closeness to the traditional erosion and closing. The sieving process, accordingly, is generalized into  $\gamma$ -sieving. When  $\gamma$  equals 1, it extract size information from the positive direction. When  $\gamma$  equals 0, it extracts size information from the negative direction. When  $\gamma$  lies between 0 and 1, it extracts size information from both the positive and negative directions. The value of  $\gamma$  is directly related to the weight (or polarity) of the size information in the positive direction.

In Chapter 6, wavelet transform, another approach to the size information extraction, is introduced. This chapter gives a friendly guide into this somewhat-difficult-to-understand theory based on Fourier analysis. Some concepts introduced, such as scaling functions, are more general than the corresponding concepts introduced in other sources. This chapter ends with multiresolution analysis using the continuous wavelet, which we shall employ in Chapter 7. Chapter 7 deals with the size information extraction using multiresolution analysis, and its application to IRAS images. Three variates, i.e., normal, iterative and predictive wavelet methods are used. In Chapter 8, characterizations of the size information extractors are made using a fixed-slope prototype peak from the size scale and spatial scale. Also, we discuss the orthogonality between size information extractors in this chapter.

The last chapter, Chapter 9, summarizes the contributions of this dissertation, and suggests future research subjects.

## CHAPTER 2. IRAS MORPHOLOGICAL FILTER DESIGN (EARLY VERSION)

Since the IRAS mission, many processing procedures have been applied to the data. The main efforts were on the improvements of the spatial and flux resolution based on multiple scans of the same region. These include interpolation of non-uniform data followed by restoration by an entropy-based algorithm [Gonsalves *et al* 1987] to improve spatial resolution in extended sources; restoration of images of extended sources by co-addition, constrained least squares, and maximum entropy methods [Bontekoe 1990], which successfully obtained the images of M51 with spatial resolution of 45 arc seconds at  $60 \mu m$  (note that the limitation of resolution of the telescope is 1 arc minute at  $60 \mu m$ ); and maximum correlation method which produces images with spatial resolution of 36 arc seconds at  $60 \mu m$  [Aumann *et al.* 1990]. The signal with a zodiacal light background was studied also [Wheelock *et al.* 1994a], which is part of the ISSA process.

We are most concerned with the Infrared Sky Survey Atlas (ISSA) images. Before we discuss the filter design, I will give a little more information on the reliability of the data. ISSA was consistently calibrated at spatial scales larger than  $5'$ . It gives relative photometry rather than absolute photometry (as we can see in the last chapter). The uncertainty of the absolute zero point is dominated at 12 and  $25 \mu m$  by uncertainties

in the zodiacal emission model, and at 60 and 100  $\mu m$  by imperfect knowledge of the detector offsets. An uncertainty of as much as 30% at 60  $\mu m$  and 60% at 100  $\mu m$  exists in the frequency response correction, which again affects the relative intensity measurement at spatial scales of more than a few degrees. A comparison of the IRAS data with the DIRBE data from Cosmic Background Explore (COBE) shows that IRAS data give high brightness (13% and 28% high at 60 and 100  $\mu m$ ). The 60-/100- $\mu m$  color is 12% low in IRAS data relative to DIRBE data [Wheelock 1994a].

ISSA was designed to study extended structures in the survey data, it has not been optimized for accuracy for sources smaller than 5'. The images within 20° of the ecliptic plane have reduced quality due to zodiacal contamination. The residual error in this region could be 10 times larger than in non-rejected regions at 12 and 25  $\mu m$ . The residual error at higher wavelengths are smaller. Special care needs to be taken when processing images in this region. Special care was taken to remove anomalies (the satellite, debris, and asteroids, etc.), but even so, the anomalies do appear. Individual HCON images should be checked to verify unusual features in the coadded images. Artifacts resembling tails appear around point sources in ISSA images. These tails are due to photon-induced responsivity enhancement, or hysteresis effect. These tails occur near bright sources, especially at 12 and 25  $\mu m$ . The hysteresis effects also remain around bright areas (within 6°) such as the Galactic plane. The images with absolute galactic latitude larger than 50° can be mosaiced within an accuracy of 0.1 MJy sr<sup>-1</sup>. The fields with absolute galactic latitude smaller than 50° can be mosaiced with the same accuracy except in the Galactic plane and where sky join with area of absolute galactic latitude of larger than 50°. At these two locations, ISSA field boundary discrepancies of 1-2 MJy sr<sup>-1</sup> at 60  $\mu m$  and 3-5 MJy sr<sup>-1</sup> at 100

$\mu m$  can be encountered.

Appleton, Siqueira, and Basart [1993], hereafter ASB, used a morphological filter to analyze the signal in  $100 \mu m$  under cirrus foreground. I refer to this filter as ASB filter. The ASB filtering process involves a morphological sieving process which is able to extract size information from peaks. This sieving process is based on morphological opening of the image by certain structuring elements. The structure smaller than the structuring element is removed, leaving the size information larger than the SE retained. The size information for selected pixels were then chosen for further study. An averaged behavior of size information for the cirrus was then obtained by the cirrus pixels chosen. This averaged cirrus growth is then used to remove the cirrus components pixel by pixel in the image.

This dissertation discusses the continuation, improvements, and generalization of the ASB filter design. For this reason, a detailed description of the work of ASB filter is necessary. The concept of characteristic interval, however, was introduced by He *et al.* [1995]. It is used in this chapter since it simplifies the notation for the description of the calculation of cirrus components in terms of equal CI area method [He *et al.* 1995].

Mathematical morphology is a theory, based on sets, which deals with image analysis using operations capable of exploring geometric information in objects. It became a well recognized image analysis discipline since the book *Image Analysis and Mathematical Morphology* by Serra [1982] was published. The basic concepts in mathematical morphology, erosion and dilation of two sets, even can be traced back to the beginning of this century [Minkowski 1903], under the names of Minkowski subtraction and addition. Some of the material in the theory of mathematical morphology

was finished by Hadwiger [1958]. Also, Matheron published a book entitled *Random Sets and Integral Geometry* [1975] which contains the main theoretical foundation for mathematical morphology.

As an image analysis approach, mathematical morphology has been developed theoretically and applied practically in image and signal processing, pattern recognition, and computer vision with an extensive number of publications in last decade [Gader 1990; Gader and Dougherty 1991; Gader *et al.* 1992; Dougherty *et al.* 1994; Shen *et al.* 1995]. Among these publications, mathematical morphology was employed in image compression [Egger *et al.* 1995; Salembier *et al.* 1995], shape recognition [Bhattacharya *et al.* 1995], skeletonizing [Pai and Hansen 1994], pattern restoration [Schonfeld 1994], texture classification [Chen and Dougherty 1994], text string extraction [Liang *et al.* 1994], fractal dimension calculation [Maragos and Sun 1993], phonetic feature extraction [Hemdal *et al.* 1991], sampling [Heijmans and Toet 1991], and segmentation [Beucher 1990].

In mathematical morphology, an image is modeled as a set (usually in  $\mathbb{R}^n$  space, where  $\mathbb{R}$  is the real set). By way of set theory, we describe the geometry and topology of an image. Mathematical morphology utilizes a set with certain geometry and topology to explore the geometry and topology of another image. The former set is called a structuring element (SE). Different SEs extract geometry and topology information of an image quite differently. Such flexibility makes mathematical morphology suitable for solving various problems in image processing.

The basic operations of mathematical morphology are erosion and dilation. They are further combined into opening and closing. Erosion and opening remove from an image the fragments and spikes which are smaller in size than the SE. On the contrary,

dilation and closing remove from an image the hole-like and crack-like structures which are smaller than the SE. Appendix A gives a full description of these concepts, and the corresponding extensions of them into the field of gray-scale images.

The presentation in Appendix A follows that of other books. For set theory, it follows the book *Introduction to Set Theory* [Hrbacek and Jech 1978]. For theory of binary morphology, we follow the book *Image Analysis and Mathematical Morphology* [Serra 1982]. For theory of gray-scale morphology, we follow the book *An Introduction to Morphological Image Processing* [Dougherty 1992] with minor modifications. The example of a void counting problem was conducted by the present author [He *et al.* 1994b].

Opening retains structures larger than the structuring element, but removes the structures smaller than the structuring element (as seen from the void counting example in Appendix A). Supposing now we have two structuring elements with different sizes, then the difference of the opened images by these two structuring elements represents the structures with sizes in between these two structuring elements. If we have a set of SEs with increasing sizes, we obtain size information at various size scales by the subtraction of successive opened images. This process is called a sieving process. With the gray-scale morphology, the sieving process is conducted similarly. Note that the IRAS images of the 100  $\mu m$  band contain diffuse cirrus clouds, and point sources (see Figure 1.4(d)). If the sieving process is applied to an image with a set of SEs with increasing sizes, then by taking the differences of the opened images, we are able to obtain the size information for each pixel. The size information of the sharp peak will have large components when the structuring elements are small, and small components when structuring elements are large. On the contrary, the “cirrus”

clouds will have small size information when structuring elements are small, and large size information when structuring elements are large. The different behavior of the size information of cirrus and extra-galactic objects is the key to the identification of point sources, and thus the key to the removal of cirrus components.

### The ASB Sieving Process

Serra describes the general process of “sieving” which is the basis of the ASB filter design approach for exploring the various size-scales in the input image [Serra 1982]. The method is described as follows [ASB]. An input image  $I_o$  is morphologically “opened” using a sequence of increasingly larger structuring elements (SE for short)  $S_i$ ,  $i \in (1, 2, \dots)$  to produce a set of images  $O_i$  (called the opened images). The differences between  $I_o$  and  $O_i$  generates a further series of images denoted by  $M_i = I_o - O_i$  (for Morphological Output). The image  $M_i$  is a descriptor of the size information of the objects which is smaller than the  $i$ th structuring element  $S_i$ . If we difference two morphological outputs, say  $M_i$  and  $M_j$  where  $j > i$ , then the outcome  $G_{j,i} = M_j - M_i = O_i - O_j$  will be a descriptor for the objects with sizes between structuring elements  $S_i$  and  $S_j$ . The  $G_{j,i}$ ’s are the functions that we use to describe the behavior of a pixel, and thus to distinguish between the undesired cirrus noise and desired objects. We call  $G_{j,i}$  the growth between the  $i$ th and  $j$ th structuring elements. The  $G_{j,i}$  most commonly used were for  $j - i = 1$ . If we have a total of  $N$  SEs, then the largest SE is  $S_N$ .  $G_{j+1,j}$ ,  $j = 1, 2, \dots, N - 1$ ,  $(I_o - O_1)$  (extremely small structure), and  $O_N$  (extremely large structure) are adequate for the reconstruction of the original image [see Appleton *et al.* 1993].

To illustrate how the sieving process extracts size information from an image, we

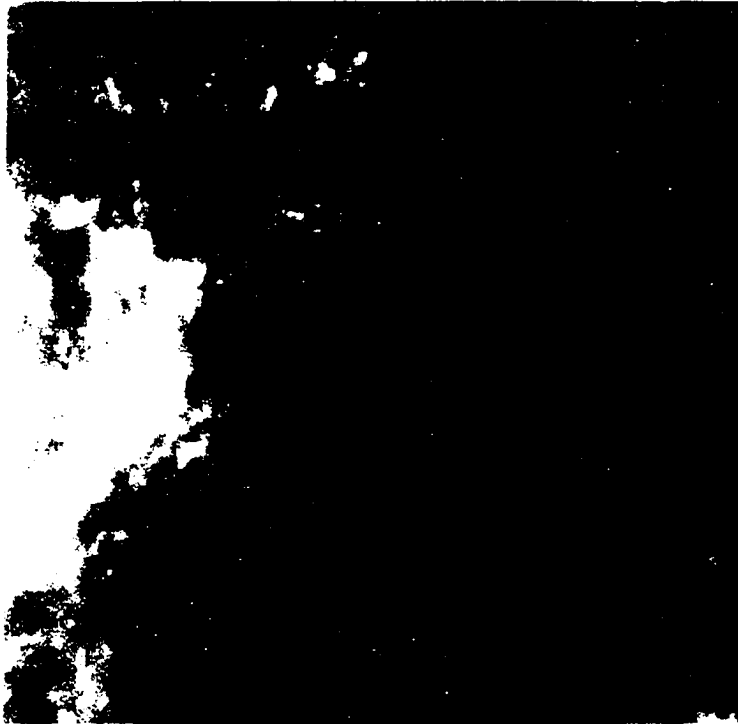


Figure 2.1: The image of ISSA field I029 at  $\lambda = 100\mu m$

choose an image which is severely contaminated by cirrus for experiment. Figure 2.1 is the field I029 in ISSA, which has galactic latitude  $-27.12^\circ$  and galactic longitude  $269.13^\circ$ . This field was chosen somewhat arbitrarily, but it turned out to be a pretty good test image as we will see in later chapters. This field has very strong cirrus, but it has point sources too which are not very strong. Although strong, the cirrus has similar morphology all over the field. This makes it possible to remove the cirrus by just using one filter.

We applied openings to the image shown in Figure 2.1 using circular Gaussian-shaped structuring elements of height 10 with widths between 5 and 39 pixels increasing in 2-pixel steps for the next larger structuring elements. The standard deviation

of the Gaussian function  $\sigma$  is dependent on the size of the SE (for step  $i$ , the SE is  $S_i$ ), and equals  $k \cdot i$  with  $k = 0.8494$ . Using the sieving process described, we calculate the growth  $G_{j,i}$ . Figure 2.2 shows several of the growth maps of Figure 2.1.

Figure 2.2(a) shows the growth between structuring elements with widths 5 and 7 pixels, Figure 2.2(b) between widths 15 and 17 pixels, Figure 2.2(c) between widths 25 and 27 pixels, and Figure 2.2(d) between widths 35 and 37 pixels. It is obvious that the structures which grow in intensity on small-scales are extracted from the growth of smaller structuring elements and those with growths on larger scales are extracted when the structuring elements are equivalently large. The growth images are stacked together to form a cube. The third dimension of the cube is called the growth layer. The reasons for the formation of the cube are that the sum of all the growth maps, extremely small structures, and extremely large structures form the original image (see next section), and by examining the cube along the vertical direction, we may obtain the growth behavior of a pixel. For pixels of the point sources, the growths are larger when SEs are small, and small when the SEs are large. For the cirrus pixels, however, the growth behavior is different. Appleton *et al.*'s paper [1993] shows some of the growth of cirrus pixels in the M81 field. The growths of cirrus pixels have various shapes, but they all have small growth when SEs are small.

### Reconstruction of Original Image from the Growth Maps

As discussed by ASB, the original image can be reconstructed from growths if extremely small and extremely large size information were taken into consideration. The extremely small size information is  $(I_o - O_1)$ , and extremely large size information is  $O_N$ , were mentioned in last section. Putting the growths together by addition, the

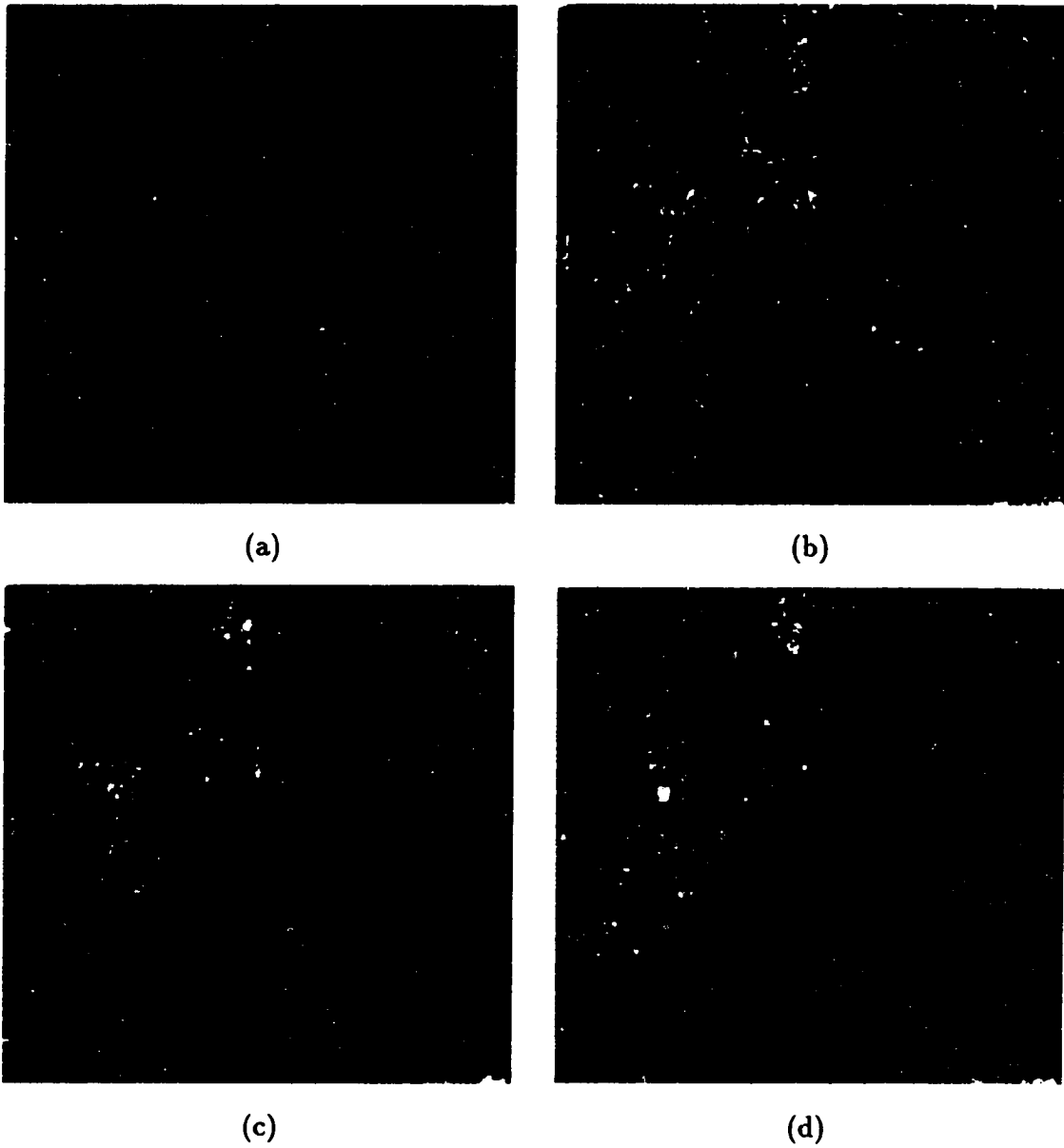


Figure 2.2: Several growth maps of the image in Figure 4.1: structuring elements (a) between widths 5 and 7 pixels; (b) between 15 and 17 pixels; (c) between 25 and 27 pixels; and (d) between 35 and 37 pixels

original image can be obtained, i.e.,

$$I_o = \sum_{j=1}^{N-1} G_{j+1,j} + (I_o - O_1) + O_N. \quad (2.1)$$

As what the ASB filtering implies, and what I think, a filtering process in general occurs by calculating the output based on modified growth maps. Simple cases of filtering is done by weighting the growth maps differently before the addition in Equation (2.1) takes place. Such a weight is not necessarily constant for all the pixels in the growth maps, therefore, a general weight image  $W_j$  for the growth  $G_{j+1,j}$  is employed. Thus, the filtering produces an output image by the following equation,

$$I = \sum_{j=1}^{N-1} W_j \cdot G_{j+1,j} + W_0(I_o - O_1) + W_N O_N. \quad (2.2)$$

An example of the filter is a binary function with weight 1 for certain growth layers, and 0 for other layers. For instance, the following weight function extracts size information smaller than the SE  $S_{K+1}$ ,

$$W_j = \begin{cases} 1, & j \leq K, \\ 0, & j > K. \end{cases} \quad (2.3)$$

When  $K$  increases, the filtered image by the above equation contains more larger sized structures. Figure 2.3 shows some of the filtered images using the binary weight function. This filter gives good filtering of point sources for some values of  $K$  (such as shown in Figure 2.3(a) and 2.3(b)). When  $K$  is small, the filter is good for strong point source identification. The intensity of the point sources obtained this way are not reliable. For instance, the fluxes of the a point source (pixel position [146, 307], i.e., Galactic latitude of  $-24.33436^\circ$  and Galactic longitude of  $268.01695^\circ$ ) in Figure 2.3(a), (b), (c), and (d) are reduced to 0.66, 0.80, 0.90, and 1.0 that of the original

flux, respectively, compared with the original image. Also, the faint sources seen in the original image cannot be seen when  $K$  is very small. The cirrus can merely be seen in the filtered image especially when  $K$  is small. The cirrus intensity in Figure 2.3(a), (b), (c), and (d) are reduced to  $10^{-5}$ , 0.006, 0.026, and 0.100, that of the original cirrus intensity, respectively.

### Cirrus Characterization and Removal

The filtering process described in the last section is simple, and it works on identification of strong point sources. Faint point sources observed easily in Figure 2.1 are very weak in Figure 2.3(a). They become stronger in Figure 2.3(b), but it appears that the cirrus components (filament structures) begin to show up there. Therefore, it is necessary that we find the weight image  $W_j$  which is more related to the information of cirrus growth. This motivates the pattern search for the average cirrus growth. ASB sieved the coadded image of M81 field from IRAS survey CRDD data dearchived from the IRAS database at the NASA-JPL Infrared Processing and Analysis Center (IPAC). The data has an image scale of 1 arcmin = 1 pixels, and the intensity scale of the image is in MJy/St. By examining unprocessed IRAS field M81 and comparing it to the optical fields of the same region, they selected 44 pixels which are definitely in well-defined cirrus regions. The growth of each pixel was plotted versus the growth layer without  $(I_o - O_1)$  and  $O_N$  into consideration (with  $N = 17$ ). The growth is further normalized by dividing the growths by the total sum of the growths of each pixel. The sum of the growth for certain layers was termed area for these layers in ASB filter design. The normalized growth profiles for the 44 pixels were then averaged to obtain the mean cirrus growth. Figure 2.4 shows the

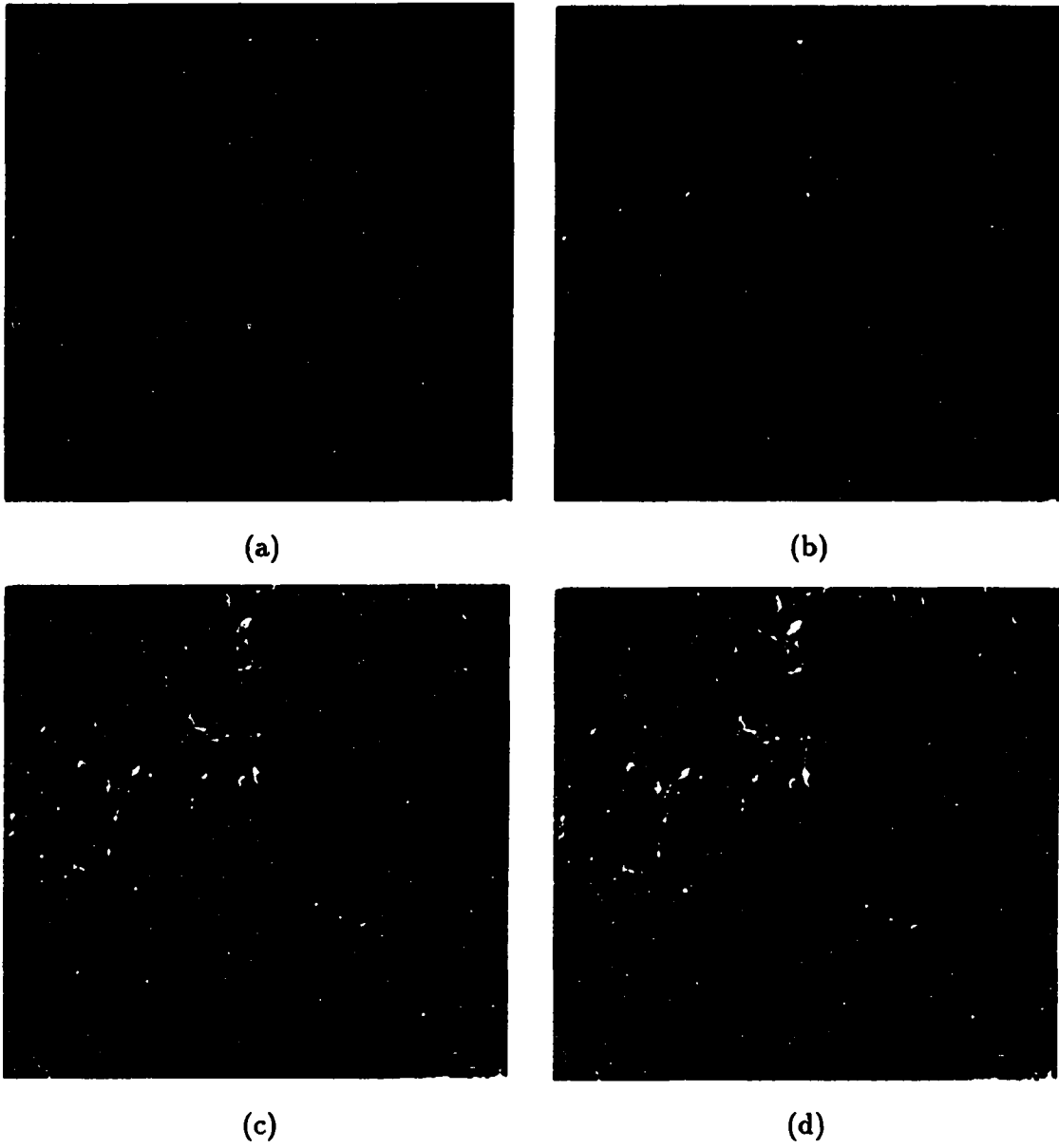


Figure 2.3: Reconstructed image using step weighting function with: (a)  $K = 2$ ; (b)  $K = 4$ ; (c)  $K = 8$ ; and (d)  $K = 16$

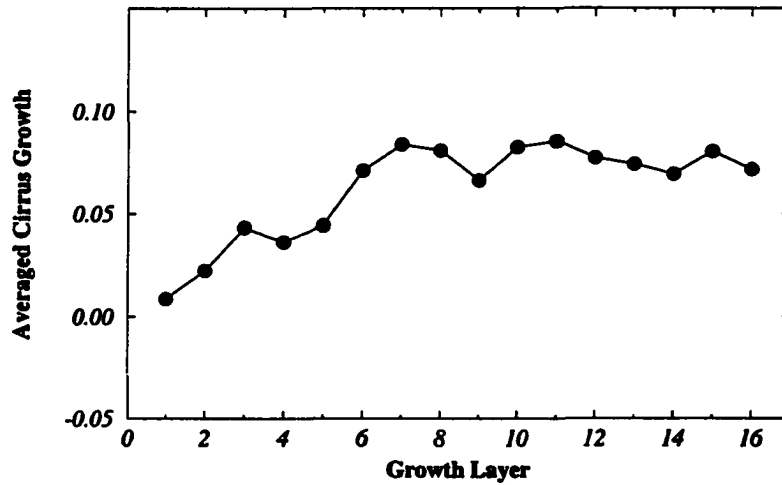


Figure 2.4: The average cirrus growth

mean growth of the 44 cirrus pixels chosen from M81 field.

### Generalization of method

In order to remove cirrus components from the growth cube, pixel by pixel, using this mean cirrus profile, the ASB filter assume that for each pixel, the cirrus components have the same normalized growth. Of course, this assumption is too simple. It can not deal with cases when multiple types of noises (such as cirrus) are the problem. A method I have developed which deals with the multiple cirrus situation would improve the results. In the experiments,  $G_{j+1,j}, j \in (1, 2, \dots, N-1)$  were grouped together to form a cube with the index  $j$  identifying the growth layer. Therefore the layers of the growth cube form a set  $L = [1, 2, \dots, N-1]$ , where  $N$  denotes the maximum index of the structuring elements for the opening process. The growth on the  $j$ th layer equals  $G_{j+1,j}$ . The characteristic interval (CI, as introduced by He *et al.* [1995] after I join this project) is defined to be a subset of the growth layer set

$L$ . For instance,  $N = 17$  in our experiment, and the interval  $L_1 = [8, 9, \dots, 13]$  is a subset for  $L$ . Similarly, the subsets  $L_2 = [1, 2, 3]$  and  $L_3 = [14, 15, 16]$  are subsets of  $L$ , thus  $[L_2, L_3]$  form a characteristic interval for  $L$  also.

The filtering starts with finding the cirrus CI, i.e., some CI in which the point sources and cirrus have very different normalized area. For each pixel in the growth cube, the cirrus component is proportional to mean cirrus growth with a scaling factor  $k_{i,j}$ . Let  $F_l, l \in L$  be the cirrus mean growth, then the scaling factor is,

$$k_{i,j} = \frac{\sum_{l \in CI} G_{l+1,l}^{(i,j)}}{\sum_{l \in CI} F_l}, \quad (2.4)$$

where  $G_{l+1,l}^{(i,j)}$  is the growth at pixel  $[i, j]$  of the  $l$ th layer. This method was later called the equal CI area method by He *et al.* [1995]. Figure 2.5 is an illustration of this method. The thick line is the growth for a pixel, the thin line is the scaled filter coefficients. Note the areas in CI for both lines are equal. With the scaling factor, the cirrus components are then deducted from the growth for the corresponding pixel. Applying this process to all the pixels in the image, we obtain a modified growth cube. The summation of the new growth cube along the growth layer direction and the extremely small structures ( $I_0 - O_1$ ) gives the filtered result.

The above filtering process was applied to the M81 field, giving a filtered result containing much less cirrus fragments (for more details, see ASB). The intensity of the cirrus in the filtered image is reduced by a factor of approximately 15 in comparison with the original image, which is quite successful. The filter is also able to preserve the extended sources in the image. These results demonstrated the power of ASB filter in the problem of cirrus removal.

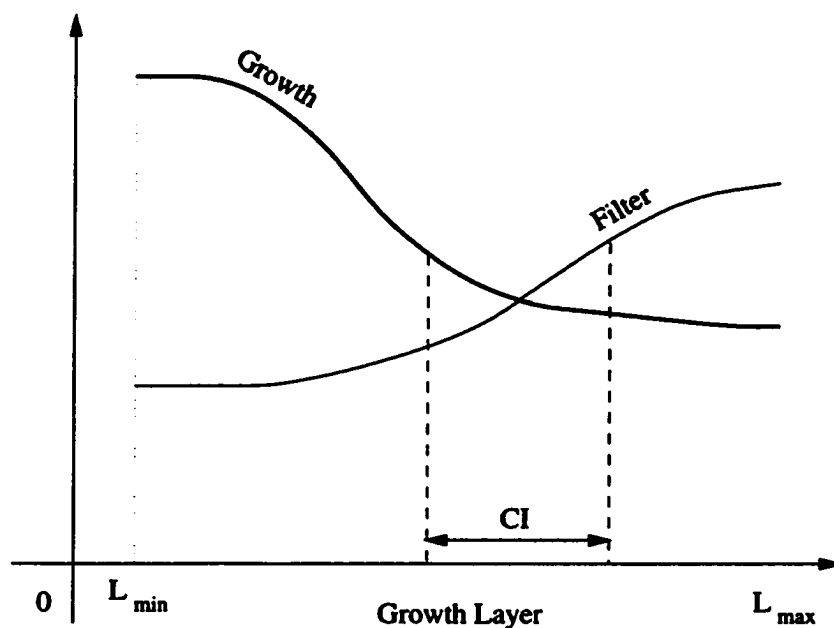


Figure 2.5: The equal CI area method

### Some Problems with the Filter Design

As stated in last section, the cirrus pixels used to calculate the mean cirrus growth by ASB were chosen by eye. This certainly is time consuming, and we might also think the selection is biased. Secondly, CI was chosen by a trial-and-error method, there is no algorithm to relate the growths with this interval. Therefore, when processing other fields, it takes lots of time to figure out a proper CI. Thirdly, it is difficult to consider multiple cirrus behavior in this filter design process. Fourthly, this filter may not work well in other fields. For instance, I applied this filter to the I029 field, giving the filtered image shown in Figure 2.6 (CI = [4, 5, ..., 12]). Note some of the dark areas in the filtered image, these are due to the over-subtraction of the cirrus components from these pixels. It is true that each field has different

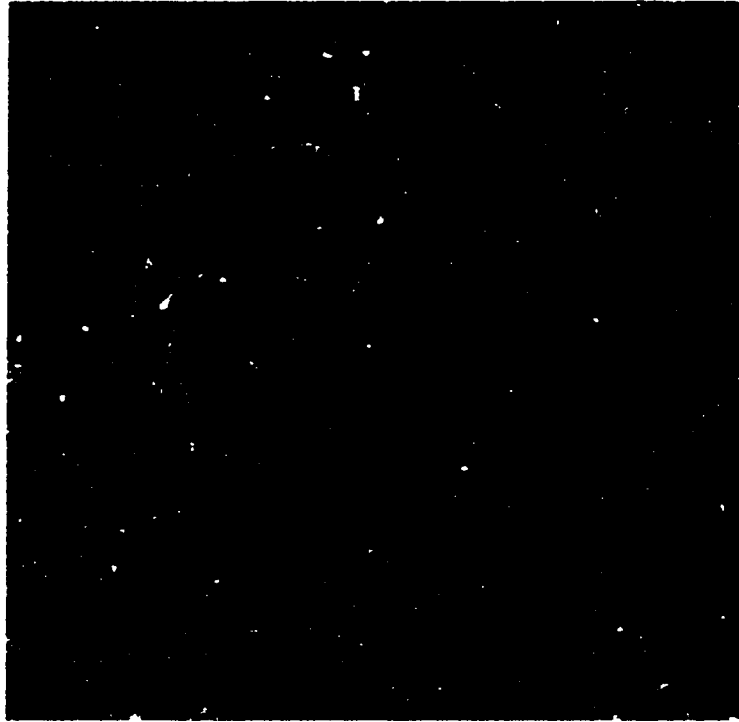


Figure 2.6: The image of Figure 2.1 filtered by the ASB filter

cirrus growth behavior, therefore, it is necessary to define the filter consistent with the cirrus growth of the same field. It is hard, however, to go through the filter design described above for all the 430 fields. A method to reduce the human supervision and to extend the method suitable for multiple cirrus categories is required. Such an idea motivated our incorporating classification schemes into the filtering process described above. This is the subject of the next chapter.

## **CHAPTER 3. SELF-CONSISTENT FILTER DESIGN USING CLASSIFICATION**

### **Introduction**

As described in the last chapter, it is desired to partition cirrus pixels into several categories. This can be accomplished by the process of classification. In this chapter, concepts of classification are introduced first, followed by an example – the k-means method. The advantages and disadvantages of the k-means method are discussed. Fractional norm and entropy are used to solve the initialization problem existing in the k-means method, which is then applied to the growths for each pixel in the growth cube (for concept about the cube, see last chapter). The growths for all the categories after the classification are then plotted versus the growth layer, in order to distinguish cirrus from point sources (with the help of maps of the classes). The growths for different cirrus classes are analyzed in order to obtain a filter which will remove the right amount of cirrus from each pixel. Intensities of the point and slightly extended sources are discussed with simulated images, and an attempt to retain the correct intensity is proposed.

## Classification in General

The classification process is a decision-making one by computers or electronic devices in a narrow sense, to distinguish the decisions made by living things. In the literature, classification has meaning similar to other terms, such as recognition, decision-making, and detection [Bachelor 1974; Therrien 1989].

The classification process partitions objects into several groups, with objects *similar* to each other in the same group (or class). The term *similarity* is judged by the features of the objects that are obtained by transformations of the observations (or measurements) of the object. The process of defining the feature transformation is called feature extraction. Features of an object can be viewed as a vector, with the vectors forming a feature space. The feature vectors of objects are fed into a classifier which judges the similarities between the vectors, and group vectors similar to each other in the same group. The similarity of two vectors is usually related to the distance between them in feature space. This distance can be Euclidean distance, or other distances (for strict definition of distances, please refer to [Dunford and Schwartz 1958; Barnsley 1992; Bachelor 1974]). If the distance between the vectors is small, then they are similar to each other.

The classifier can be a device, program, or a mathematical algorithm. It can be divided into three categories based on the development approach. These categories are traditional classifiers [Bachelor 1974; Duda 1973; Therrien 1989], fuzzy logic classifiers [Pal and Majumder 1986; Yager and Zadeh 1992], and neural network classifiers [Lippmann 1987].

The foundation for the traditional classifier was laid in the 1960s and early 1970s [Bachelor 1974]. These classifiers include mainly, linear classifier,  $\phi$ -machine,

piece-wise linear classifier, nearest neighbor classifier, potential function classifier, compound classifier, k-means method, and the ISODATA method [Batchelor 1974; Therrien 1989]. The fuzzy logic classifier is based on the theory of fuzzy sets by L. A. Zadeh [Zadeh 1965]. Fuzzy logic classifiers have become a very important part in the field of artificial intelligence. The neural network was developed in the 1980s with an attempt to achieve good performance via a dense interconnection of simple computational units. Lippmann [1987] reviewed the neural network algorithms and compared them with the corresponding counterparts in the traditional classifiers.

Classifiers can also be divided into two categories based on whether the classes of any available objects are known and incorporated into the processing. If yes, the classification is called supervised, if no, the classification is called unsupervised, or clustering. Most of the classifiers are supervised. The unsupervised process is more difficult than the supervised one, since no prior information is known. K-means and ISODATA [Therrien 1989] are traditional unsupervised classifiers, and Kohonen self-organizing feature maps [Lippmann 1987] is an unsupervised neural network classifier. The ISODATA method is extended into the area of fuzzy classifiers, but usually fuzzy classifiers often used are supervised.

A classifier with a simple algorithm can be easily accomplished within a short time, however, it cannot be used in complicated classification situations. For instance, the linear classifier might be the simplest one, but it can only be used for two classes. The trade-off between the simplicity of the algorithm and classifying data in more detail is the basis for our selection of the classifiers. When two classifiers have similar algorithm complicity, they might be suitable for different cases. For instance, the k-means method and the nearest neighbor method have similar complicity

in algorithms, k-means is good for grouping objects inside spheres together, on the other hand, the nearest neighbor method is good for linking. When a classifier has a very complicated algorithm, it can deal with complicated situations, but the process would be slower.

Traditional, fuzzy, and neural net classifiers have their own advantages and disadvantages. The traditional classifiers are easier to understand, because the mathematics behind them are very clear for an average user. Their criterion functions can usually be written out explicitly, thus they can be analyzed easily. The disadvantages of the traditional classifiers are that when a complicated situation is involved, we need to make a very complicated model using the traditional approaches. The fuzzy classifiers aimed mostly at theoretic developments of the decision making models. Part of the reason why they are less applied in real situations are due to the complications of fuzzy set theory. Fuzzy logic, however, may be the best way to approach the decision making of humans. The neural nets try to use very simple computational units and vast networking between them to simulate the human decision process. One can use neural nets to make very difficult decisions with very complicated net layouts. But such complicated net layouts (parallel layouts) are not manufactured popularly yet. Using a serial computer to simulate the neural nets is inconvenient, because of many iterations and big loops involved in the simulation. Another disadvantage of a neural net is that often when the output converges, it converges to a local energy minimum (as does the Kohonen self-organizer). The neural nets, however, have their advantages over other approaches in speech and image recognition where many hypothesis are considered in parallel.

Classification has been applied in various fields, such as in business, health pro-

grams, science, engineering, and the environment. Examples are automatic readings of checks, invoices, and postal codes, automatic medical diagnosis, classification of biological species, classification of spectrum, stars, and galaxies in astronomy, classification of signals and images in many fields, pollution prevention, etc.

### **K-means Method**

Since IRAS data has many fields to be processed, an unsupervised classification in our project is desired to reduce the labor of human workers. The most often used unsupervised classifiers are the k-means method, ISODATA method, and Kohonen self-organizer. The ISODATA method is based directly on the k-means method. The Kohonen self-organizer is very much the same thing as the k-means method. If the weight update in Kohonen self-organizer is controlled properly, it will produce similar result to the k-means method. Because of these reasons, and the simple algorithm of k-means method, we choose to use the k-means method in our problem.

#### **The procedure**

The K-means method tries to classify the feature space into  $k$  regions. Each region or class has one representative, denoted as  $\vec{y}_j, j \in [1, 2, \dots, k]$ . The error of a feature vector  $\vec{x}$  is  $\|\vec{x} - \vec{y}_j\|_2^2$  ( $\|\cdot\|_2$  is the Euclidean distance), if  $\vec{x}$  belongs to class  $j$ . The objective of the k-means method is to minimize the total error with respect to all the sample feature vectors. The procedure is as follows [MacQueen 1967; Therrien 1989]:

- (1) Arbitrarily assign feature vector  $\vec{y}_j$  as representative of class  $j$ . Do this for all classes.

- (2) Assign the sample feature vectors to be class  $j$  if  $y_j$  among all the representatives of the classes is closest to the sample (judged by Euclidean distance).
- (3) Compute the mean of the samples belonging to class  $j$  to obtain a new  $\bar{y}_j$ .
- (4) Iterate (2) and (3) until the decisions for all the samples do not change between two nearby iterations.

The k-means method decreases the error at each iteration. However, it sometimes converges to some local minimum of error instead to global minimum of error. In order to solve this problem, stochastic relaxation was used [Rose *et al.* 1993]. Also, I will discuss our approach toward this problem in next section by means of fractional norm or entropy methods.

### Fractional norm

The k-means method is very sensitive to the initial assignment of the positions in the feature space. If inappropriately assigned, the iteration will converge at some local minimum instead of the global minimum of the criterion function [Duda and Hart 1973; Rose *et al.* 1993]. There are many ways to solve this problem. One is to use simulated annealing or stochastic relaxation [Geman and Geman 1984; Rose *et al.* 1993]. In our project, we do not use simulated annealing in the k-means method. Instead we use another technique called fractional norm [He *et al.* 1995]. The fractional norm method originated from the metric (or distance) between a vector and a set of vectors.

In linear algebra, the  $k$ -norm for a vector  $\vec{D} = [d_1, d_2, \dots, d_n]$  is defined by:

$$k\text{-norm: } \|\vec{D}\|_k \equiv \sqrt[k]{\sum_{i=0}^n |d_i|^k}, \quad k = 1, 2, 3, \dots \quad (3.1)$$

In a similar fashion, we define a fractional norm as follows:

$$\frac{1}{k}\text{-norm: } \|\vec{D}\|_k \equiv \left( \sum_{i=0}^n |d_i|^k \right)^k, \quad k = 1, 2, 3, \dots \quad (3.2)$$

which is an extension of the  $p$ -norms [Khalil 1992], but fails to obey the triangular inequality. In the initialization of positions of the representative for different classes in the feature space, we need to consider the metric between *one vector* and *a set of vectors*. We denote the former vector as  $\vec{P}_d$ , and the latter set as  $\vec{P}_1, \vec{P}_2, \dots, \vec{P}_n$ . Then the Euclidean distance between  $\vec{P}_d$  and  $\vec{P}_i$ ,  $i \in (1, 2, \dots, n)$  can be calculated as

$$d_i = \|\vec{P}_d - \vec{P}_i\|_2, \quad i \in (1, 2, 3, \dots, n). \quad (3.3)$$

If we form a vector based on  $d_i$  as

$$\vec{D} \equiv [d_1, d_2, \dots, d_n], \quad (3.4)$$

then we see that the 1-norm or 2-norm of  $\vec{D}$  is not a good measure for the distance between the point  $\vec{P}_d$  and  $\vec{P}_i$ ,  $i \in (1, 2, \dots, n)$ . For example, suppose we have two vectors in one-dimensional space at  $P_1 = 0$  and  $P_2 = 1$ . With  $P_d \in (0, 1)$ ,  $d_1 = P_d$  and  $d_2 = 1 - P_d$ . Thus  $\vec{D} = [P_d, 1 - P_d]$ . Now we want to find the  $P_d$  which is far from both  $P_1$  and  $P_2$ . The 1-norm  $\|\vec{D}\|_1 = 1$  which is a constant, and 2-norm  $\|\vec{D}\|_2 = \sqrt{2P_d^2 - 2P_d + 1}$  which has a maximum when  $P_d = 0$  or  $P_d = 1$ . That is not a preferred result since these points lie on top of  $P_1$  and  $P_2$ . We prefer  $P_d = 0.5$  which is far from *both*  $P_1$  and  $P_2$ . The fractional norm of  $\vec{D}$ , on the other hand better represents the distance between one vector and a set of vectors. Figure 3.1 demonstrates the differences of 1/4-norm, 1/2-norm, 1-norm and 2-norm for the case above.

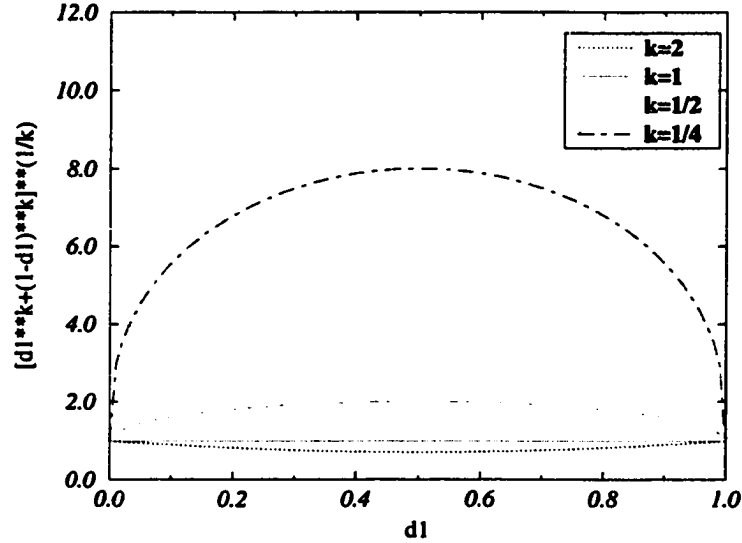


Figure 3.1: The differences between  $1/k$  norm and  $k$ -norm

## Entropy

Another way to calculate the distance between one vector and a vector set is to use the concept of *entropy* [Pratt 1991]. For a statistical process, if there are  $n$  possible events and the probability for the  $i$ th event is  $p_i$ , then we have

$$p_i > 0, \sum_{i=1}^n p_i = 1, i \in (1, 2, \dots, n). \quad (3.5)$$

The entropy is defined as:

$$H = - \sum_{i=1}^n p_i \log_2 p_i. \quad (3.6)$$

In our case, with the vector  $\vec{D}$  we can define the probabilities as:

$$p_i = \frac{|d_i|}{\sum_{i=1}^n |d_i|} = \frac{|d_i|}{\|\vec{D}\|_1}. \quad (3.7)$$

These probabilities, if plotted with respect to  $i$ , demonstrates whether the components of  $\vec{D}$  are well correlated. If they are all the same, then the entropy is maximum,

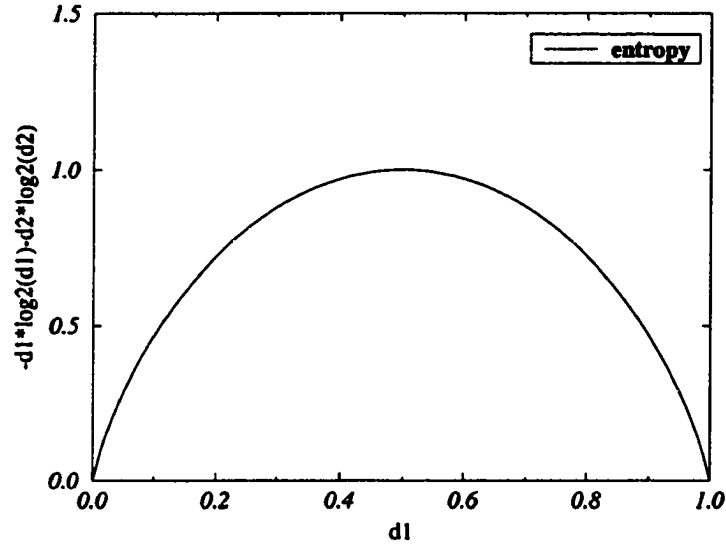


Figure 3.2: The entropy maximizes at  $d_1 = d_2 = 0.5$

implying maximum order between these components. Figure 3.2 shows the entropy for the example in previous section ( $P_1 = 0$ ,  $P_2 = 1$ ,  $P_d \in (0, 1)$ ,  $d_1 = P_d$ , and  $d_2 = 1 - P_d$ ). From the figure, we see that the entropy maximizes at  $d_1 = d_2 = 0.5$ , which is the result we desire. In a series of experiments of the  $k$ -means method, we found that using  $\|\vec{D}\|_1 H$  for adjusting the initial distance often led to a minimization of energy which is the same as that from  $1/4$  fractional norm as discussed in last section, in the final result. Therefore  $\|\vec{D}\|_1 H$  might be a good representation of the distance between the point  $\vec{P}_d$  and  $\vec{P}_i$ ,  $i \in (1, 2, \dots, n)$ .

### Relations between the entropy and fractional norm

For very large  $k$ , the  $\frac{1}{k}$  norm is closely related to the entropy. At first glance, we may find it difficult to relate the two. Now

$$\lim_{k \rightarrow \infty} \|\vec{D}\|_{\frac{1}{k}} \rightarrow \lim_{k \rightarrow \infty} (n)^k = \begin{cases} 1 & \text{for } n = 1, \\ \infty & \text{otherwise.} \end{cases} \quad (3.8)$$

thus when  $k \rightarrow \infty$ , the  $\frac{1}{k}$  norm of  $\vec{D}$  goes to  $\infty$ . If we define a normalized  $\frac{1}{k}$  norm  $\|\vec{D}\|_{\frac{1}{k}}^{normal}$  as

$$\|\vec{D}\|_{\frac{1}{k}}^{normal} \equiv \left( \frac{\sum_{i=1}^n |d_i|^{\frac{1}{k}}}{n} \right)^k. \quad (3.9)$$

Let  $x = 1/k$ , we have

$$\lim_{k \rightarrow \infty} \|\vec{D}\|_{\frac{1}{k}}^{normal} = \lim_{x \rightarrow 0} \left( \frac{\sum_{i=1}^n |d_i|^x}{n} \right)^{1/x}. \quad (3.10)$$

Take logarithm on both side with base of  $e$ , then

$$\ln \lim_{k \rightarrow \infty} \|\vec{D}\|_{\frac{1}{k}}^{normal} = \frac{\ln \lim_{x \rightarrow 0} \left( \frac{\sum_{i=1}^n |d_i|^x}{n} \right)}{x}, \quad (3.11)$$

which is has an indefinite form of  $\frac{0}{0}$ , thus by taking derivatives of the denominator and numerator of right side of Equation (3.11), we obtain

$$\ln \lim_{k \rightarrow \infty} \|\vec{D}\|_{\frac{1}{k}}^{normal} = \frac{1}{n} \sum_{i=1}^n \ln |d_i|, \quad (3.12)$$

which is

$$\lim_{k \rightarrow \infty} \|\vec{D}\|_{\frac{1}{k}}^{normal} = \sqrt[n]{\prod_{i=1}^n |d_i|}. \quad (3.13)$$

The infinity present in Equation (3.8) has been removed. We create a new vector  $\vec{D}_e$  from the components of vector  $\vec{D}$  as follows,

$$\vec{D}_e = [|d_1|^{-|d_1|}, |d_2|^{-|d_2|}, \dots, |d_n|^{-|d_n|}]. \quad (3.14)$$

then:

$$\lim_{k \rightarrow \infty} \log_2 \|\vec{D}_\epsilon\|_{\frac{1}{k}}^{normal} = \frac{1}{n} \log_2 \prod_{i=1}^n |d_i|^{-|d_i|} = \frac{-\sum_{i=1}^n |d_i| \log_2 |d_i|}{n} \quad (3.15)$$

The quantity on the right hand side of Equation (3.15) equals to

$$(\|D\|_1 H - \|D\|_1 \log_2 \|D\|_1) / n$$

by examining Equations (3.6), (3.7) and (3.15), where  $\|D\|_1$  is the 1-norm of  $D$ . The relation between the asymptotic behavior of the  $\frac{1}{k}$  normalized norm and the entropy (as seen above) shows that they are equivalent. Variates of either of fractional norm with sufficiently large  $k$  or entropy could be regarded as the distance criteria between  $\vec{P}_d$  and  $\vec{P}_1, \vec{P}_2, \dots, \vec{P}_n$ . In the k-means method, we initialize the classes by first finding the centroid (average) of all the vectors in the feature space. The representative describing the first class is assigned to a position in the sample which is farthest from the centroid. The representative of the second class is then assigned to the position in the sample which is farthest from the first class by the measure of entropy or  $\frac{1}{k}$ -norm. The third one is farthest from both the first and second, and so on. To determine which position is farthest from *several* positions, we use entropy or  $\frac{1}{k}$ -norm as the measure. Be careful that we use fractional norm to assign the positions for the representatives of the classes in initialization, but we use *Euclidean norm* to do the k-means classification.

### Cirrus Characterization by K-means Method

Now, let's utilize the k-means method to classify the growths in the cube. The reason for the classification is to have more than one type of cirrus. With more than

one type of cirrus, we may treat cirrus with more than one filter, or we can obtain one filter based on the growths of different types of cirrus, which optimizes the removal of cirrus components. We first map the growth of a pixel (with 16 layers) onto a feature vector in the feature space (16-dimensional), and then set the desired number of classes as five. The desired number of classes was chosen somewhat arbitrarily, but was based, in part, on our previous experience with the images. The number of classes is possibly adjusted later based on the classification of k-means method with  $k=5$ . The adjustment is based on the distances between the representatives of the classes. We first assign a threshold distance  $d_t$ , we then require the minimum distance between the classes to be smaller than  $d_t$ . If all the distances between the classes are larger than  $d_t$ , we increase the number of classes by one, then classify the data again, and the distances between the classes are compared with  $d_t$  again in order to decide whether we need to increase the number of classes again. Such process goes on until the minimum distance between the classes is smaller than  $d_t$ . The initialization problem of the k-means method was solved using 1/4 fractional norm or entropy as mentioned in last section, such that the k-means method converged to possibly the global minimum of energy. The classification was implemented on a MasPar parallel computer at Ames Laboratory, with a FORTRAN 90 code. The FITS (Flexible Image Transport System, an image format, usually used in astronomy, see [Harten *et al.* 1988; Grosbol *et al.* 1988]) image reading and saving subroutines in FORTRAN were from NASA GSFC. With the parallel computer, in the k-means method, we present the sample data (growths) for all 250,000 ( $500 \times 500$ ) pixels at the same time. The distance calculations, class assignments for all the pixels were also done at the same time. Therefore, the classification process was very fast (around

2 minutes, or less, to finish 100–200 iterations), with 250,000 16-dimensional feature vectors. The parallel computer also enabled the morphological operations to be done extremely fast. For example, the ASB filtering process was initially conducted on a Stellar computer, which took more than 24 hours to filter one image. On the parallel computer, the ASB filtering process took less than 2 minutes. It is the speed of the parallel computer that allows us to design self-consistent filters based on classification for all the ISSA fields.

The classification process produces two very important files. One file has the information for the mean growths of the classes. Another file has an  $500 \times 500$  image which contains the class index for each pixel. We call this image the class map for this field.

Before classification, the data (growth) could have been scaled, normalized, transformed. In this dissertation, we only discuss one method of modification – partial normalization.

### **Classification with the growth not modified**

To simplify the problem, we first choose not to modify the growth when conducting the classification. Figure 3.3 shows the areas corresponding to different classes after classifying the growths from Figure 2.1 using the k-means method.

A good way to study the classification result is to show the mean growths of the classes. Comparing the class map with the original image is also helpful. Figure 3.4 shows the profiles for growths of different classes. Note that in Figure 3.4, the standard deviation of each coefficient is shown as an error bar. To avoid confusion caused by the overlapping of the error bars, I have shifted the growth layer for each

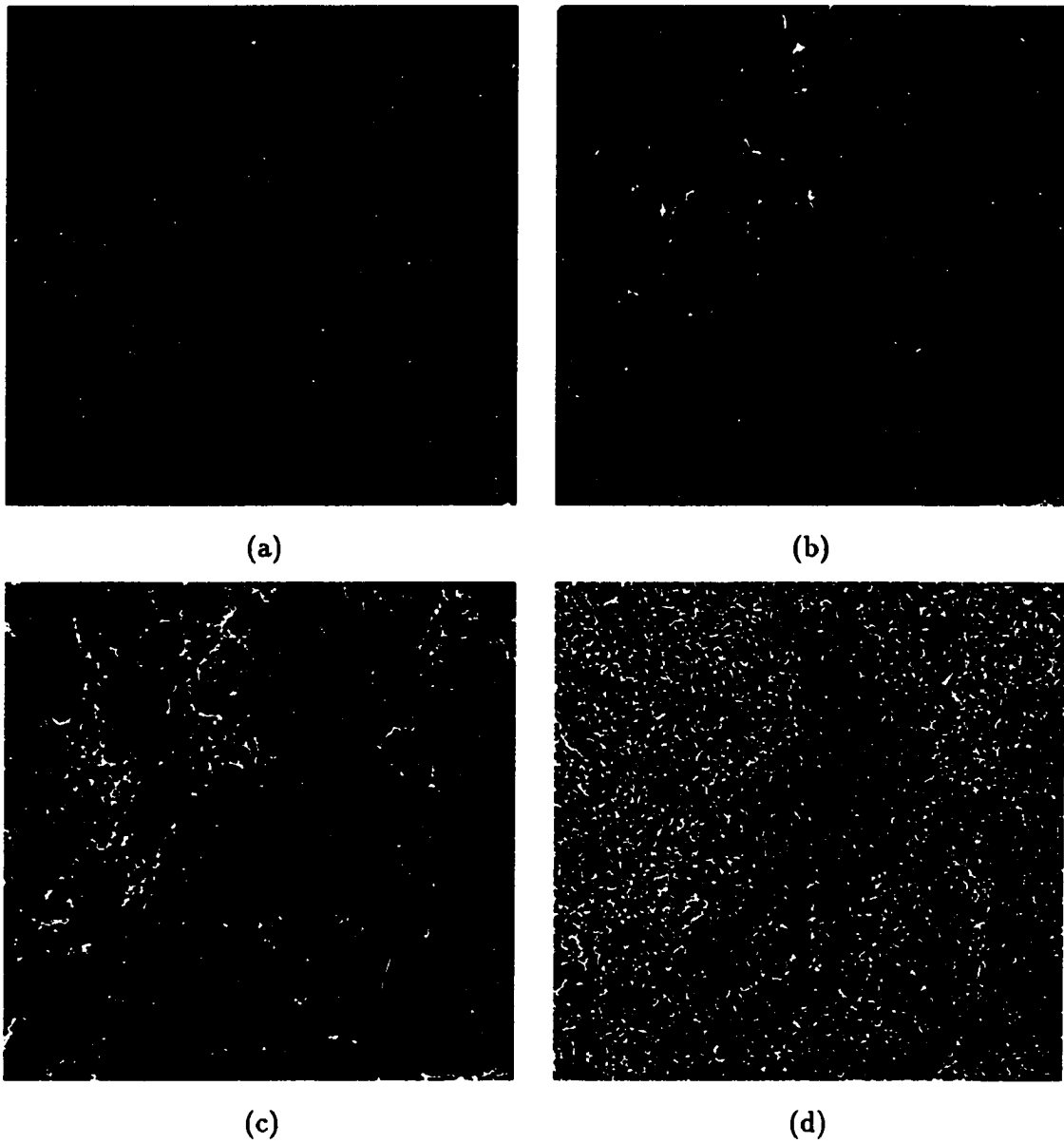


Figure 3.3: The areas for different classes using morphology shown in white: (a) Class 1; (b) Class 2; (c) Class 3; and (d) Class 4

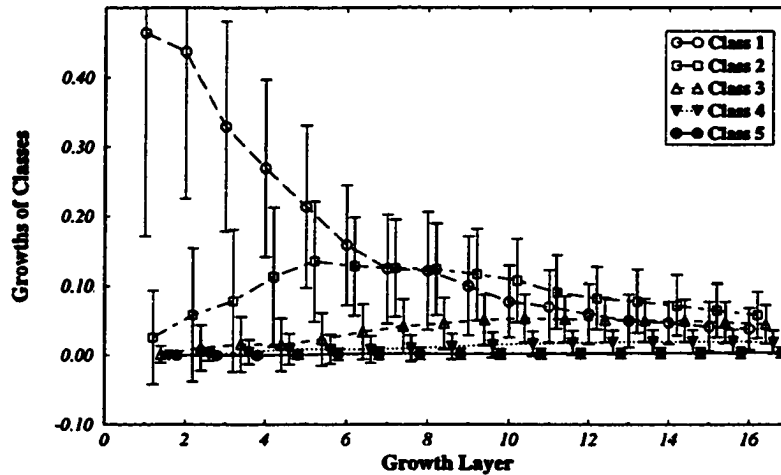


Figure 3.4: The growths for five classes using morphology, the error bars represent standard deviation

class differently. For a class  $i$ , the layer  $j$  is shifted to  $[j + 0.2i - 0.2]$ . When examining the growth profiles, please be careful with such shifting.

By analyzing the class maps, the class growths, and by comparing the class-map with the original image, it is not difficult to see the following results. Class 1 has large growth for small structuring elements and corresponds to sharp point sources (Figure 3.3(a)). Class 2 corresponds to extended sources (Figure 3.3(b)). Class 3 surrounds Class 1 and 2 (Figure 3.3(c)) which is strong cirrus. Class 5 corresponds to very smooth background (very weak cirrus, not shown, but you can find out by excluding the white areas in Figure 3.3). Class 4 is in between Class 3 and 5, i.e., it is medium cirrus (Figure (3.3(d))).

The evaluation of the classification is quite difficult to define. However, the growth profiles shown in Figure 3.4 might be a clue. If there are two classes in such a figure, overlapping with each other within the error bars for most of the growth layer,

then they are more similar to each other. A classification yielding classes resembling each other is not a good classification. For two classes  $i$  and  $j$ , if their probability distributions are  $f_i(x)$  and  $f_j(x)$ , then their resemblance can be evaluated by the resemblance coefficient

$$r_{ij} = \frac{\int dx f_i(x) f_j(x)}{\sqrt{\int dx f_i^2(x)} \sqrt{\int dx f_j^2(x)}}. \quad (3.16)$$

If  $f_i = f_j$ , then  $r_{ij} = 1$ . If  $f_i f_j = 0$  for all  $x$ , then  $r_{ij} = 0$ , which means class  $i$  and  $j$  are exclusive.

For simplicity, we assume  $f_i$  is Gaussian with mean  $\mu_i$  and deviation  $\sigma_i$ . It is not difficult to show that

$$r_{ij} = \sqrt{\frac{2\sigma_i\sigma_j}{\sigma_i^2 + \sigma_j^2}} e^{-\frac{(\mu_i - \mu_j)^2}{2(\sigma_i^2 + \sigma_j^2)}}. \quad (3.17)$$

For more than two classes, the resemblance between the classes are represented by a matrix (resemblance matrix)

$$R = \begin{bmatrix} 1 & r_{12} & r_{13} & \cdots \\ r_{21} & 1 & r_{23} & \cdots \\ r_{31} & r_{32} & 1 & \cdots \\ \vdots & \vdots & \vdots & \ddots \end{bmatrix}. \quad (3.18)$$

Using this matrix, we can further evaluate the resemblance between different classes using less parameters, such as the eigenvalues. When  $r_{ij} = \delta_{ij}$ , the eigenvalues of  $R$  are all 1. Therefore, we can use the eigenvalues of  $R$  (denoted as  $\lambda_i$ ) to evaluate the resemblance of the classes. If  $\lambda_i$ 's are all close to 1, then all the classes are quite different from each other. We also can use  $\Lambda = \sum_i |\lambda_i - 1|$  to evaluate the overall resemblance of the classes. If  $\Lambda$  is close to zero, then the classification produces less similar classes, yielding better classification results.

The resemblance coefficient in our classification is calculated by multiplying together the resemblance coefficients  $r_{ij}$  in each separated dimension of the feature space. The resemblance matrix  $R$  is

$$R = \begin{bmatrix} 1.0000 & 0.0901 & 0.0000 & 0.0000 & 0.0000 \\ 0.0901 & 1.0000 & 0.0267 & 0.0000 & 0.0000 \\ 0.0000 & 0.0267 & 1.0000 & 0.0420 & 0.0000 \\ 0.0000 & 0.0000 & 0.0420 & 1.0000 & 0.0000 \\ 0.0000 & 0.0000 & 0.0000 & 0.0000 & 1.0000 \end{bmatrix}. \quad (3.19)$$

Eigenvalues of  $R$  are calculated using MATLAB, which produces

$$\begin{aligned} \lambda &= [\lambda_1 \lambda_2 \lambda_3 \lambda_4 \lambda_5] \\ &= [0.9052 \ 0.9601 \ 1.0000 \ 1.0398 \ 1.0949]. \end{aligned} \quad (3.20)$$

The overall resemblance  $\Lambda$  is 0.2694.

Another important parameter for the classification is the overall deviation for each class. To simplify the analysis, we assume the growth on different layers to be uncorrelated. Using the MSE (Mean Square Error) criterion, we define the overall deviation of class  $i$  as

$$\sigma_i = \sqrt{\sum_{j=1}^{16} \sigma_{ij}^2}, \quad (3.21)$$

where  $j$  is the index of growth layer. Table 3.1 shows the overall deviation for different classes. Note that the classes are rearranged in such a way that the overall deviation decreases when the class index increases.

Table 3.1: The overall deviation for different classes

Class	1	2	3	4	5
$\sigma$	0.469199	0.274343	0.135881	0.068942	0.027275

### Classification with growth partially normalized along the growth layer

As we can remember, in the ASB filter design, the selected sample cirrus pixels produce normalized growth, which were further used to get a mean cirrus growth. The so-called normalization is with respect to the growth layer direction, i.e., normalization for a pixel is done by dividing the the growth by total sum of the growths of this pixel (total area). The partial normalization in this chapter includes the case of normalization, and the case of non-normalization. We use a parameter  $\beta$  to define the partial normalization. A vector  $\vec{x} = (x_1, x_2, \dots, x_n)$ , is partially normalized with parameter  $\beta$ , into

$$\vec{y} = \vec{x} / \left( \sum_{i=1}^n |x_i| \right)^\beta. \quad (3.22)$$

When  $\beta$  equals zero, the vector is not changed. When  $\beta$  equals to 1, the vector is totally normalized, with its sum of the absolute values of the components equal to 1. The reason for introducing this method to modify the growth for classification is that when dealing with the images close to the Galactic plane, we encounter problems of areas with very strong fluxes and thus relatively weak cirrus. To emphasis the importance of the cirrus pixels, we may introduce a large  $\beta$  which yields reasonable classification results, i.e., the classes with strong intensities have population more than certain values. By using appropriate  $\beta$ , we may classify the samples such that the population of the classes obey approximately certain distribution. With increasing  $\beta$  the classes containing the strongest point sources have more population. For example,

Table 3.2: The population of Class 1 when partially normalized using different parameters

$\beta$	0.00	0.25	0.50	0.75	1.00
$N_1$	178	357	18371	44639	65061

Table 3.3: The eigenvalues of the resemblance matrix and overall resemblance using different partial normalization factors

$\beta$	0.00	0.25	0.50	0.75	1.00
$\lambda_1$	0.9052	0.9929	0.9992	0.9993	0.9240
$\lambda_2$	0.9601	1.0000	1.0000	1.0000	1.0000
$\lambda_3$	1.0000	1.0000	1.0000	1.0000	1.0000
$\lambda_4$	1.0398	1.0000	1.0000	1.0000	1.0000
$\lambda_5$	1.0949	1.0072	1.0008	1.0007	1.0760
$\Lambda$	0.2694	0.0144	0.0017	0.0015	0.1521

the field I029 at 100  $\mu\text{m}$  was studied using different values of  $\beta$ . When  $\beta$  is zero, only 178 pixels belong to Class 1 (the strongest point sources). When  $\beta$  increases, its population increases. Table 3.2 shows the relationship of the population of Class 1 ( $N_1$ ) and  $\beta$ .

Note that around  $\beta = 0.5$ , the population changes dramatically. To relate this dramatical change of  $N_1$  with the resemblance of the classes, we calculated the eigenvalues  $\lambda_i$  and the overall resemblance  $\Lambda$  at different  $\beta$ , which are shown in Table 3.3. It is reasonable to assume that the dramatic change in  $N_1$  is related to small  $\Lambda$ , because at  $\beta = 0.5$  and 0.75, the overall resemblance almost have the same value, which corresponds to the minimum resemblance at all  $\beta$ .

### Approximate Linearity of Sieving Process

The filtering process in ASB filter design is the equal CI area method (see Chapter 2), which actually took too much intensity from the growth. For instance, the fluxes of strong point sources are reduced by a factor of up to more than 1/3, the fluxes of faint sources are reduced by a factor of 3. The reasons for the flux reduction follows. First of all, the equal CI area method assumes the growths in the CI are all from the cirrus, which might not be true if CI is not chosen properly, or if there are no CIs which have zero growths for point sources. Secondly, the filtering process assumes that the growths from both cirrus and point sources are linearly superposed, which is not necessarily true (under certain conditions, however, this can be approximately assumed). Thirdly, the equal CI area method assumes that all the pixels in the image have the same cirrus growth behavior (or shape). This is not true, as we have seen from last section with the classification results. Therefore, although the equal CI area method produces image free of severe cirrus emission, the fluxes of the point sources are in doubt.

The basis of the equal CI area method is related to the approximate linearity of the sieving process under certain conditions. Such an approximation is discussed in Chapter 8, where we analyze different size information extractors (some are not introduced at this point). As we shall see in Chapter 8, a sieving process with cylindrical SEs extracts growth information from a fixed-slope peak, linearly dependent on the slope  $k$  (for instance a function  $f(x) = -k|x|$  has a slope of  $k$ ). Roughly speaking, if we assume the cirrus to be strong at locations of the emission of point sources where they are strong, we may think that the cirrus modifies the point source by changing its slope. In such a case, the sieving process by cylindrical SEs is linearly dependent

on the signal. For peak  $p(x)$  and cirrus  $c(x)$ , with the sieving process of cylindrical SEs at step  $i$ , denoted as  $\mathcal{S}_c^i$ , we have

$$\mathcal{S}_c^i(p(x) + c(x)) = \mathcal{S}_c^i(p(x)) + \mathcal{S}_c^i(c(x)). \quad (3.23)$$

In Chapter 8, we also discuss the sieving process by Gaussian SEs. It is shown there, that the sieving process of Gaussian SEs at step  $i$ , denoted as  $\mathcal{S}_g^i$ , is approximately linear on  $p(x)$  and  $c(x)$  when  $i$  is large enough, i.e., when  $i \geq I$ , where  $I$  is a threshold. The threshold  $I$  depends on the heights of the Gaussian SEs, and the slope of the peak. If the heights of the SEs are large, then  $I$  is large. If the slope of the peak is large, then,  $I$  is small. The value  $I$  is very difficult to be estimated mathematically, however, it can be obtained using numerical simulations. For instance, in Chapter 8, when the heights of SEs are 10, and the slope of the peak is 0.7143, the value of  $I$  is between 4 and 5. Therefore, if the peaks in our problems have slopes larger than 0.7143, the value of  $I$  is smaller than 5. Examination of the field I029 (Figure 2.1) tells us that the point sources have slopes larger than 0.7143. Therefore, we may assume that the sieving process at growth layers larger than or equal to 5 is a linear operator. Also, in Figure 3.4, we see that the cirrus (Classes 3, 4, and 5) have very small growth at layers 1 to 4. Therefore, if we assume the signal in the image is a combination of the point sources (or extended sources) and cirrus, we can assume that the sieving process is approximately a linear operator at layers from 1 to 4 too. In the whole, the sieving process with Gaussian SEs of height 10 can be assumed to be a linear operator for field I029.

The filtering formula in Equation (2.2) is based on the approximate linearity of the sieving process. The definition of the weight image  $W_j$  for layer  $j$  is ambiguous, though. One example of the definition is the equal CI area method in the ASB filter

design. More definition of the weighting (filtering methods) will be discussed later. As we have seen from Figure 3.4, only one cirrus class (Class 3) has strong growth, the other two cirrus (Class 4 and 5) have much smaller growths. Therefore, the filtering process using one type of cirrus behavior is valuable. Again, we need to emphasize that considering multiple types of cirrus will yield better filtering results. The next sections discuss the general cirrus removal processes using one type of cirrus and multiple types of cirrus. For all these methods, we use three images to judge how well the filtering is done. The first one is ISSA I029 fields at  $100 \mu m$ , the second one is I029 superposed with a point source (FWHM is 2.80 pixels, i.e., 4.2 arc minutes with flux  $I_p = 62.7 \text{ MJy sr}^{-1}$ ) at 16 locations 100 pixels apart (shown in Figure 3.5(a)). The third one is I029 superposed with an extended emission (galaxy M101 scaled with a factor of 0.2, FWHM is around 4.99 pixel, i.e., 7.49 arc minutes with flux  $I_e = 165.5 \text{ MJy sr}^{-1}$ ), also at 16 locations 100 pixels apart (shown in Figure 3.5(b)). These sources superposed were extracted from I029 and the field containing M101. Sources extracted were removed of background by thresholding, and scaled by a factor to reduce the flux. The reason for the scaling is that we do not wish to use very strong sources as the tests. The fluxes were determined by a software package IRAF, which uses the sky information given by the user to remove sky flux, thus determines the fluxes for the sources by summations of the intensities at pixels of the sources. The field I029 is used to judge the appearance of the filtered result by our eyes. Figure 3.5(a) is used to judge how well the fluxes of the point sources are retained after the filtering. Figure 3.5(b) is used to judge how well the fluxes of extended emissions are retained after the filtering.

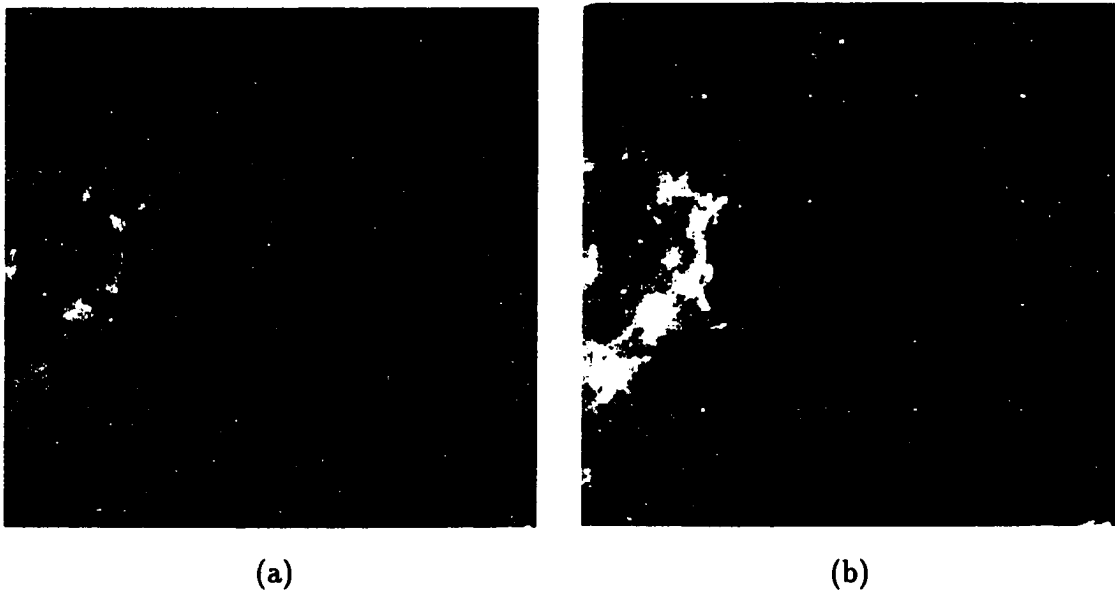


Figure 3.5: The image of ISSA field I029 at  $\lambda = 100 \mu m$  superposed at 16 locations (white dots in a square grid format) with: (a) point source (FWHM = 4.20 arc minutes); and (b) extended source (FWHM = 7.49 arc minutes)

### Method of One-Type-of-Cirrus

As we have discussed in last section, using one type of cirrus structure would be a good method to remove the cirrus components for the purpose of object identification. The cirrus component at a pixel could be estimated based on the mean cirrus behavior in many ways. Such cirrus estimations could be approximately correct for cirrus pixels, but might not be correct for pixels of point sources, though. Most of the time, over-estimation of cirrus happens to point sources and extended emission, producing loss of fluxes for them. The remedy for such over-estimation can be conducted by down-scaling the estimation [He *et al.* 1995].

#### Equal CI area method revisited

This method has been discussed in detail in Chapter 2, along with the ASB filter design. Based on the growths of the most significant cirrus from the classification results, we obtain the filter coefficients  $F_i$ ,  $i \in L$  by normalization along the direction of the layers, where again  $L$  is the set of the growth layers' indexes. The normalization is discussed in Chapter 2. It is done by dividing the filter coefficients by the total sum of their absolute values. For each pixel we rescale the cirrus characteristic growth such that the area (sum of the growths in consideration) of the growth for pixel  $[i, j]$  and for cirrus characteristic growth in the CI is equal. Figure 2.5 is an illustration of this method. Equation (2.4) is the mathematical representation of the scaling factor for the cirrus in this method.

For field I029, the coefficients  $F_i$  are obtained by normalizing the growths of Class 3, since it is the most significant cirrus. The CI was determined based on the classification results (Figure 3.4). Note in Figure 3.4, Class 1 and 2 have smallest

growths at the highest layers. As we analyzed in previous sections, Class 3 surrounds Class 1 (point sources) and Class 2 (extended emission). Class 3 has similar growths at higher layers to Class 1. It has a little bit smaller growths at higher layers than Class 2, but Class 1, 2, and 3 are close within the error bars at high layers. It is quite safe to assume that the growths at higher layers are mainly from cirrus. We choose CI as [10, ..., 16], which is at the high layers, yet the normalized areas for Class 3 and 4 are very close there (i.e., Class 3 and 4 are alike at the CI). Using this CI, we filter field I029 (Figure 2.1), Figure 3.5(a) and Figure 3.5(b). Figure 3.6(a), (b), and (c) show the corresponding filtered results, using equal CI area method, of Figure 2.1, Figure 3.5(a), and Figure 3.5(b), respectively. Comparing them with the original images, one sees that the cirrus clouds in the original images are removed. We found that the cirrus intensity is reduced by a factor of 30. Figure 3.6(a) is better than the result from ASB filter, where the cirrus is reduced by a factor of 15. Also the new filtered image has smoother background than the result from ASB filter. The point sources and extended emissions less visible in the original images are now more easily seen. The filtered image of Figure 3.5(a) is Figure 3.6(b), in which the 16 point sources arranged periodically are shown. Although these point sources were superposed onto I029 at different locations which have quite different cirrus background (for instance, some locations are in bright areas, and some are in dark areas), the filtered image shows point sources with very similar appearances. The FWHM and fluxes of these point sources are further measured using the package IRAF. The FWHM is determined by fitting a point source by a Gaussian peak. The flux of the point source is determined by subtracting from the total flux (the sum of the the intensities at each pixels) of the point source by the sky flux (averaged flux of

the background) using the information given by the user. The average of the FWHM of the 16 point sources is 2.81 pixels (4.22'). The standard deviation of the FWHM is 0.097 pixels (0.146'). Thus the distortion between the 16 filtered point sources judged by the FWHM is around 3.5%. The average of the measured FWHM is larger than the real FWHM by 0.36%. The deviation (square root of MSE (mean square error)) of the measured FWHM from the real value is around 0.1 pixels, which means the reliability of the measured FWHM is within 3.5% of error. The measured fluxes for the 16 point sources are  $56.1 \pm 2.0$  MJy sr<sup>-1</sup>. The error between the average and the real flux is 11%. Thus the deviation of the measured fluxes from the real flux is 7.0 MJy sr<sup>-1</sup>, i.e., the reliability of the measured flux is within 11.1% of error.

Figure 3.6(c) shows the filtered image of Figure 3.5(b), it contains 16 extended sources arranged periodically, in the field of I029. The 16 extended sources in the filtered image are very similar in appearance. The FWHM and the fluxes of the extended sources are measured by IRAF in the same way as I described in last paragraph. The average of the FWHM is 4.30 pixels, the standard deviation of the FWHM is 0.077 pixels. Thus the average of the FWHM is 0.69 pixels from the real value, and the deviation of the measurements from the real value is 0.694 pixels (13.9% smaller than the real value). The flux for them are also found by IRAF using polynomial fitting of the background. The fluxes of the 16 extended sources are  $100.6 \pm 4.1$  MJy sr<sup>-1</sup>, i.e., the average is 39.2% lower than the real flux. The deviation of the measurements from the real flux is 65.03 MJy sr<sup>-1</sup> (39.3%). Such big losses in fluxes and in FWHM are due partly to the over-estimation of the cirrus components in the filtering process, but mainly to the SE sizes which are not sufficiently large (as will be discussed soon).

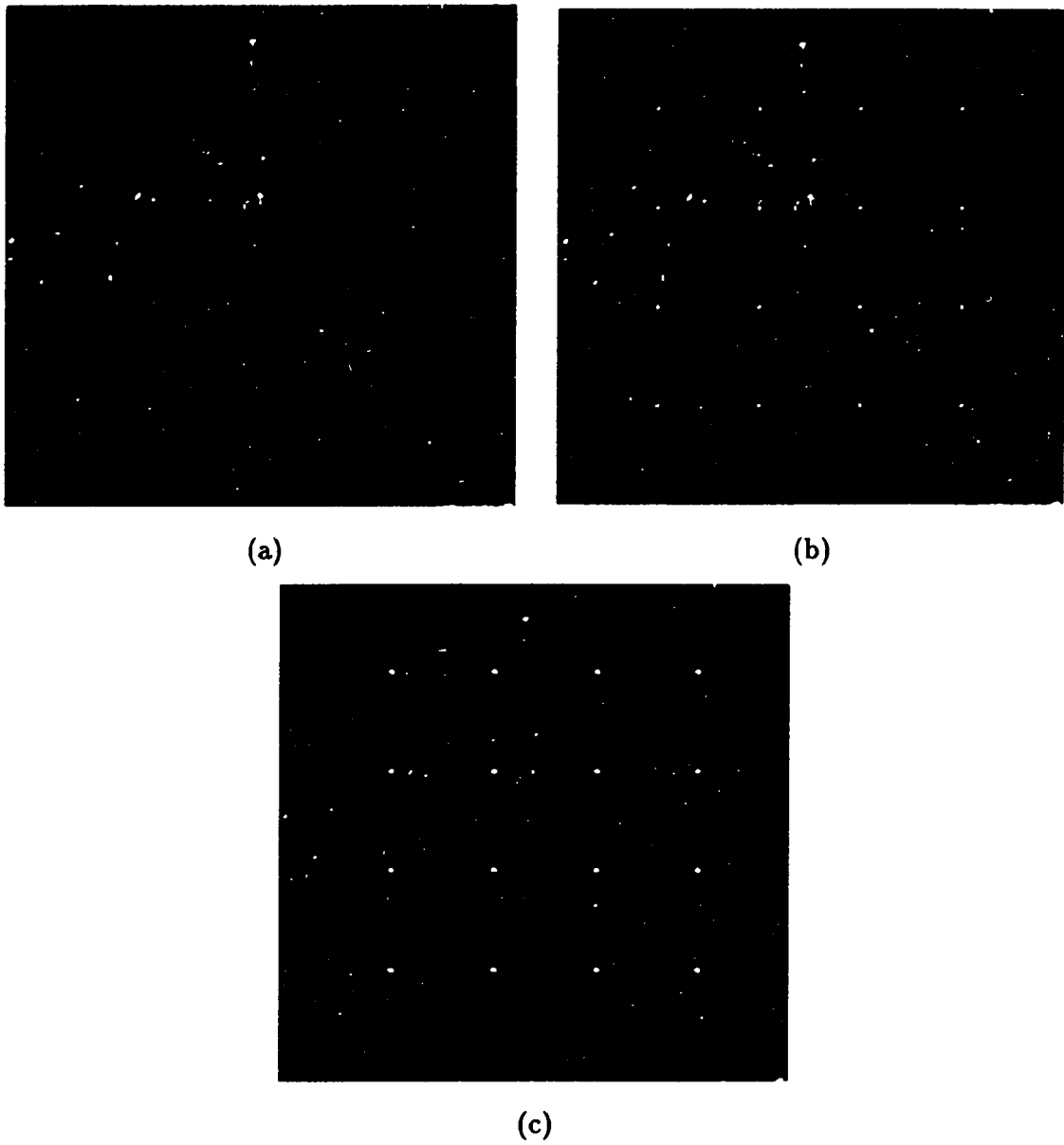


Figure 3.6: The filtered results using equal CI area method of: (a) Figure 2.1; (b) Figure 3.5(a) ; and (c) Figure 3.5(b)

Table 3.4: The CI area ratio with morphology method

Class	1	2	3	4	5
CI ratio	0.149	0.381	0.595	0.649	0.656

The loss of fluxes for the point sources and extended sources discussed above is due to over-estimation of the cirrus components for these sources as we have discussed in last section. Such over-estimation can be compensated by giving the cirrus components another weight (or scaling factor) on the bases of each pixel. This weight needs to be small when a pixel is more like a point source or extended sources (Class 1 or Class 2), close to 1 if this pixel is more like cirrus (Class 3, 4, and 5). This weight could be a function of some parameters which distinguishes between point sources and cirrus. One of these parameters for each growth profile is the ratio of the sum of growths in the CI to the sum of the growths at all the layers. We call this ratio the *CI area ratio*, or for short, the CI ratio. For our problem of field I029, with CI = [10,...,16] the CI ratio for the five classes are shown in Table 3.4. The CI ratio for the point sources is the smallest, and the CI ratio for the cirrus (Class 3, 4, and 5) are close to each other in values. The CI ratio of Class 2 (extended sources) is between that of the point sources, and those of the cirrus classes.

There are many ways to define the weighting function. The simplest way is a step function which gives no transient weighting. Thus we can not regard the sources and the cirrus as more than two categories when weighting. Another simple example of such a weighting function is a sigmoidal function which enable the transient weighting between the strongest point sources and the weakest cirrus. If we denote the CI ratio

for pixel  $[i,j]$  as  $r_{i,j}$ , and denote the weighting for this pixel as  $w_{i,j}$ , then

$$w_{i,j} = \frac{1}{1 + e^{-(r_{i,j}-\alpha)/\delta}}, \quad (3.24)$$

where  $\alpha$  and  $\delta$  are two parameters to be adjusted. Also note that  $\delta > 0$  in order for a small CI ratio to have small weight. When the  $w_{i,j}$  are obtained, the scaling function of the cirrus components is then  $w_{i,j}k_{i,j}$ , where  $k_{i,j}$  is found by the equal CI area method as discussed in Chapter 2. The cirrus removal process is as usual, to first subtract the cirrus components from growth of each pixel, and then sum up the modified growths for this pixel to obtain the filtered result.

We filtered Figure 3.5(a) and Figure 3.5(b) again incorporating the sigmoidal weighting function, with  $\alpha = 0.2757$  and  $\delta = 0.1626$ . The filtered images have similar appearances to Figure 3.6(b) and Figure 3.6(c). The reason is that such weighing does not change the amount of cirrus taken from cirrus pixels, it does increase the fluxes of the point and extended sources which give a little bit larger sources when displayed. Thus there is no need to display them here. The FWHM of the 16 point sources are  $2.85 \pm 0.05$  pixels, which gives a deviation from the real value of 0.07 pixels (2.5%). It is obvious that the average FWHM has a larger deviation from the real FWHM than the case when the weighting is not considered, but the standard deviation of the measurements is smaller, which gives a smaller deviation from the real FWHM in total (thus high reliability). The FWHM of the measured extended sources in Figure 3.6(c) give a statistics of  $4.55 \pm 0.08$  pixels, and a deviation from the real FWHM of 0.448 pixels (9.0%). The fluxes of the 16 point sources and 16 extended sources are analyzed similarly to the procedure discussed before. The fluxes of the 16 point sources are  $61.35 \pm 2.4$  MJy sr<sup>-1</sup>, which is 2% from the real flux. The fluxes of the extended sources are  $131.6 \pm 5.6$  MJy sr<sup>-1</sup>, which is still 21% lower than

the real flux. The reason that the extended sources are still 21% lower than the real flux, and the FWHM is still 9% smaller than the real FWHM, is that the SEs employed are not large enough for the total SI extraction from extended sources. To retain correct intensity of the extended sources, one needs to use SEs with larger sizes, or to use another set of SEs (such as cylindrical SEs, as will be mentioned in next chapter). We thus conclude that the Gaussian SEs can preserve the fluxes and the FWHM for point sources (FWHM is less than 4.2 arc minutes) in within 2–3%. But for extended sources (FWHM larger than 7.5 arc minutes), the flux is lost by more than 20%, and the distortion of the filtered source (or its FWHM) from the original source can be up to 9%.

A list of the fluxes and FWHMs for these point and slightly extended sources can be found in Appendix B, Table B.1.

### **Non-overlapping method**

The scaling factors  $k_{i,j}$  in the one-type-of-cirrus removal process can also be found in ways other than the equal CI method. For instance, summation operators in Equation (2.4) can be replaced by median operators which yields a new  $k_{i,j}$ . The non-overlapping method introduced by He *et al.* [1995] is of interest because it has the ability to filter an image well and avoids negative intensities. This section discusses the overlapping method in detail.

Suppose we rescale the characteristic cirrus growth, which we defined in previous sections from the result of classification, such that in the *CI* the cirrus growths are below the growths of pixel  $[i, j]$ . We can guarantee that the subtraction of the cirrus from the growth of a pixel will not make the output a negative value in *CI*. The

reason behind this method is that the sieving process produces positive growths when the SEs are chosen properly (such as cylindrical and hemispheric SEs). As will be seen in Chapter 4, the size information extracted by the sieving process of the Gaussian SEs are almost all positive.

The non-overlapping method is defined by a scaling factor for the cirrus components at pixel  $[i,j]$  of

$$k_{i,j} \leq \min_{l \in CI} \frac{G_{l+1,l}^{(i,j)}}{F_l}, \quad (3.25)$$

where again,  $G_{l+1,l}^{i,j}$  is the growth of pixel  $[i,j]$  at layer  $l$ ,  $F_l$  is the growth of the filter at layer  $l$ . The  $k_{i,j}$  we often use is the maximum values found by above equation, that is

$$k_{i,j} = \min_{l \in CI} \frac{G_{l+1,l}^{(i,j)}}{F_l}, \quad (3.26)$$

Figure 3.7 is an illustration of how the cirrus components are accounted for using this method. The thick line is the growth for the pixel  $[i,j]$ , the thin line is the filter coefficients scaled by  $k_{i,j}$ . Notice that the thin line lies under the thick line in  $CI$ .

We again select the CI as  $[13, \dots, 16]$  for the reason that the growths for Class 1 and 2 have small values there. Figure 2.1, 3.5(a), and 3.5(b) are filtered using the non-overlapping method. We only show the filtered image of Figure 2.1 in Figure 3.8 for the reason that the filtered images have similar filtering qualities, and the objectives that we filter Figure 3.5(a) and 3.5(b) are to examine the loss of the fluxes. The filtered image makes the point sources which were less visible in the original image easier to be recognized. A comparison of Figure 3.8 with Figure 3.6(a) (filtered image by the equal CI area method) tells us that the non-overlapping method retains very small structures and produces a less smooth image. Part of the fine structure is

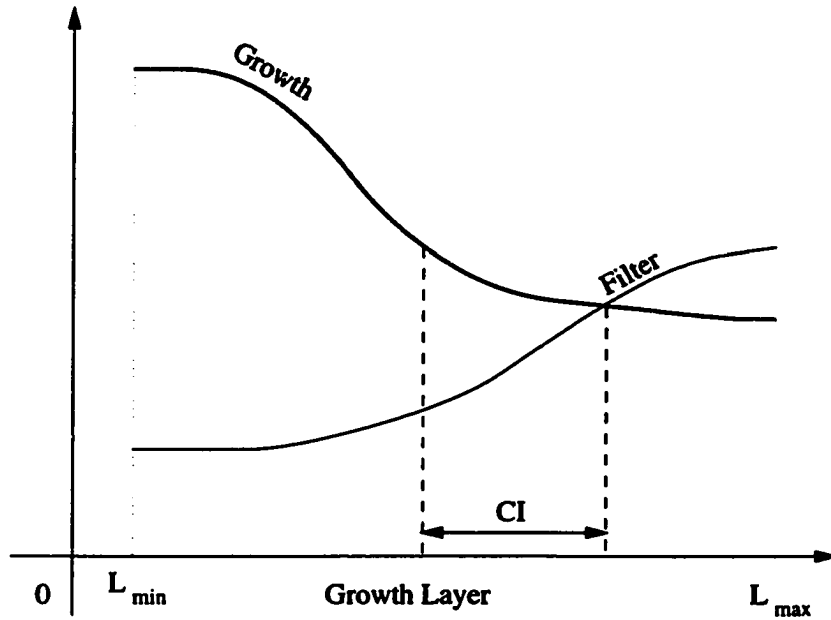


Figure 3.7: The non-overlapping method

from point sources, but part of the fine structure could be random noise produced for example by the detectors in the spacecraft. Therefore if there are sources of noise with very fine-scale structure (such as 1 or 2 pixels wide), the non-overlapping method is unable to remove them. The cirrus intensity is reduced by a factor of 15 when compared with the original image.

The filtered results of Figure 3.5(a) and 3.5(b) are analyzed in a similar fashion to the analysis in the equal CI area method. The FWHM of the point sources are  $2.87 \pm 0.06$  pixels, which gives a deviation to the real value of 0.09 pixels (3.2% larger). The fluxes of the 16 point sources are  $61.4 \pm 2.7$  MJy sr<sup>-1</sup>, which is only 2% lower than the real flux. We see that the FWHM by the non-overlapping method has larger error than the equal CI area method, and the flux by this method is much better preserved. The FWHM of the extended sources are  $4.71 \pm 0.08$  pixels, which gives a deviation to

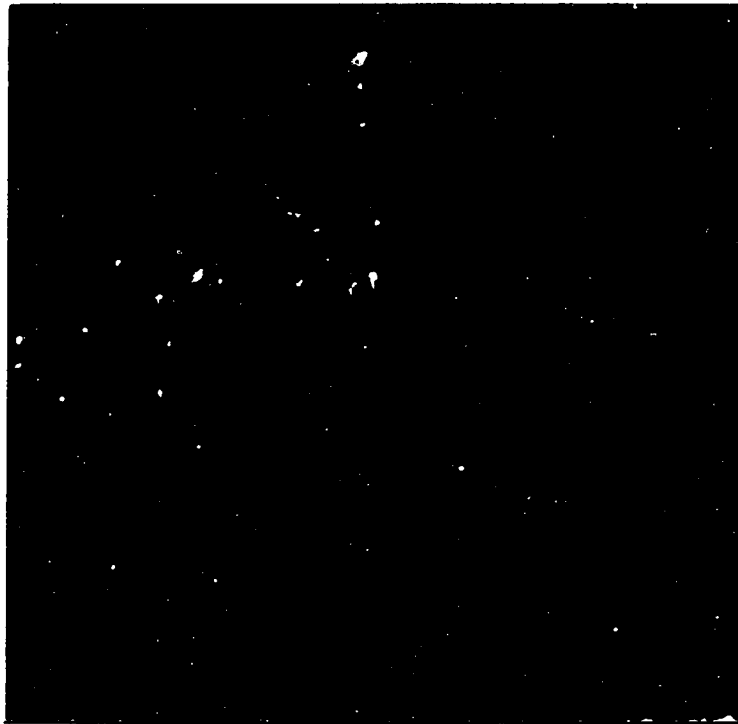


Figure 3.8: The filtered image of Figure 2.1 using the non-overlapping method

the real FWHM of 0.29 pixels (5.8% smaller). The 16 extended sources are  $139.5 \pm 5.9$  MJy sr<sup>-1</sup>, which is 15% lower than the real flux. Comparing this result with the result from the equal CI area method, one sees that the non-overlapping method preserve fluxes (note that the extended sources lost fluxes due to too small SEs) better than the equal area method. This method gives a little bit larger 3.2% compared with 2.5% error on FWHM for the point sources, but it gives smaller distortion when the sources in consideration is a extended source. We put a sigmoidal weighting with  $\alpha = 0.175628$  and  $\delta = 0.107200$  onto the filtering process to see how it affect the fluxes, but found that the fluxes for the point and extended sources are not change compared with the corresponding fluxes without the weighting.

A list of the fluxes and FWHMs for these point and slightly extended sources can be found in Appendix B, Table B.2.

### Multi-Cirrus Filtering

As we have discussed several times, when we consider the cirrus by having one type of growth behavior, we are limiting our filtering process to narrow areas of the growth curve. The trade-offs between different classes result in over-estimation or under-estimation of the real cirrus components for a pixel. By considering more than one type of cirrus when filtering, we may obtain better flux preservation, as well as removing the cirrus more perfectly.

Multiple filters were obtained from the cirrus growths (of Classes 3, 4, and 5). Since Class 3 is closer in the growth intensity and the locations to Classes 1 and 2, we used the growth of Class 3 to remove the cirrus components from a pixel which belongs to Class 1, 2, or 3. The cirrus components for a pixel belonging to Class

4 was removed by using the growth of Class 4. The cirrus components for a pixel belonging to Class 5 was removed by the growth of Class 5.

For Classes 1 and 2, the cirrus scaling factor  $k_{i,j}$  could be estimated by the equal CI area method or the non-overlapping method. In such cases, the fluxes for the point sources and extended sources would be the same as the results in last section. Flux retention could be done in the same fashion discussed in last section.

One more reasonable way to estimate the cirrus components of the point sources and extended sources is described as follows. For each point source, or extended source, the nearby cirrus (could be Class 3, 4, or 5) is studied. The point and extended pixels were assumed to be pixels of Classes 1 and 2. The surrounding cirrus pixels for each source is obtained by simply using a circular mask of size 10-15 to select pixels of Classes 3, 4, and 5. By using the growth of the cirrus surrounding this point source, we remove the cirrus components from the growth of the source by simple subtraction (without rescaling) of the growth of cirrus which is obtained from the surrounding cirrus pixels by average. Such a process is more time-consuming, but it surely gives better flux retention. Figure 3.9 shows the filtered image of Figure 2.1 using this method. The appearance of the image is similar to the results before. It is found that the background of the filtered image is smoother than the one by the equal CI area method and the non-overlapping method. The filtering quality, because of the residual in consideration, is higher than equal CI area method, but smaller than the non-overlapping method. The cirrus intensity is reduced by a factor of 35 compared with the original image. Figure 3.5(a) and (b) are also processed using this method. The 16 point sources have fluxes of  $56.3 \pm 2.0$  MJy sr<sup>-1</sup>, i.e., 10% of the fluxes are lost. They have FWHM of  $2.72 \pm 0.20$  pixels, which gives a overall

deviation to the real FWHM of 0.215 pixels (7.7% lower). Note that this method gives rather big an error for the FWHM, and the averaged FWHM is smaller than the real value, instead of larger than the real value in previous methods. The 16 extended sources have fluxes of  $102.6 \pm 4.0$  MJy sr<sup>-1</sup>, i.e., the flux of the real source is lost by 38%. They have FWHM of  $4.3 \pm 0.08$  pixels, which gives a deviation to the real FWHM of 0.7 pixels (14% lower). Using sigmoidal cirrus weighting, we may compensate part of the losses. The 16 point sources after the weighting have fluxes of  $61.8 \pm 2.3$  MJy sr<sup>-1</sup>, i.e., they are only 1.4% lower than the real flux. The 16 extended sources now have fluxes of  $135.6 \pm 5.4$  MJy sr<sup>-1</sup>, i.e., they are 18% lower than the real flux (which is again due to the small sizes of the SEs). The FWHM of the 16 point sources now is  $2.825 \pm 0.045$  pixels, which gives a deviation to the real value of 0.05 pixels (1.8%). The extended sources have FWHM of  $4.50 \pm 0.07$  pixels, which gives a deviation to the real value of 0.5 pixels (10%). Thus the multiple cirrus filtering, when sigmoidal weighting is considered, has a performance between the equal CI area method and the non-overlapping method in flux preservation and FWHM retention.

A list of the fluxes and FWHMs for these point and slightly extended sources can be found in Appendix B, Table B.3.

### **Automated Adjustment of Partial Normalization Factor**

The previous sections discussed the filtering process using sieving, classification, and cirrus subtraction. The subtracted cirrus components could be weighted in order to preserve the flux for the point sources.

The filtering includes several variables. The sizes and shapes of SEs are two basic variables in the sieving process. The partial normalization factor of the growth

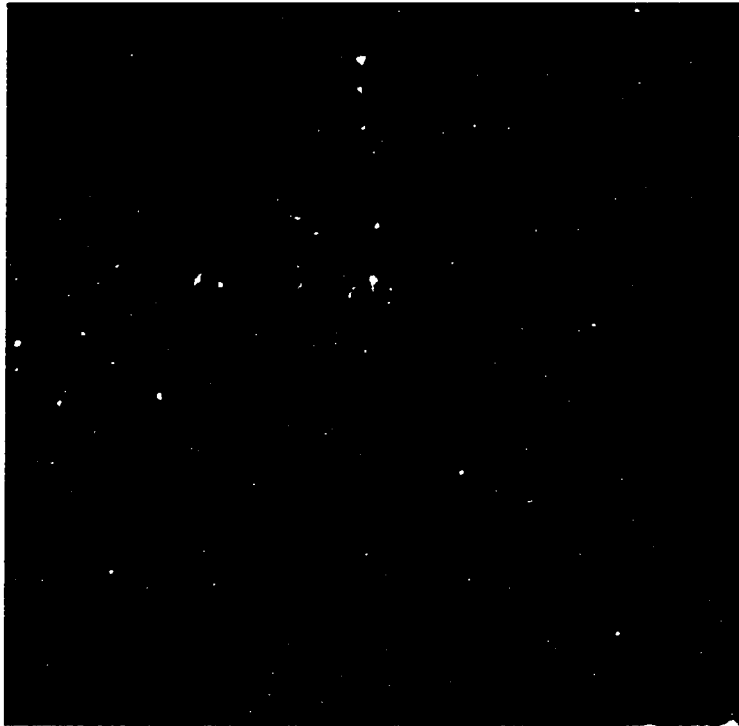


**Figure 3.9:** The filtered image of Figure 2.1 using multi-cirrus filters

in the process of classification is a variable too. The cirrus subtraction technique and the cirrus component scaling factor are variables in the final step.

The cirrus component subtraction techniques (and also the scaling factors) were discussed in previous sections. The sizes and shapes of SEs will be discussed in the next chapter together with granulometry. In this section, we discuss the adjustment of the partial normalization factor  $\beta$  for the ISSA fields.

As we have discussed before, the parameter  $\beta$  changes the population (the number of elements of a specific class) of the point source class. It also changes the population for other classes. For instance, the field I029 was classified using the growths and different partial normalization factors (different  $\beta$ ). Figure 3.10 shows the distribution of the population (percentage of the population among the total pixels) for the classes at different  $\beta$ . Like we did before, the class index is arranged in such a way that it increases when the sum of growths of the class from layer 1 to 8 decreases, thus strongest point sources is in Class 1, and the weakest cirrus is Class 5, always. When  $\beta$  is zero (non-normalized), the population increases exponentially as the class index increases. When  $\beta$  increases to 0.25, the overall curve changes less abruptly. That is to say, the curvature of the curve became smaller. As  $\beta$  gets up to 0.50 and 0.75, the population of the classes can be treated as uniformly distributed. When  $\beta$  gets to 1.00, the distribution of population is decreasing when class index changes from 3 to 5.

The distribution of population of the classes for other fields are also studied. Fields far from the Galactic plane have similar results as Figure 3.10. However, the fields close to the Galactic plane are quite different. The fields I390, I391, I363, and I108, were studied using different partial normalization factors. They all show tiny

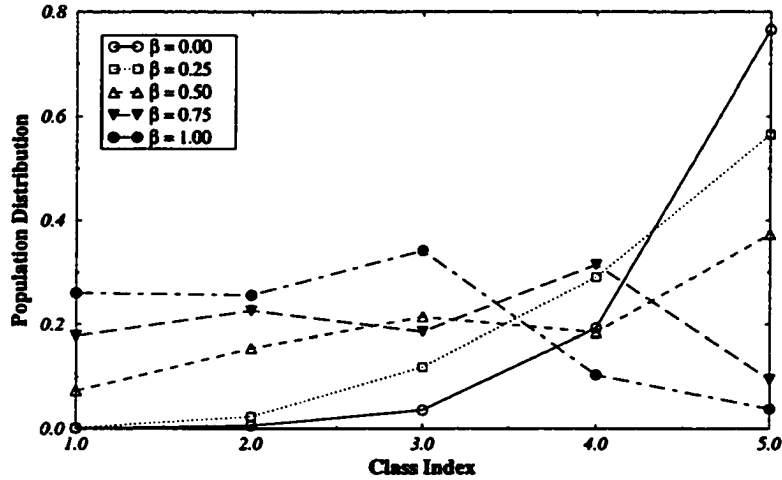


Figure 3.10: The distribution of population of different classes for field I029 with  $\beta = 0, 0.25, 0.5, 0.75,$  and  $1.0$

populations for Class 1, 2, and 3 when  $\beta$  is small (such as 0.00 and 0.25). Figure 3.11 shows the population distribution of the field I390. Note that the distribution of population behaves similarly to Figure 3.10 except that the value of  $\beta$  at which the population approximates the uniform distribution is higher (between 0.75 and 1).

Different  $\beta$  produces different cirrus estimations and gives different filtering results. The qualities of the filtered results were examined, and compared to each other. A good filtering produces a filtered image with few pixels of negative intensities, small deviation of the negative values from zero, smooth background in areas other than the point and extended sources, and smooth residuals with respect to the original image (the residual should be free of traces of point and extended sources). Among the attributes, the smoothness of the residual and the smoothness of the background of the filtered image are in conflict, therefore a trade-off needs to be made between them. We define the gradient of a pixel  $[i,j]$  by  $\vec{g}^{i,j} = (I_{i+1,j} - I_{i,j}, I_{i,j+1} - I_{i,j})$ , where

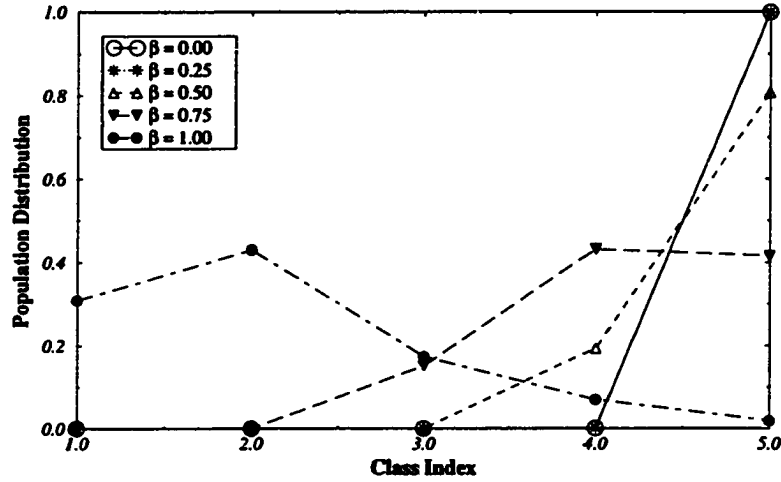


Figure 3.11: The distribution of population of different classes for field I390 with  $\beta = 0, 0.25, 0.5, 0.75,$  and  $1.0$

$I_{i,j}$  is the intensity of the image  $I$  at pixel  $[i,j]$ . Let the standard deviation of the gradient in  $x$  and  $y$  directions be  $\sigma_x$  and  $\sigma_y$ , then the smoothness is  $S = \sqrt{\sigma_x^2 + \sigma_y^2}$ . Smoothness of the residual images and backgrounds of the filtered images are related to the filtering quality. The pixels of negative values and their deviation from zero can be considered in the definition of quality by simply modifying the smoothness of the background by multiplying a factor. Thus the quality of filtering process is defined as

$$Q = \frac{S_o}{S_r + S_f(k + \sigma_-)}, \quad (3.27)$$

where  $S_o$  is the smoothness of the original image,  $S_r$  is the smoothness of the residual,  $S_f$  is the smoothness of the background of the filtered result,  $k$  is a factor denoting how far the background is from the horizontal plane, and  $\sigma_-$  is the deviation of the negative values from zero. The parameter  $k$  is calculated as follows. We first calculate  $\vec{g}$  which is the gradient image, then calculate a vector having components which are

absolute values of  $\vec{g}$ . The standard deviation  $\sigma$  of this new vector is an indicator of how far the backgrounds are from horizontal plane. We define  $k$  as  $\sigma/S_f$ .

Such quality evaluations for the filtered results of fields I029, I363, I390, I391, and I108 were conducted using different partial normalization factors. We found that when the field is far from the Galactic plane, a small  $\beta$  produces maximum quality  $Q$ . For a field close to the Galactic plane, a  $\beta$  larger than 0.5 is needed to produce maximum  $Q$ . For example, the field I390 was classified and filtered using the k-means method and equal CI area method, with  $\beta = 0.00, 0.25, 0.5, 0.75$ , and 1.00. The quality of the image with  $\beta = 0.5$  is highest. Figure 3.12 shows the filtered results of I390 with  $\beta = 0.25, 0.5, 0.75$ , and 1.00. Note that when  $\beta$  is small, such as 0.25, the pixels around strongest sources were grouped into cirrus classes, thus the estimated cirrus has relatively large growths at low growth layers, which produces over-subtraction of fluxes from areas around the strongest sources (number of negative pixels with negative values increases, which lowers the quality). When  $\beta$  is very large, such as 1, the strong cirrus were treated as extended sources. Thus the cirrus components are under-estimates at low layers, which produces rough background for the filtered image ( $S_f$  increases, making  $Q$  decrease). Filtering fields I029, I363, I391, I390, and I108 with different  $\beta$  reveal that when the population of Class 5 is four times that of Class 4, the filtered images have good qualities for the fields. The above statement gives a  $\beta$  of 0 for I029, and a  $\beta$  a little bit larger than 0.5 for I390. We also found that the optimized  $\beta$  can be related to the maximum value of growths  $G_{max}$  approximately by

$$\beta = 1 - \frac{\log 25}{\log G_{max}}. \quad (3.28)$$

This formula was used to determine the partial normalization factor for all the 430

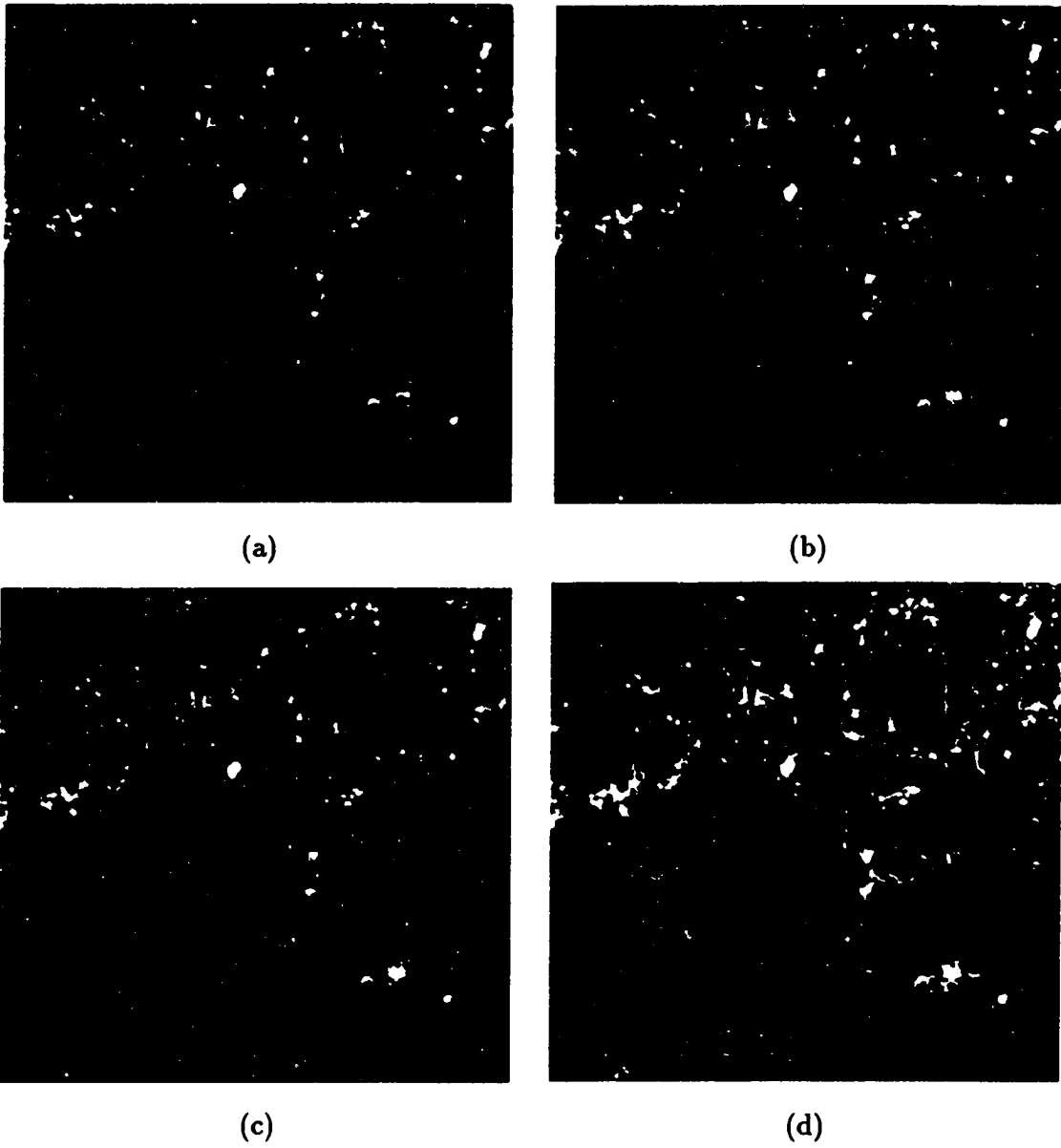


Figure 3.12: The filtered images of ISSA field I390 with  $\beta$  as: (a) 0.25; (b) 0.5; (c) 0.75; and (d) 1.0

fields of ISSA at 100  $\mu\text{m}$ .

### **Reliability of the Sources Detected from the Filtering**

The filtered images for ISSA fields show many sources which look like point sources and extended sources, especially when the fields are close to the Galactic plane. Such sources were not all detected by other methods of observation and analysis. Some of them are actually newly found sources by IRAS which was published in the IRAS Point Source Catalog (PSC). Some of them are cirrus sources [Chester 1986]. To evaluate the reliabilities of the sources found in our filtered image qualitatively, we first searched for them in the computer database called NED created by IPAC at Caltech (this database contains extragalactic sources, contact [nedbatch@ned.ipac.caltech.edu](mailto:nedbatch@ned.ipac.caltech.edu) to find more about NED). The sources not found in NED were then searched for in the IRAS PSC. For instance, the field I391 (centered at galactic latitude of  $0.0034^\circ$ , and galactic longitude of  $135^\circ$ ) was studied this way. We first threshold the image (let's denote the threshold as T). The threshold T is found by averaging the intensities at pixels in the areas of filtered image excluded of the sources. The sources are excluded by the following method. We first find the average and deviation for the whole filtered image. The pixels having intensities outside the  $1\text{-}\sigma$  regions are excluded. Exclusion process based on previous excluded image goes on until the difference of the averages between two consecutive steps is smaller than certain tolerance. When the areas occupied by extended sources were not considered, a total of 113 sources were found from the filtered image. Among them, 33 sources were found in NED (29.2%), 61 sources remaining were found in IRAS PSC (54.0%). Only 19 sources were not found (16.8%). One of the sources not

found in IRAS PSC and NED is actually a newly discovered galaxy called Dwingeloo 1, discovered by astronomers in Netherlands in Nov. 1994 [Kraan-Korteweg *et al.* 1994]. This galaxy lies behind the Galactic plane, which is in the field of I391. The position of Dwingeloo 1 in I391 contains a weak point source, which is shown at the center of Figure 3.13. Since Dwingeloo 1 is weak [Kraan-Korteweg *et al.* 1994], and the point source we obtained at the same position is weak, it is reasonable to assume that the point source we see at the position of Dwingeloo 1 is the galaxy itself. The remaining 18 sources are still under investigation at Fick Observatory. There are many sources presented in IRAS PSC not included in our 113 sources. The reasons are that we did not include the sources in the regions with diffuse emission (extended sources), that PSC used multiple coverage by the scans to detect very faint sources, and that PSC include sources detected by all the four wavelength bands.

Some of the filament structures in the filtered image correspond to dust which was already observed optically. The field I363 was filtered using  $\beta = 0.00$  and the equal CI area method. The filtered image is shown in Figure 3.14, which contains the same dust finger as observed by the optical method in POSS (Figure 3.15).

### Reliability of the Shape for a Source

From previous sections, we see that the equal CI area method, non-overlapping method and multi-cirrus filtering method preserve the FWHM better than they preserve the intensity for a source, even when sigmoidal weighing is not considered. This means the filtering applies a homogeneous scaling on intensity at each pixel of this source. Such a conclusion, however, is based on point and slightly extended sources which are Gaussian shaped. In this section, we discuss the shape retention of sources

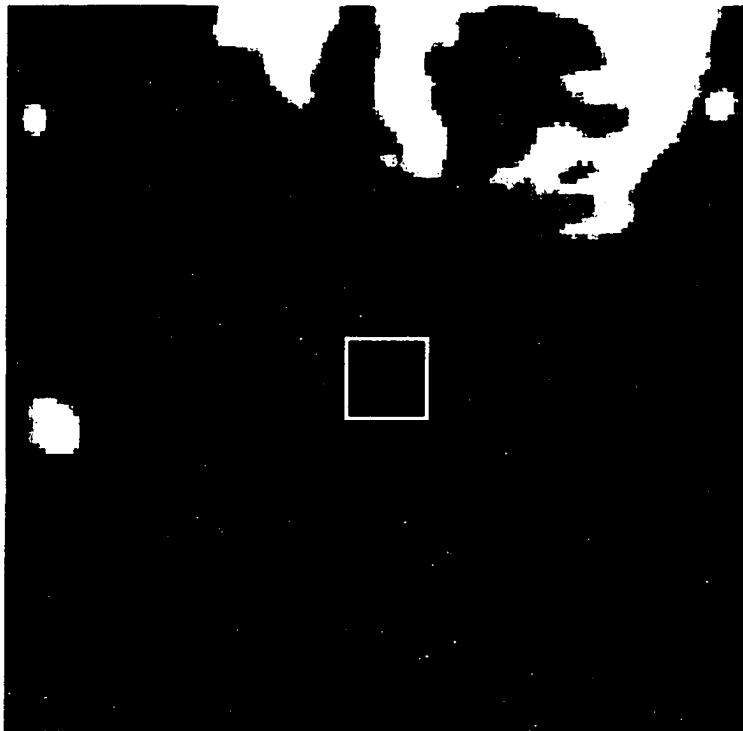


Figure 3.13: The point source at the position of Dwingeloo 1 (framed at the center)



Figure 3.14: The filtered result of field I363 using equal CI area method



Figure 3.15: The POSS plate containing the dust finger in IRAS field I363

with forms other than Gaussian shape. Intensity is not a factor in consideration here. We superpose some simulated sources onto I029, and using equal CI area method to do the filtering with the sigmoidal weighting in effect. Other filtering methods are not discussed here, because they perform similarly to equal CI area method. The resultant filtered image is observed and compared with the simulated source. Two simulated sources are made, one has the form of a square, another has the form of an ellipse. The square source is prismatic with a height of 6 (Figure 3.16(a)). When this simulated source is superposed with Figure 2.1 (I029 field) at 16 different positions, Figure 3.16(b) is obtained. Using equal CI area method as described previously in this chapter, we filter Figure 3.16(b) to obtain Figure 3.17. A comparison of the square-like sources in Figure 3.17 and Figure 3.16(a) show that the sources are not distorted too much. We use the average and the deviation of the lengths of the sides for the square-like sources to characterize the corresponding shape. If the deviation is small (compared with the average), then the shape is close to a square. For instance, the original square source has sides with average of 9.9 pixels and deviation of zero pixels. When the squares in Figure 3.17 are examined, we found that the lengths of the sides have an average of 9.85 and deviation of 0.15 pixels. That is to say, the squares in Figure 3.17 are almost perfect if only the lengths of the sides are considered. A close examination of these squares, however, reveals that the sides are slightly curved toward inside of the squares. Such effects are due to the reason that the edges of the squares are less sharp than the corners, thus they are more like cirrus pixels. A similar simulation is done with an elliptical source. This ellipse is an elongated Gaussian shaped source with a height of 6 and short axis of 3 pixels. The ratio of the long axis to the short axis is 7. Figure 3.18(a) shows this source, and

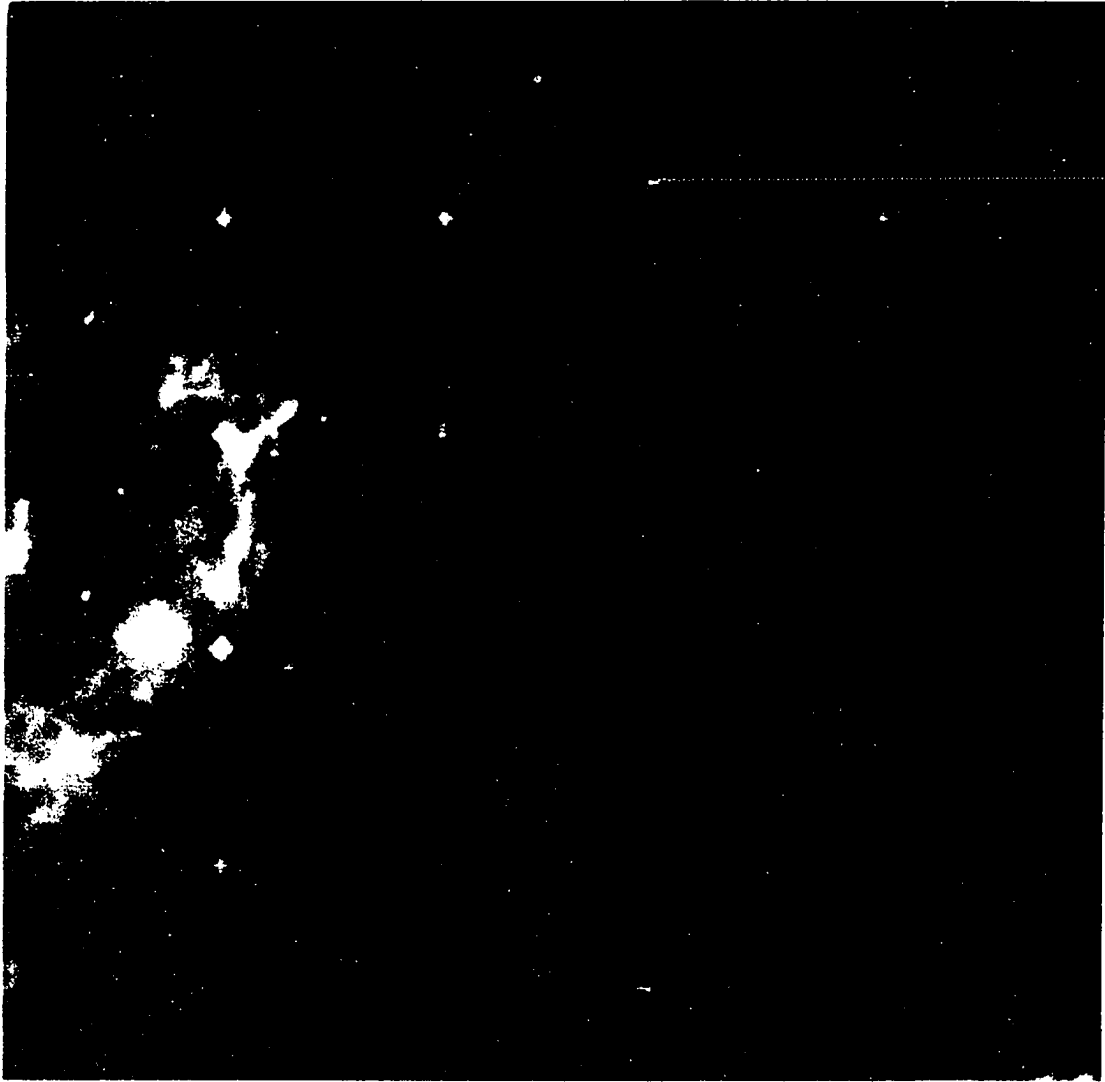
Figure 3.18(b) shows the source imposed onto I029 at 16 different positions. We filter Figure 3.18(b) using the equal CI area method, and obtain Figure 3.19. To justify how well these sources are retained in shape, we measure their ratios of long axis to short axis. It is found that their ratios have an average of 6.87 and a deviation of 0.13. Thus we conclude that the morphological methods can retain the shapes of the sources in within a few percent of error, if the sources are slightly extended square-like or ellipse-like. Other slightly extended sources can be simulated and analyzed. It is reasonable to assume that their shapes are to be retained too.

### Summary

In this chapter, we presented a self-consistent filtering process using sieving and classification. The growths from the sieving process are mapped into a feature space in order to classify them into several categories. From the classification, cirrus growths were obtained which was further used to remove the cirrus components by the equal CI area method, non-overlapping method, or multi-cirrus filtering method. Partial normalization of the growths with different normalization factors were made prior to the classification in order to find the best filtering result. Several fields were examined to relate the sources found in the filtered image with the known sources, or known dust structures.



(a)



(b)

Figure 3.16: A square-like source (a) superposed on I029 to obtain (b)

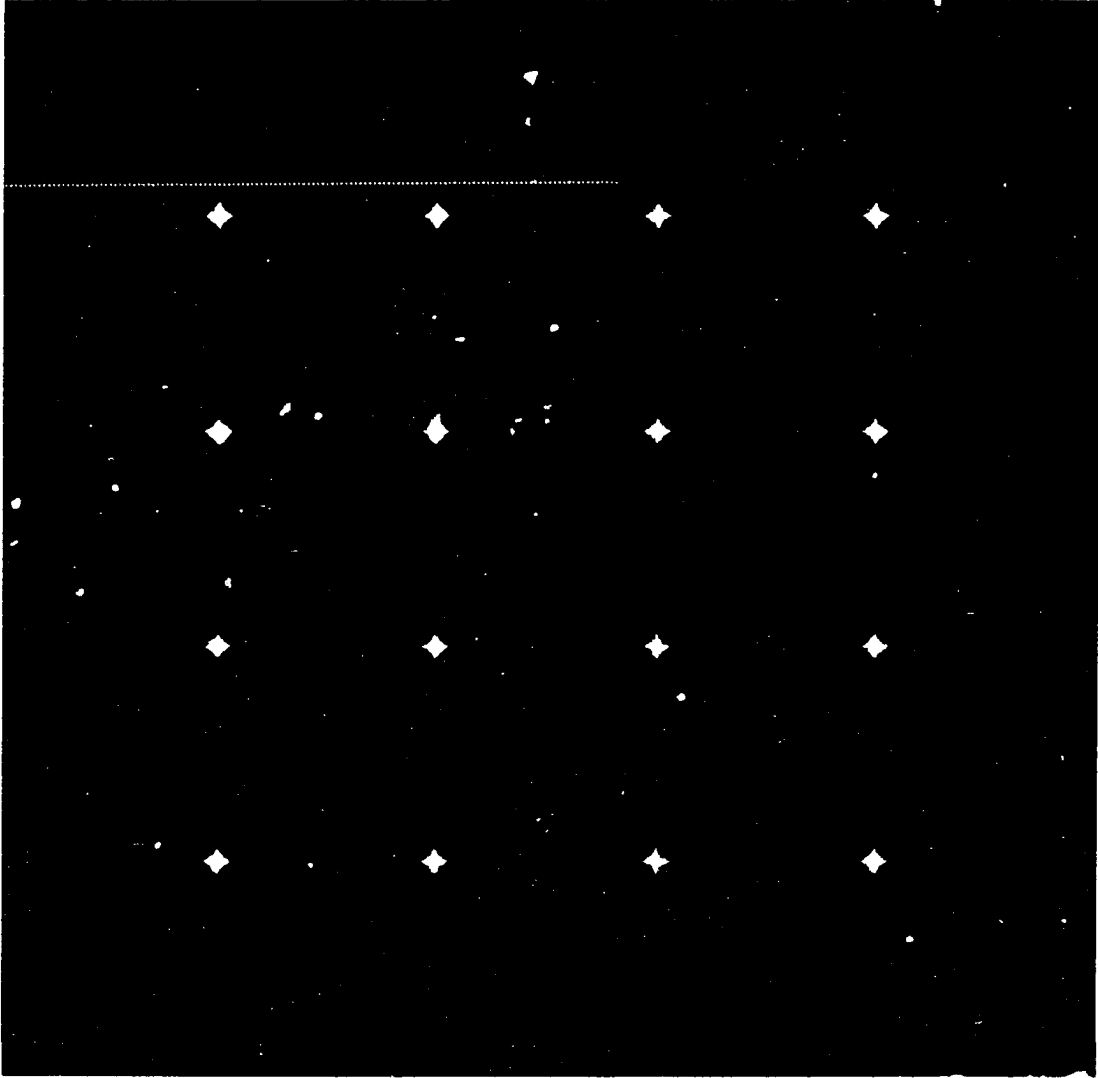


Figure 3.17: The filtered result of Figure 3.16(b) by equal CI area method



(a)



(b)

Figure 3.18: An ellipse-like source (a) superposed on I029 to obtain (b)

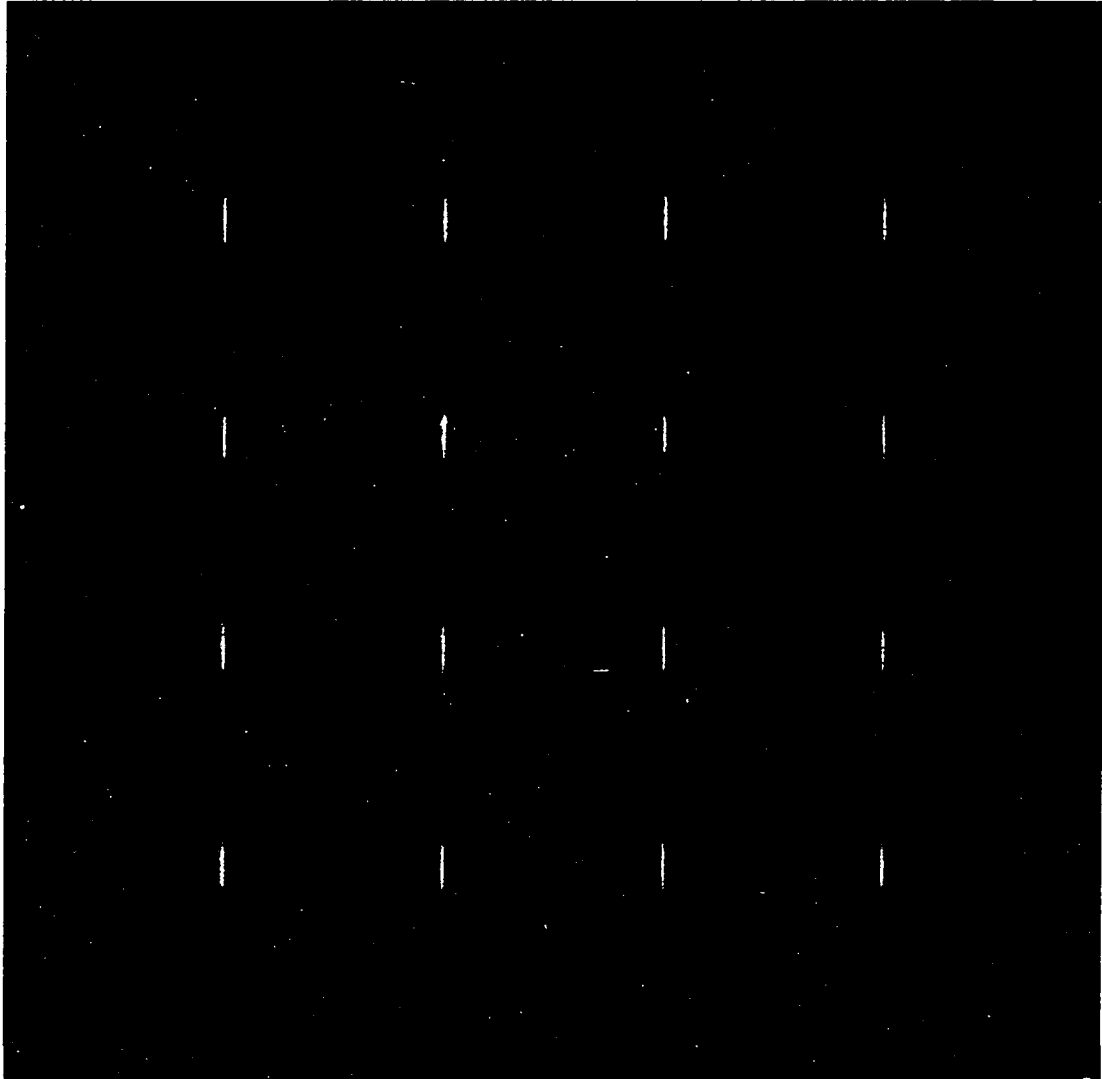


Figure 3.19: The filtered result of Figure 3.18(b) by equal CI area method

## CHAPTER 4. GRANULOMETRY AND UNI-DIRECTIONAL SIZE INFORMATION EXTRACTION

From the last chapter, we know that using the sieving process with Gaussian shaped structuring elements, we are able to remove cirrus components from an ISSA field. The choices of larger Gaussian shaped SEs at successive steps were to obtain positive growths. The experiments, however, show that some of the growths were negative. In this chapter, we show how to avoid this problem, and obtain positive growths, in terms of granulometry, and alternatively, sequential sieving. In granulometry, the SEs can be decomposed by smaller SEs using dilations. Such SEs can be used to reduce the computational time of dilation, erosion, opening and closing.

### Structuring Element Decomposition

When a bigger SE can be represented by the dilation of two or more smaller SEs, we may execute the dilation or the erosion of this bigger SE, by using dilations and erosions of these smaller SEs. For example, if an SE  $B$  is decomposed into  $B_1$  and  $B_2$  as [Serra 1982; Dougherty 1992]

$$B = B_1 \oplus B_2, \tag{4.1}$$

then

$$X \oplus B = (X \oplus B_1) \oplus \check{B}_2, \quad (4.2)$$

and

$$X \ominus B = (X \ominus B_1) \ominus \check{B}_2. \quad (4.3)$$

The sequential dilations and erosions of smaller SEs reduce the computational time. For instance, if  $B_1 = B_2$ , which is a circle with radius  $r$ , then  $B$  is a circle with radius  $2r$ . The number of computational operations on the left hand side of Equation (4.2) or (4.3) then is proportional to  $\pi(2r)^2 = 4\pi r^2$ , but on the right side it is proportional to  $\pi r^2 + \pi r^2 = 2\pi r^2$  which is one half of  $4\pi r^2$ . Thus we see that by using structuring element decomposition, we are making the morphological operations easier to calculate.

### Granulometry

One very important property of opening when  $B = B_1 \oplus \check{B}_2$  is [Serra 1982]

$$X \circ B \subset X \circ B_1. \quad (4.4)$$

This property tells us that in the sieving process, when the larger structuring element is chosen properly (which can be decomposed by smaller SEs), we will get positive growths at all the pixels positions and all the growth layers. If we have a set of SEs  $\{S_i\}, i \in \mathbb{Z}$  (integer set), with  $S_{i+1} = S_i \oplus \check{B}_i$ , then  $G_{i+1,i} = (X \circ S_i) - (X \circ S_{i+1})$  is the growth with size information between  $S_i$  and  $S_{i+1}$ .

Now let  $i$  be positive, and  $S_1$  is the origin, then (see Appendix A)

$$X \circ S_1 = X. \quad (4.5)$$

If there is a number  $N$ , such that for  $i > N$ ,  $S_i$  is large enough producing  $X \circ S_i = \emptyset$ , then

$$\bigcup_{i=1}^N G_{i+1,i} = X, \quad (4.6)$$

and

$$G_{i+1,i} \cap G_{j+1,j} = \emptyset, \quad \text{when } j \neq i, \quad (4.7)$$

The above equation can be proven as follows. Any element of  $G_{i+1,i}$  does not belong to  $X \circ S_{i+1}$ . For any  $j > i$ ,  $G_{j+1,j}$  is a subset of  $X \circ S_j$ , which is again a subset of  $X \circ S_{i+1}$  by Equation (4.4). Thus Equation (4.7) holds. Equations (4.6) and (4.7) show that the  $G_{j+1,j}$ ,  $j \in [1, 2, \dots, N]$  are non-intersecting, and complete decompositions of a signal  $X$  (complete decomposition means that there exists a reconstruction of the components which makes the original signal without error). This case of the sieving process is called granulometry [Heijmans 1994; Dougherty 1992]. When the opening is for gray-scale images, granulometry produces

$$G_{j+1,j} \geq 0, \quad j \in [1, 2, \dots, N]. \quad (4.8)$$

This property of the growth is desired for cases when size information in the image is from one direction (such as in the case of ISSA fields, the peaks are all pointing upwards).

The Gaussian shaped SEs, however, do not satisfy the requirement of granulometry. The growths produced by them are negative sometimes. For field I029, 309518 pixels in the growth cube have negative values, which is 7.7% of the total pixels of the cube. Such a small fraction of negative pixels do not distinguish this sieving process from a true granulometry significantly, thus the Gaussian sieving process can be called a quasi-granulometry process.

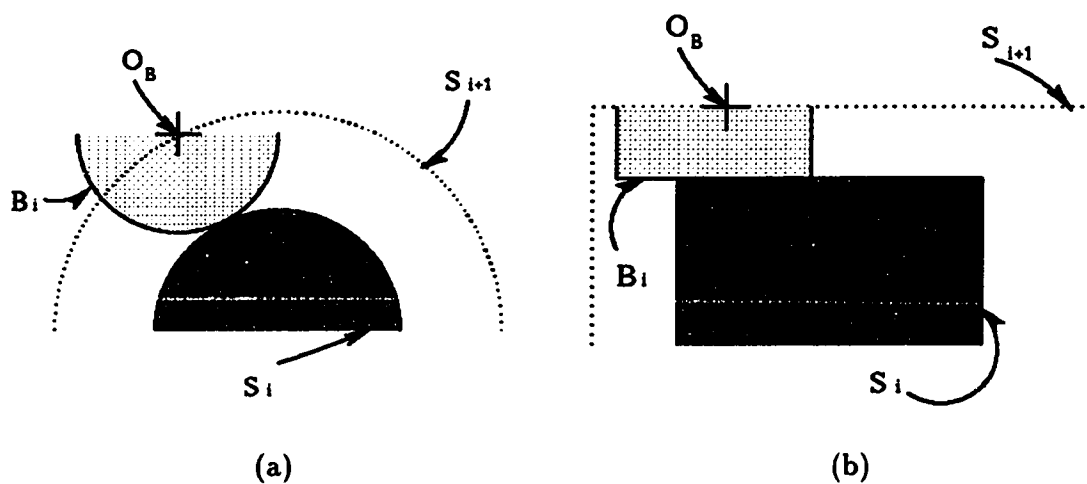


Figure 4.1: Granulometry: (a) hemispheric structuring elements; and (b) cylindric structuring elements

Two common structuring element sets satisfying the granulometry requirements are hemispheric and cylindric structuring elements. Figure 4.1 shows these structuring elements sets.

Applying hemispheric and cylindric structuring elements in the sieving process we described in the previous chapter with partial normalization factor  $\beta = 0$ , we obtain the classification of results shown in Figure 4.2.

From Figure 4.2(a), we decided to use  $CI = [8, \dots, 12]$ , and the growth for Class 4 to be the significant cirrus. Using the equal CI method and sigmoidal cirrus weighting ( $\alpha = 0.250$ ,  $\delta = 0.039$ ), we filtered Figures 2.1, 3.5(a), and 3.5(b). The filtered result of Figure 2.1 is shown in Figure 4.3, which has very similar morphology as the filtered image by Gaussian SEs. The cirrus intensity is reduced by a factor of 30 compared with original image. The fluxes of the 16 point and extended sources are measured

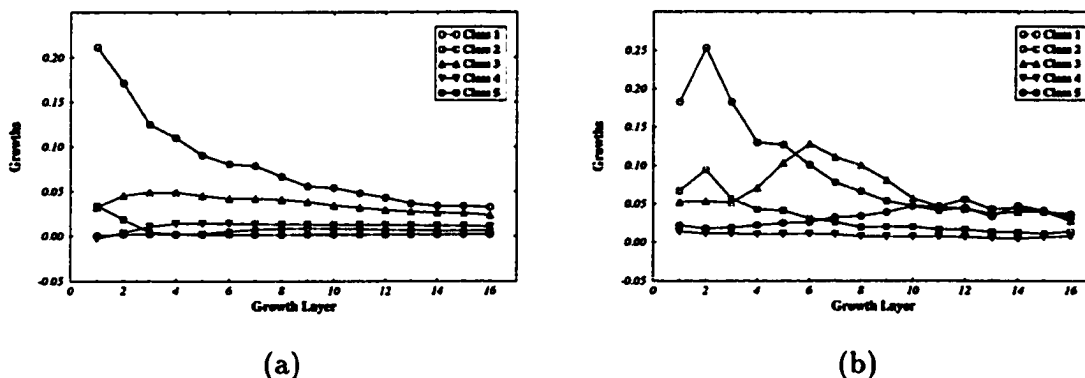


Figure 4.2: Classification results of sieving processes with: (a) hemispheric SEs; and (b) cylindric SEs

from the filtered images of Figure 3.5(a) and Figure 3.5(b). The 16 point sources have fluxes of  $57.3 \pm 2.0 \text{ MJy sr}^{-1}$  when the sigmoidal cirrus weighting is not considered, and  $61.3 \pm 2.3 \text{ MJy sr}^{-1}$  when the sigmoidal cirrus weighting is considered, i.e., the fluxes are 9%, and 2% lower than the real flux of the point sources, before and after the sigmoidal cirrus weighting. The FWHM of these sources are  $2.81 \pm 0.05$  pixels when sigmoidal weighting is not applied (giving 1.7% of total deviation from the real FWHM),  $2.86 \pm 0.05$  pixels when sigmoidal weighting is considered (giving 2.9% of total deviation from the true FWHM). For the 16 extended sources, the fluxes are  $87.7 \pm 4.4$  and  $120.1 \pm 5.0 \text{ MJy sr}^{-1}$  before and after the sigmoidal cirrus weighting, thus the corresponding errors are 46% and 27%. The FWHM of these sources are  $4.15 \pm 0.07$  pixels when sigmoidal weighting is not applied (giving 17% of total deviation from the real FWHM),  $4.47 \pm 0.07$  pixels when sigmoidal weighting is considered (giving 10.6% of total deviation from the true FWHM).

A list of the fluxes and FWHMs for these point and slightly extended sources



Figure 4.3: The filtered image of Figure 2.1 with hemispheric structuring elements using the equal CI area method

can be found in Appendix B, Table B.4.

A comparison between the present results and the results in last chapter shows that hemispheric SEs gives more distortion in both flux and FWHM.

For the cylindrical SEs, similar procedure is conducted. The filtered image of Figure 2.1 is shown in Figure 4.4, with  $\alpha = 0.243372$ , and  $\delta = 0.070$ . The filtered image has very rough background, thus the cirrus is only 7 times smaller than the original image. The reason for such behavior of the cylindric SEs are due to their low abilities of spatial discrimination as discussed in Chapter 8. The fluxes of the sources are preserved even the sigmoidal cirrus weighting is not considered. For in-

stance, the 16 point sources obtained by filtering Figure 3.5(a) have fluxes of  $61.8 \pm 3.0$  MJy sr<sup>-1</sup> (which is only 1.5% lower than the real flux) before sigmoidal weighting is considered. The FWHM is  $2.96 \pm 0.08$  pixels (6% of total deviation from the true FWHM). When sigmoidal weighting is considered, the fluxes and FWHM for the point sources are  $64.2 \pm 4.7$  MJy sr<sup>-1</sup> (7.6% total deviation from the true flux) and  $2.94 \pm 0.06$  pixels (5.4% total deviation from the true FWHM), respectively. The 16 extended sources obtained by filtering Figure 3.5(b) without sigmoidal weighting have fluxes of  $164.4 \pm 9.9$  MJy sr<sup>-1</sup>, which is only smaller than the real flux by 0.6%, and have FWHM of  $4.97 \pm 0.13$  pixels (a total deviation from the true FWHM of 2.6%). When sigmoidal weighting is considered, their fluxes and FWHMs are  $167.0 \pm 6.0$  MJy sr<sup>-1</sup> (total deviation of 4%) and  $5.08 \pm 0.06$  pixels (total deviation of 2%). It is obvious that the cylindric SEs with the sizes as the Gaussian SEs are able to extract more size information from objects in an image, thus the fluxes of the extended sources can be preserved. The cylindric SEs, however, have lower abilities to discriminate spatial structures (see Chapter 8), thus the cirrus are still strong when filtered. One way to get around this problem is to increase the number of classes in the classification, thus multi-cirrus filtering process will remove cirrus components differently one pixel from another using the corresponding cirrus response.

A list of the fluxes and FWHMs for these point and slightly extended sources can be found in Appendix B, Table B.5.

### **Uni-directional Size Information Extractors**

As we saw from previous sections, granulometry produces non-intersecting and complete basis. In gray-scale morphology, such basis produced non-negative growths.



**Figure 4.4:** The filtered image of Figure 2.1 with cylindric structuring elements using the equal CI area method

In this case, we call granulometry a uni-directional size information extractor (SIE), because it only extracts size information from one direction. Granulometry is just one example of the uni-directional SIEs, it extracts size information from the positive direction. More specifically, we can call it a positive-directional SIE (p-directional SIE). When a uni-directional SIE extracts negative size information, we call it a negative-directional (or n-directional) SIE. When  $S_{i+1} = S_i \oplus \tilde{B}_i$ , the growths  $G_{i+1,i} = X \bullet S_i - X \bullet S_{i+1}$  are n-directional SIEs. This is because  $X \bullet S_i \subset X \bullet S_{i+1}$ , thus in gray-scale morphology,  $G_{i+1,i} \leq 0$  always, which is an n-directional SIE.

Beside granulometry, it is possible to form uni-directional SIEs using any SE set  $S_i$ . The design of the uni-directional SIEs can be easily accomplished by using a sequential sieving process. In the sequential sieving process, at each step, we sieve out structures of certain sizes from the image which was sieved by smaller SIEs. This differs from the sieving process in the ASB filter design, which sieves all the size information from the original image. The sieving process in the ASB filter can be called a parallel sieving process, in which multiple sieves can be applied to the same image at the same time. The sequential sieving process is like sieving of sand. Smaller grains are sieved out first, and the material left are sieved using a large sieve to obtain larger grains.

For a sequential sieving process, let the SIE at step  $i$  be  $\mathcal{E}_i$ , the image at step  $i$  to be sieved be  $I_i$ , also let  $I_1 = I_o$  (the original image) then for  $i = 1, 2, \dots$ , we have

$$\begin{cases} I_{i+1} &= I_i - \mathcal{E}_i(I_i), \\ G_{i+1,i} &= I_i - I_{i+1}, \end{cases} \quad (4.9)$$

where  $\mathcal{E}_i(I_i)$  is the size information of  $I_i$  extracted by  $\mathcal{E}_i$ , and  $G_{i+1,i}$  is the growth. In the above equations, if  $\mathcal{E}_i(I) \geq 0$  for any image  $I$ , then  $G_{i+1,i} \geq 0$  always holds, i.e.,

$\mathcal{E}_i, i \in [1, 2, \dots]$  are uni-directional SIEs. Also note that for  $i = 1, 2, \dots, N - 1$ , we have  $I_o = \sum_{i=1}^{N-1} G_{i+1,i} + I_N$ , thus  $G_{i+1,i}, i = 1, 2, \dots, N - 1$  and  $I_N$  form an complete basis.

An example of the uni-directional SIEs in this approach is

$$\mathcal{E}_i(I_i) = I_i \circ S_i, \quad (4.10)$$

with  $\{S_i\}$  being any set of SEs. For instance, the SE set can be chosen as Gaussian in the ASB sieving process. In this case, the growths were calculated here by a sequential sieving process, and then classified by the same methods as we described in Chapter 3. Figure 4.5 shows the growths of the classes after classification with  $\beta = 0.00$ . From the figure, a  $CI = [10, \dots, 16]$  is chosen, Class 3 is selected as the most significant cirrus. The filtering method was the equal CI area method with sigmoidal weighting ( $\alpha = 0.360$  and  $\delta = 0.212$ ) applied. Figure 4.6 shows the filtered result of Figure 2.1. It looks similar to the filtered results by Gaussian and hemispheric parallel sieving. The cirrus is reduced by a factor of around 20 in this case. Also Figure 3.5(a) and 3.5(b) were filtered in the same way. The fluxes of the 16 point sources before and after the sigmoidal cirrus weighting are  $51.2 \pm 1.8$  and  $58.8 \pm 2.3$  MJy sr<sup>-1</sup>, i.e, they are 18% and 6.0% lower than the real flux of the source, respectively. The FWHM of these sources are  $2.74 \pm 0.03$  pixels when sigmoidal weighting is not applied (giving 3.7% of total deviation from the real FWHM),  $2.81 \pm 0.04$  pixels when sigmoidal weighting is considered (giving 1.4% of total deviation from the true FWHM).

The 16 extended sources have  $61.2 \pm 6.2$  and  $110.9 \pm 7.7$  MJy sr<sup>-1</sup>, before and after the sigmoidal cirrus weighting, i.e., they are 63% and 33% lower than the real flux. The FWHM of these sources are  $3.84 \pm 0.08$  pixels when sigmoidal weighting is not applied (giving 23% of total deviation from the real FWHM),  $4.31 \pm 0.07$  pixels when sigmoidal weighting is considered (giving 14% of total deviation from the true

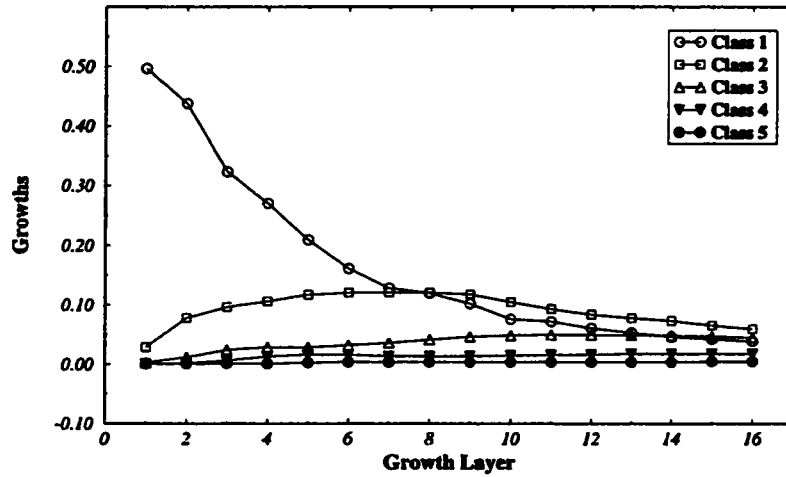


Figure 4.5: The growths of different classes of sequential sieving process

FWHM).

The lower fluxes compared with the corresponding (i.e., using the same SEs) parallel sieving is due to the relative low extraction speed of the same SEs in the sequential method, the reason may be that the information of small sizes escaped in previous sieving are not captured in later extractions.

A list of the fluxes and FWHMs for these point and slightly extended sources can be found in Appendix B, Table B.6.



**Figure 4.6:** The filtered image of Figure 2.1 by sequential sieving process, Gaussian SEs, equal CI area method, and sigmoidal noise weighting

## CHAPTER 5. GENERALIZED HIT-OR-MISS TRANSFORM AND RELATED NON-LINEAR FILTERS

In the previous chapters, I have been discussing about using opening to extract size information (sieving process). When the SEs in the ASB sieving process were chosen properly, we obtained positive size information (one example is granulometry). In the sequential sieving process, the uni-directional SIEs can be obtained more easily than in the parallel sieving process since the SEs are arbitrary. These uni-directional SIEs have their advantages in that they can extract the size information from the positive and negative directions separately (for a p-directional extractor  $\mathcal{E}$ , the extraction  $-\mathcal{E}(-I)$  is the negative size information of image  $I$ ), thus we have one more degree of freedom in processing the data. The disadvantages of the uni-directional SIEs are that when size information from both directions needs to be considered, double calculations are involved, since p- and n-directional size information are calculated separately.

When size information from both the p- and n-directions are required, SIEs able to extract size information from both directions *at the same time* are desired. Such SIEs are called *bi-directional*. In this chapter, we generalize the morphological operations to explore both uni- and bi-directional SIEs by generalizing the sieving process. Remember that when the SEs are  $S_{i+1} = S_i \oplus \check{B}_i$ , we use the opening

(closing) to extract p-directional (n-directional) size information. If we can introduce a parameterized operator that unifies closing and opening, then by changing the parameter, one can use this operator in the sieving process to obtain bi-directional SIEs.

The ordered statistic filters took erosion and dilation as special examples [Magaros and Schafer 1987], thus parameterization of closing or opening based on order statistic filters is one clue to the parameterized operator discussed in last paragraph.

This chapter generalizes the concept of the hit-or-miss transform, which took order statistic filters as special examples. The order statistic filters introduced by the generalized hit-or-miss transform are parameterized by  $\gamma \in (0, 1)$ . We call them  $\gamma$ -erosions, because when  $\gamma$  equals  $1^-$ , the order statistic filter is erosion, when  $\gamma$  equals  $0^+$ , the order statistic filter is dilation.  $\gamma$ -erosion is further used in the parameterization of closing (called  $\gamma$ -closing). When  $\gamma = 0^+$ ,  $\gamma$ -closing is traditional opening, when  $\gamma = 1^-$ ,  $\gamma$ -closing is traditional closing. Replacing opening in the sieving process of Chapters 2, 3, and 4, by  $(1 - \gamma)$ -closing, we obtain the  $\gamma$ -sieving process, which is bi-directional. The relative abilities of the extraction from p- and n-directions are discussed with the concept *polarity*, which is closely related to  $\gamma$ .

### Parameterized Erosion and Closing

The basic morphological operations are erosion and its dual dilation. Erosion can be considered as a special example of the hit-or-miss transform as discussed in Appendix A. In the hit-or-miss transform, there is a structuring element  $B = (B^1, B^2)$  which is a pair of sets. To obtain the hit-or-miss transform of a set  $X$  by  $B$  (denoted as  $X \circledast B$ ), we first relate each element  $x$  in the whole set (universe) by a pair of

sets  $(B_x^1, B_x^2)$  (where  $B_x^i$  is the translation of  $B^i$  by  $x$ , thus  $(B_x^i)_{-x} = B^i$ ), then judge whether  $B_x^1 \subset X$  and  $B_x^2 \subset X^c$  hold. If yes, then  $x$  is an element of  $X \circledast B$ .

### Generalized (dynamic) hit-or-miss transform

To generalize the hit-or-miss transform, we do not wish to constrain the SE  $B$  to be a pair of sets. Thus, we assume that  $B$  could be a set or pair of sets. Relating to each element  $x$  in the universe is  $(B^1(x), B^2(x))$  ( $[B^i(x_1)]_{-x_1} \neq [B^i(x_2)]_{-x_2}$ ). The judges  $B_x^1 \subset X$  and  $B_x^2 \subset X^c$  in the traditional hit-or-miss transform are replaced by two relation kernels  $\mathcal{R}_1(B^1(x), B^2(x), x, X, B)$  and  $\mathcal{R}_2(B^1(x), B^2(x), x, X, B)$ . Of course, the traditional hit-or-miss transform is a special example of such generalization. Thus we define the generalized (or dynamic) hit-or-miss transform as the following.

**Definition 5.1** *Let the universe in consideration be  $E = \{x\}$ . There is a constant structuring element  $B$  which could be a set or pair of sets. The set in consideration is  $X$ . For each element  $x \in E$ , there are two sets  $B^1(x)$  and  $B^2(x)$  relating to it which are functions of  $x, X$ , and  $B$ . The dynamic hit-or-miss transform of  $X$  by structuring element  $B$  is defined as*

$$X \circledast B = \{x : \mathcal{R}_1(B^1(x), B^2(x), x, X, B); \mathcal{R}_2(B^1(x), B^2(x), x, X, B); x \in E\}, \quad (5.1)$$

where  $\mathcal{R}_1$  and  $\mathcal{R}_2$  are two relation kernels which define whether the sets obey the corresponding relationships. In the traditional hit-or-miss transform, structuring element is  $B = (B^1, B^2)$ , the pair of sets relating to  $x$  is  $(B^1(x), B^2(x)) = (B_x^1, B_x^2)$ , the relation kernels  $\mathcal{R}_1$  and  $\mathcal{R}_2$  are  $B^1(x) \subset X$ , and  $B^2(x) \subset X^c$ .

### $\gamma$ -erosion and $\gamma$ -closing

The dynamic hit-or-miss transform is able to form the order statistic filters which bridges the erosion and dilation. We call this operation  $\gamma$ -erosion, with  $\gamma \in [0^+, 1^-]$ . The definition of  $\gamma$ -erosion is as following.

**Definition 5.2** *Let the universe be  $E = \{x\}$ . If the set  $E$  is countable, and the operator  $\mathcal{N}$  finds the number of elements of a set, then the  $\gamma$ -erosion of set  $X$  with structuring element  $B$  (which is a set instead of pair of sets in traditional hit-or-miss transform) and a parameter  $\gamma \in [0^+, 1, \dots, \mathcal{N}(B)^-] / \mathcal{N}(B)$  is denoted as  $\mathcal{E}_\gamma$  and defined by dynamic hit-or-miss transform with  $B^1(x) = B_x \cap X$ ,  $B^2(x) = B_x \cap X^c$ ,  $\mathcal{N}(B^1(x)) > \gamma \mathcal{N}(B)$ , and  $\mathcal{N}(B^2(x)) \leq (1 - \gamma) \mathcal{N}(B)$ .*

With the numbers of elements for the sets  $B$  and  $X$  being infinite, we still can extend the concept of  $\gamma$ -erosion.

**Definition 5.3** *If the numbers of elements in structuring element  $B$  and set  $X$  are infinite with the density function for the distribution of elements in  $B$  being known, and if operator  $\mathcal{A}$  is able to find the volume of the density function for the sets, then the  $\gamma$ -erosion  $\mathcal{E}_\gamma$ ,  $\gamma \in (0, 1)$  is defined by the dynamic hit-or-miss transform similar to Definition (5.2) with  $\mathcal{N}$  substituted by  $\mathcal{A}$ .*

It is not very difficult to show that

$$\mathcal{E}_{0^+}(X, B) = X \ominus B, \quad (5.2)$$

and

$$\mathcal{E}_{1^-}(X, B) = X \oplus B. \quad (5.3)$$

Figure 5.1 is an illustration of how  $\mathcal{E}_\gamma$  works with  $\gamma = 0^+, 0.5$  and  $1^-$ . Set  $X$  is denoted as  $X$ , the circle  $B$  stands for the structuring element with its center at the origin (Figure 5.1(a)). In Figure 5.1(b), the dotted line was obtained using  $\mathcal{E}_{1^-}(X, B)$  which is actually an erosion (note that the long rectangle pointing outward was removed, but the long rectangle pointing inward produced a huge hole). The dotted line in Figure 5.1(c) was obtained by  $\mathcal{E}_{0.5}(X, B)$  (note that the corners, long rectangles pointing outward and inward are all smoothed away). Finally, the dotted line in Figure 5.1(d) is the dilation of  $X$  by  $B$  which was obtained by  $\mathcal{E}_{0^+}(X, B)$  (note that long rectangle pointing inward is gone, and the long rectangle pointing outward produces a huge bump).

The  $\gamma$ -erosion has nice properties such as monotonically increasing and translation invariant (for these concepts, please refer to [Serra 1982; Heijmans 1994; Dougherty 1992]). Also it is decreasing with respect to  $\gamma$ .

**Proposition 5.1** *The  $\gamma$ -erosion has following properties.*

(1)  $\mathcal{E}_\gamma(X, B) = [\mathcal{E}_{1-\gamma}(X^c, B)]^c$ , i.e.,  $\mathcal{E}_\gamma$  and  $\mathcal{E}_{1-\gamma}$  are dual operators (see Appendix A for the concept of duality).

(2)  $\mathcal{E}_\gamma$  is monotonically increasing, i.e., for  $X \supset Y$ , the following holds

$$\mathcal{E}_\gamma(X, B) \supset \mathcal{E}_\gamma(Y, B). \quad (5.4)$$

(3)  $\mathcal{E}_\gamma$  is translation invariant, i.e.,

$$\mathcal{E}_\gamma(X_y, B) = [\mathcal{E}_\gamma(X, B)]_y. \quad (5.5)$$

(4) For  $\gamma_1 < \gamma_2$ , we have

$$\mathcal{E}_{\gamma_1}(X, B) \supset \mathcal{E}_{\gamma_2}(X, B). \quad (5.6)$$

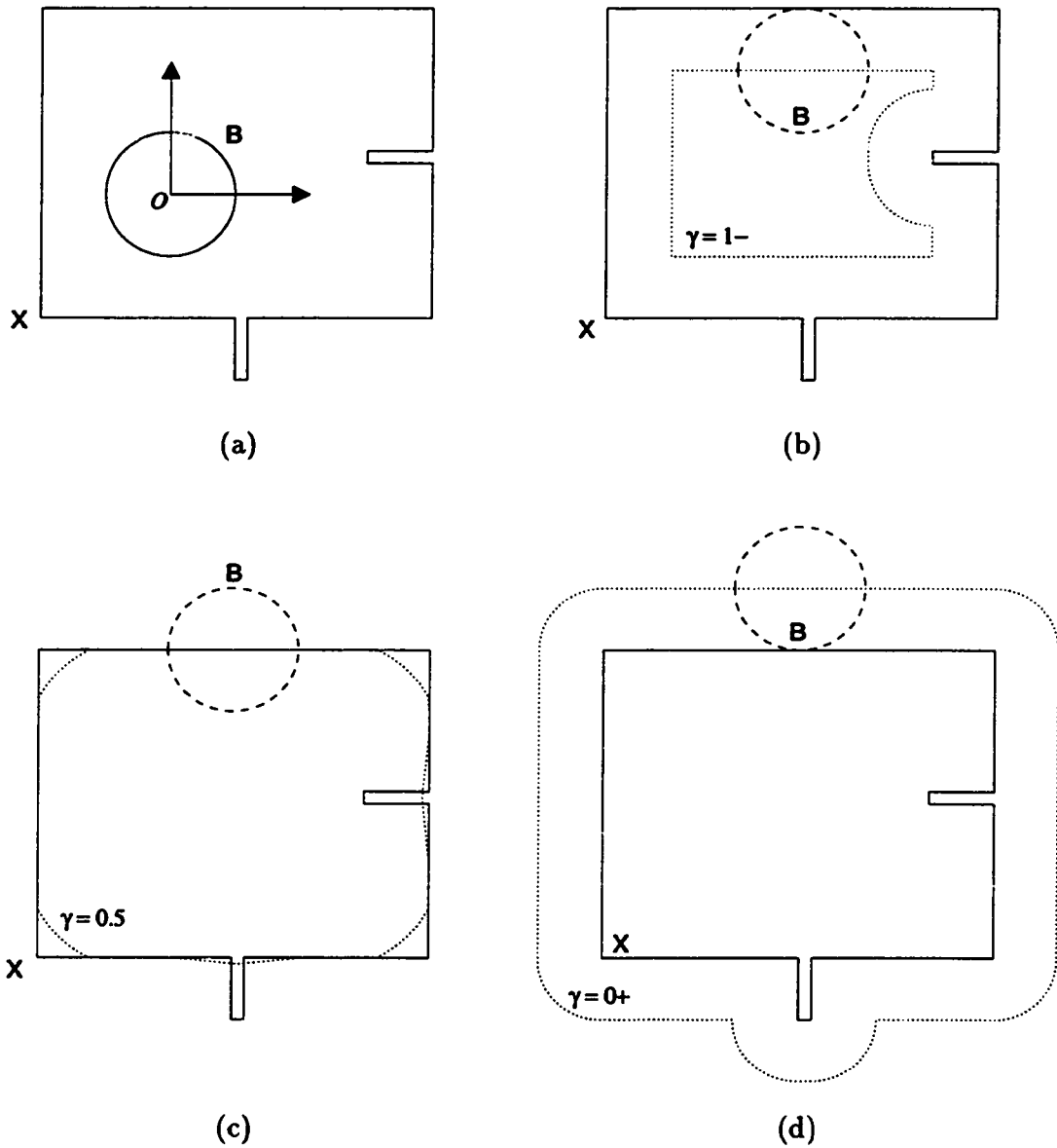


Figure 5.1: Illustrations of  $\mathcal{E}_\gamma$  with  $\gamma = 1-, 0.5$  and  $0+$ : (a) letter  $X$  represents the set  $X$ , circle  $B$  represents the structuring element; (b)  $\mathcal{E}_{1-}(X, B)$  which is actually erosion; (c)  $\mathcal{E}_{0.5}(X, B)$ ; and (d)  $\mathcal{E}_{0+}(X, B)$  which is the same as dilation

**Proof:**

Without loss of generality, we assume that the structuring element has finite elements.

We define  $B^1$  and  $B^2$  as in Definition (5.2).

(1) First, we define a set  $X^\beta$  which is a subset of the universe  $E$ ,

$$X^\beta = \{x : \mathcal{N}(B^1(x))/\mathcal{N}(B) = \beta\}. \quad (5.7)$$

Note that

$$\begin{aligned} X^\beta &= \{x : \mathcal{N}(B^2(x))/\mathcal{N}(B) = 1 - \beta\} \\ &= (X^c)^{(1-\beta)}. \end{aligned} \quad (5.8)$$

Now we have

$$\bigcup_{\beta=0}^1 X^\beta = E, \quad (5.9)$$

i.e.,

$$\mathcal{E}_\gamma(X, B) = \bigcup_{\beta=\gamma}^1 X^\beta \quad (5.10)$$

$$= \left[ \bigcup_{\beta=0}^{\gamma} X^\beta \right]^c \quad (5.11)$$

$$= \left[ \bigcup_{\beta=0}^{\gamma} (X^c)^{(1-\beta)} \right]^c \quad (5.12)$$

$$\stackrel{\beta_1=1-\beta}{=} \left[ \bigcup_{\beta_1=1-\gamma}^1 (X^c)^{\beta_1} \right]^c \quad (5.13)$$

$$= [\mathcal{E}_{1-\gamma}(X^c, B)]^c. \quad (5.14)$$

(2) Since  $X \supset Y$ , for  $x \in \mathcal{E}_\gamma(Y, B)$ , we have  $B^1(x) = B_x \cap X \subset B \cap Y$ , therefore,

since

$$\mathcal{N}(B_x \cap Y)/\mathcal{N}(B) > \gamma, \quad (5.15)$$

we have

$$\mathcal{N}(B_x \cap X) / \mathcal{N}(B) > \gamma. \quad (5.16)$$

By Definition (5.2) and above equations, we have  $\mathcal{E}_\gamma(X, B) \supset \mathcal{E}_\gamma(Y, B)$ .

(3) Since  $\mathcal{E}_\gamma(X, B) = \bigcup_{\beta=\gamma}^1 X^\beta$ , we have

$$\mathcal{E}_\gamma(X_y, B) = \bigcup_{\beta=\gamma}^1 (X_y)^\beta. \quad (5.17)$$

It is easy to show that

$$(X_y)^\beta = [X^\beta]_y, \quad (5.18)$$

therefore

$$\begin{aligned} \mathcal{E}_\gamma(X_y, B) &= \bigcup_{\beta=\gamma}^1 [X^\beta]_y \\ &= \left[ \bigcup_{\beta=\gamma}^1 X^\beta \right]_y \\ &= [\mathcal{E}_\gamma(X, B)]_y. \end{aligned} \quad (5.19)$$

(4) For  $\gamma_1 < \gamma_2$ ,

$$\begin{aligned} \mathcal{E}_{\gamma_1}(X, B) &= \bigcup_{\beta=\gamma_1}^1 X^\beta \\ &= \left( \bigcup_{\beta=\gamma_2}^1 X^\beta \right) \cup \left( \bigcup_{\beta=\gamma_1}^{\gamma_2} X^\beta \right) \\ &\supset \bigcup_{\beta=\gamma_2}^1 X^\beta = \mathcal{E}_{\gamma_2}(X, B). \end{aligned} \quad (5.20)$$

It is straightforward to define opening and closing with a parameter  $\gamma$  using the  $\gamma$ -erosion operator  $\mathcal{E}_\gamma$ . We define an operator  $\gamma$ -closing with parameter  $\gamma$ ,  $\mathcal{C}_\gamma$  as

$$\mathcal{C}_\gamma = \mathcal{E}_\gamma(\mathcal{E}_{1-\gamma}(X, B), \check{B}). \quad (5.21)$$

Traditional closing corresponds to  $\mathcal{C}_{1-}$  and the traditional opening corresponds to  $\mathcal{C}_{0+}$ , i.e.,

$$\mathcal{C}_{1-}(X, B) = X \bullet B, \quad (5.22)$$

$$\mathcal{C}_{0+}(X, B) = X \circ B. \quad (5.23)$$

The readers is encouraged to find the results of  $\gamma$ -closing with the application of  $\mathcal{E}_{1-\gamma}$  on the dotted lines in Figures 5.1(b), 5.1(c), and 5.1(d).

The  $\gamma$ -closing is also monotonically increasing, and translation invariant.

**Proposition 5.2**  *$\gamma$ -closing has following properties.*

(1)  $\mathcal{C}_{\gamma}(X, B) = [\mathcal{C}_{1-\gamma}(X^c, B)]^c$ , i.e.,  $\mathcal{C}_{\gamma}$  and  $\mathcal{C}_{1-\gamma}$  are dual operators.

(2)  $\mathcal{C}_{\gamma}$  are monotonically increasing, i.e., for  $X \supset Y$ , the following holds

$$\mathcal{C}_{\gamma}(X, B) \supset \mathcal{C}_{\gamma}(Y, B). \quad (5.24)$$

(3)  $\mathcal{C}_{\gamma}$  is translation invariant, i.e.,

$$\mathcal{C}_{\gamma}(X_y, B) = [\mathcal{C}_{\gamma}(X, B)]_y. \quad (5.25)$$

These propositions can be proven straight forwardly by the propositions of  $\gamma$ -erosion.

The  $\gamma$ -erosion and  $\gamma$ -closing can be represented by the Matheron representation [Matheron 1975; Serra 1982; Dougherty 1992]. In the Matheron representation, for a translation invariant and monotonically increasing operator  $\Psi$  with structuring element  $B$ , there exists a *kernel* defined by

$$\text{Ker}[\Psi(\cdot, B)] = \{A : 0 \in \Psi(A, B)\}, \quad (5.26)$$

where  $0$  is the origin. Application of  $\Psi$  onto  $X$  can be represented by the union of the traditional erosion with elements in  $Ker[\Psi(\cdot, B)]$ , i.e.,

$$\Psi(X, B) = \bigcup \{X \ominus C : C \in Ker[\Psi(\cdot, B)]\} \quad (5.27)$$

The above equation can also be represented by the kernel of the dual operator of  $\Psi$ , i.e.,  $Ker[\Psi^*(\cdot, B)]$ , with the following equation

$$\Psi(X, B) = \bigcap \{X \oplus C : C \in Ker[\Psi^*(\cdot, B)]\} \quad (5.28)$$

### Parameterized Gray-scale Erosion and Closing

In last section, we described the parameterization of erosion and closing from a set point of view. Such parameterization can be easily extended into the area of gray-scale morphology. Instead of the number counting for sets, we use the definition domain length in the relation kernels.

**Definition 5.4** *If a function  $f(x)$  has finite definition domain length  $\mathcal{L}(f)$ , the length of the definition domain with  $f(x) \geq 0$  is  $\mathcal{L}^+(f)$ , and the length of definition domain with  $f(x) < 0$  is  $\mathcal{L}^-(f)$ , then*

$$\mathcal{L}(f) = \mathcal{L}^+(f) + \mathcal{L}^-(f) \quad (5.29)$$

With the help of the definitions above, we define  $\gamma$ -erosion of the gray-scale images as following:

**Definition 5.5** *The  $\gamma$ -erosion of the gray-scale image  $f(x)$  by the structuring element  $g(x)$  is defined as*

$$\mathcal{E}_\gamma(f, g)(x) = \{y : \mathcal{L}^+(f - g_x - y) / \mathcal{L}(g) = \gamma\} \quad (5.30)$$

where  $\gamma \in (0, 1)$ .

Gray-scale  $\gamma$ -erosion has similar properties as those of  $\gamma$ -erosion discussed in the previous section.

**Proposition 5.3** *Gray-scale  $\gamma$ -erosion has the following properties:*

(1)  $\mathcal{E}_\gamma(f, g) = -[\mathcal{E}_{1-\gamma}(-f, -g)]$ , i.e.,  $\mathcal{E}_\gamma(f, g)$  and  $\mathcal{E}_{1-\gamma}(f, \check{g})$  are dual operations.

(2)  $\mathcal{E}_\gamma$  are monotonically increasing, i.e., for  $f_1 \gg f_2$ , the following holds

$$\mathcal{E}_\gamma(f_1, g) \gg \mathcal{E}_\gamma(f_2, g), \quad (5.31)$$

where  $f \gg g$  means that  $f$  lies above  $g$ .

(3)  $\mathcal{E}_\gamma$  is translation invariant, i.e.,

$$\mathcal{E}_\gamma(f_{(x_0, y_0)}, g) = [\mathcal{E}_\gamma(f, g)]_{(x_0, y_0)}. \quad (5.32)$$

where  $f_{(x_0, y_0)}(x) = f(x - x_0) + y_0$ .

(4) For  $\gamma_1 < \gamma_2$ , we have

$$\mathcal{E}_{\gamma_1}(f, g) \gg \mathcal{E}_{\gamma_2}(f, g). \quad (5.33)$$

The proof can be conducted without too much difficulty.

It is obvious that  $\mathcal{E}_{1-}(f, g) = f \ominus g$ , and  $\mathcal{E}_{0+}(f, g) = f \oplus \check{g}$ . The operation  $\mathcal{E}_{0.5}(f, g)$  represents the median filter with a structuring element  $g$ . When  $g \equiv 0$ ,  $\mathcal{E}_{0.5}(f, g)$  is the same as the traditional median filter.

To verify how  $\gamma$ -erosion treats noise, an image extracted from ISSA I029 field (Figure 5.2(a)) is corrupted by spike noise to obtain Figure 5.2(b). We then applied  $\mathcal{E}_\gamma$  to Figure 5.2(b), using a  $3 \times 3$  structuring element flat on the top (constant values at all the pixels). Since  $\mathcal{E}_\gamma$  and  $\mathcal{E}_{1-\gamma}$  are duals, only results with  $\gamma \leq 0.5$  need

to be shown. Figure 5.3 shows the results of  $\gamma$ -erosion with  $\gamma = 0^+, 1/9, 3/9,$  and  $4/9$ . When  $\gamma = 0^+$ ,  $\mathcal{E}_\gamma$  is traditional dilation, which removes the n-directional noise, but enlarges the areas for the p-directional spikes. When  $\gamma = 1/9$ , the  $\gamma$ -erosion diffuses the sources and background. When  $\gamma$  changes from  $3/9$  to  $4/9$ , the diffusion effects became smaller and smaller. A comparison of Figure 5.3 and Figure 5.2(a) reveals that when  $\gamma = 4/9$ , the spike noise is totally removed, the diffusion effects are smallest, and the  $\gamma$ -eroded image (Figure 5.3(d)) is closest to the original image Figure 5.2(a).

The  $\gamma$ -closing can be extended in a similar fashion.

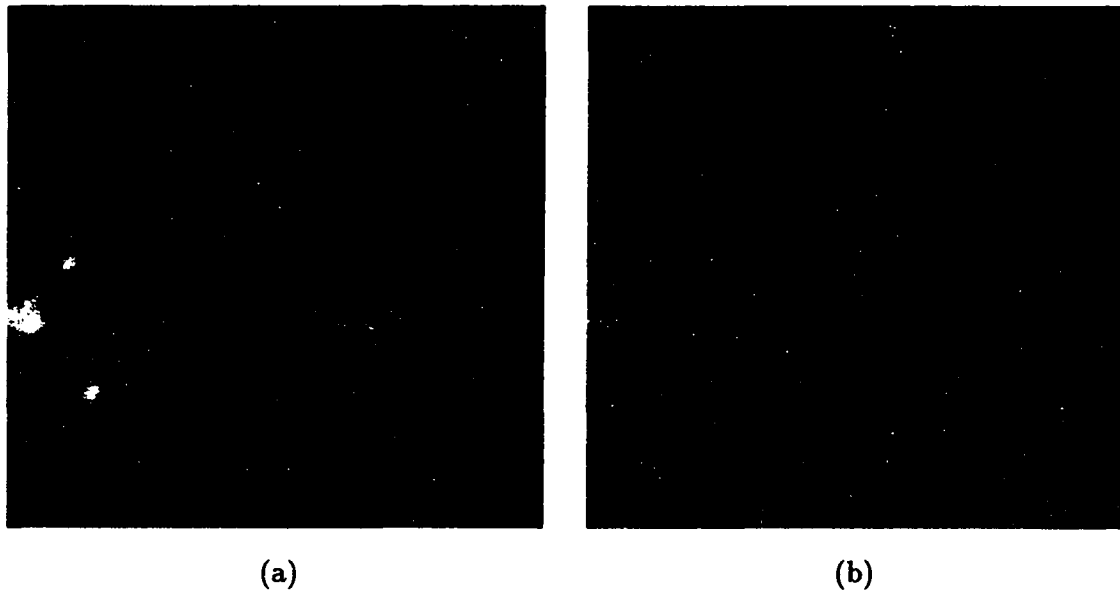


Figure 5.2: An image from the IRAS database: (a) original; and (b) corrupted by spike noise

**Definition 5.6**  $\gamma$ -closing of image  $f(x)$  by the structuring element  $g(x)$  is denoted as  $\mathcal{C}_\gamma$  and defined as

$$\mathcal{C}_\gamma(f, g) = \mathcal{E}_\gamma(\mathcal{E}_{1-\gamma}(f, \check{g}), g), \quad (5.34)$$

where  $\gamma \in (0^+, 1^-)$ .

It is easy to see that  $\mathcal{C}_{1-}(f, g) = f \bullet g$  and  $\mathcal{C}_{0+}(f, g) = f \circ \check{g}$ .

Gray-scale  $\gamma$ -closing has the following properties.

**Proposition 5.4** (1)  $\mathcal{C}_\gamma(f, g) = -[\mathcal{C}_{1-\gamma}(-f, -g)]$ , i.e.,  $\mathcal{C}_\gamma(f, g)$  and  $\mathcal{C}_{1-\gamma}(f, \check{g})$  are dual operations.

(2)  $\mathcal{C}_\gamma$  are monotonically increasing, i.e., for  $f_1 \gg f_2$ , the following holds

$$\mathcal{C}_\gamma(f_1, g) \gg \mathcal{C}_\gamma(f_2, g). \quad (5.35)$$

(3)  $\mathcal{C}_\gamma$  is translation invariant, i.e.,

$$\mathcal{C}_\gamma(f_{(x_0, y_0)}, g) = [\mathcal{C}_\gamma(f, g)]_{(x_0, y_0)}. \quad (5.36)$$

$\gamma$ -closing also has the ability to remove spike noise from an image. For example, Figure 5.2(b) was processed by  $\gamma$ -closing, with the same  $3 \times 3$  SE. Because  $\mathcal{C}_\gamma$  and  $\mathcal{C}_{1-\gamma}$  are dual operators, we show the results in Figure 5.4 of  $\gamma = 0^+, 1/9, 3/9$  and  $4/9$  only. From the figures, one sees that when  $\gamma = 0^+$  or  $1/9$ , the p-directional noise was totally removed, with the n-directional noise left there. When  $\gamma = 3/9$  or  $4/9$ , both p- and n-directional noises were removed, leaving images having the same appearance as the original image Figure 5.2(a) (Note that the p-directional sources have lower intensities compared with the original image).

### The $\gamma$ -Sieving Process and Bi-directional SIEs

As we discussed before, the sieving process using opening extracts uni-directional size information when SEs were chosen properly. Replacing the opening in the sieving process by  $(1 - \gamma)$ -closing produces a parameterized sieving process. We call it the  $\gamma$ -sieving process. In the case of a digital signal and structuring element, however, when we increase the size of SE (thus the number of element in the SE) it is impossible to keep the same  $\gamma$  at each step (the only cases in which we can use the same  $\gamma$  are when  $\gamma = 0^+$  or  $1^-$ ). Thus, the parameter  $\gamma$  actually is a vector  $(\gamma_1, \gamma_2, \dots)$ . Let the  $\gamma$ -sieving ( $\gamma = (\gamma_1, \gamma_2, \dots)$ ) be denoted as  $\mathcal{S}_\gamma$  with SEs  $S_i$ ,  $i = 1, 2, \dots$ , then the growths of an image  $I$  by  $\mathcal{S}_\gamma$  are

$$G_{i+1,i} = \mathcal{C}_{1-\gamma_i}(I, S_i) - \mathcal{C}_{1-\gamma_{i+1}}(I, S_{i+1}). \quad (5.37)$$

When  $\gamma_i = 1^-$ , the growths are

$$G_{i+1,i} = I \circ \check{S}_i - I \circ \check{S}_{i+1}, \quad (5.38)$$

which is the sieving process in the ASB filtering process with SEs  $\{\check{S}_i\}$ . When all the components of the vector above have the same value, say  $\bar{\gamma}$ , then  $\gamma = \bar{\gamma}(1, 1, \dots)$ . In this case we simply write  $\mathcal{S}_\gamma = \mathcal{S}_{\bar{\gamma}}$ . In the case of  $S_{i+1} = S_i \oplus \check{B}_i$ ,  $\mathcal{S}_{1^-}$  produces p-directional growths  $G_{i+1,i}$ ,  $\mathcal{S}_{0^+}$  produces n-directional growths  $G_{i+1,i}$ . When  $\gamma$  is not  $0^+$  or  $1^-$ , however,  $\mathcal{S}_\gamma$  produces bi-directional growths.

The relative abilities of a bi-directional SIE to extract p- and n-directional SIs are judged by the polarities  $p^+ > 0$  and  $p^- > 0$ , with  $p^+ + p^- = 1$ . The polarities need to satisfy the following requirements. For any SIE,  $p^+ = 1$  is equivalent to purely p-directional;  $p^- = 1$  is equivalent to purely n-directional; and  $p^+ = p^- = 0.5$ ,

is equivalent to purely bi-directional (without polarity). Such polarities are also dependent on the input image  $I$ , thus for an SIE  $\mathcal{E}$ , the relative polarities with respect to image  $I$  could be defined by the following equations:

$$\begin{cases} p^+(\mathcal{E}, I) + p^-(\mathcal{E}, I) = 1, \\ p^+(\mathcal{E}, I)/p^-(\mathcal{E}, I) = \sqrt{\frac{\int[\mathcal{E}(I)+|\mathcal{E}(I)|]}{\int[-\mathcal{E}(-I)+|\mathcal{E}(-I)|]}}, \end{cases} \quad (5.39)$$

where the  $f$ s are the integrals over the whole definition domain of the corresponding functions.

In the  $\gamma$ -sieving process, the polarities at each step  $i$  are closely related to the corresponding  $\gamma_i$ . For a fixed-sloped peak (see Chapter 8 for this concept) and the SEs in  $\gamma$ -sieving process are cylindric, the polarities at step  $i$  are,  $p^+ = \gamma_i$ , and  $p^- = 1 - \gamma_i$ . When  $\gamma$  is approximately 0.5, one have  $p^+ = p^-$ , which implies from Equation (5.39) that

$$\mathcal{E}(I) = -\mathcal{E}(-I). \quad (5.40)$$

In the  $\gamma$ -sieving process, when  $\lim_{i \rightarrow \infty} \gamma_i = \bar{\gamma}$ , we see that

$$\sum_{i=1}^{\infty} G_{i+1,i} = I_o - C_{1-\bar{\gamma}}(I, S_{\infty}), \quad (5.41)$$

i.e., the summation only depends on  $\bar{\gamma}$ . We call it an asymptotic  $\bar{\gamma}$  sieving process, denoted as  $\bar{S}_{\bar{\gamma}}$ .

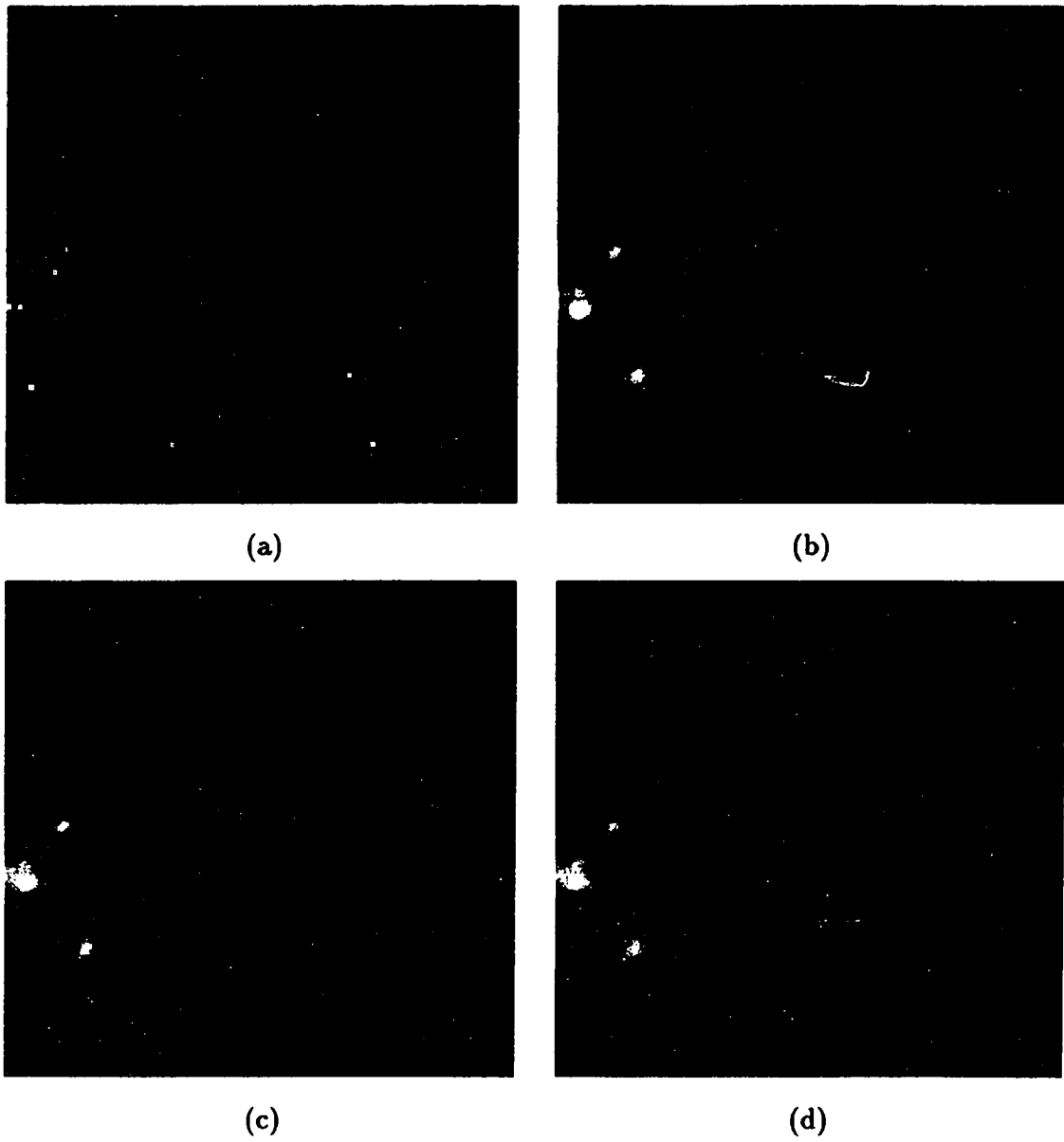


Figure 5.3: The  $\gamma$ -erosion of Figure 5.2(b) with a  $3 \times 3$  flat structuring element: (a)  $\gamma = 0^+$ ; (b)  $\gamma = 1/9$ ; (c)  $\gamma = 3/9$ ; and (d)  $\gamma = 4/9$

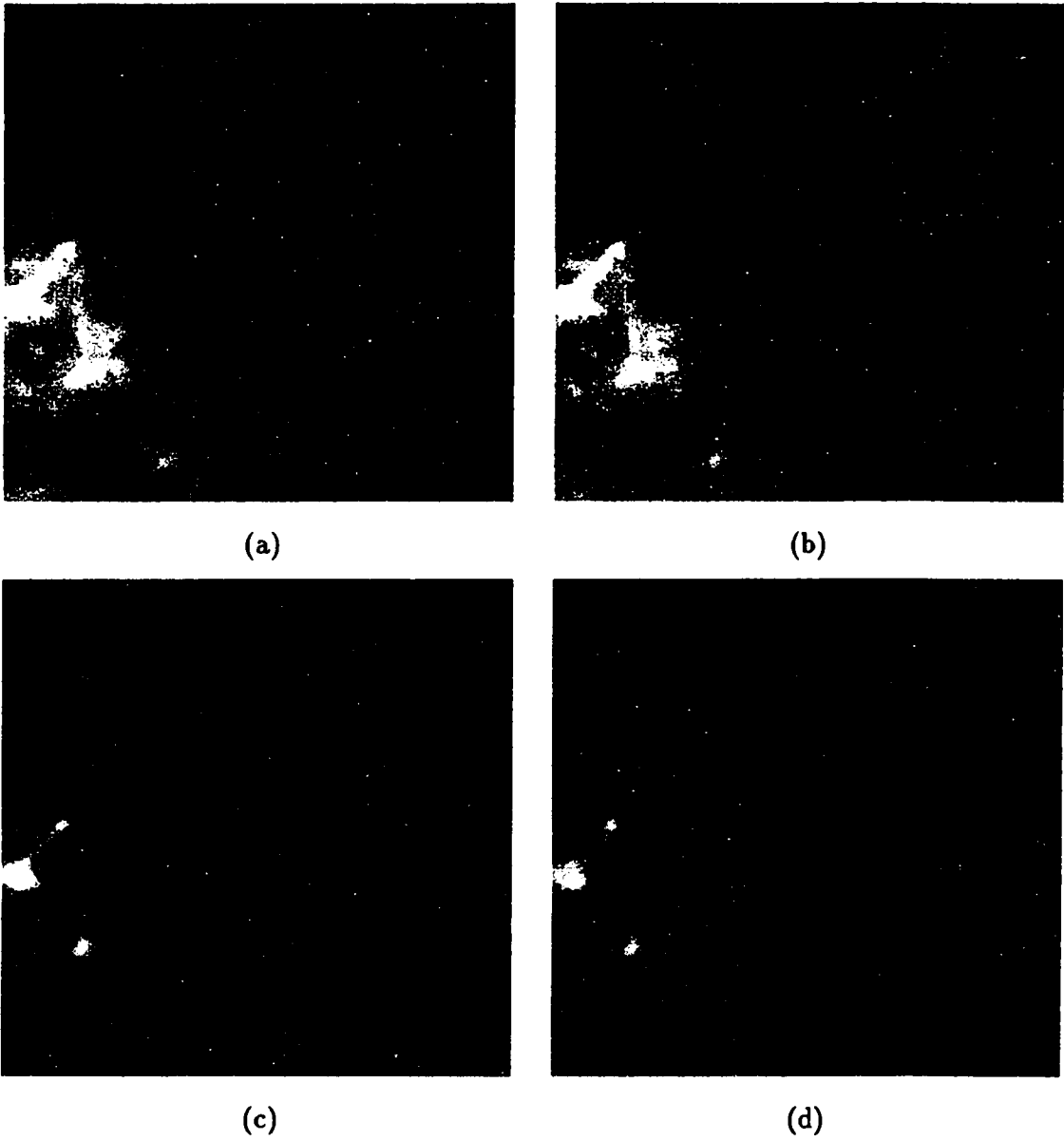


Figure 5.4: The  $\gamma$ -closing of Figure 5.2(b) with a  $3 \times 3$  flat structuring element: (a)  $\gamma = 0^+$ ; (b)  $\gamma = 1/9$ ; (c)  $\gamma = 3/9$ ; and (d)  $\gamma = 4/9$

## CHAPTER 6. WAVELET ANALYSIS

The name *wavelet* was first introduced in optics by Huygens where he used wavelets (or secondary waves) to form a wavefront [Jackson 1975]. The wavelets introduced were sinusoidal. Gabor [1946] tried to use wavelets localized in the time domain shifted from one basic wavelet to decompose a signal based on the Fourier transform. In the 1980's wavelets were used in geophysics to process seismology data [Cline 1984; Grossman and Morlet 1984; Goupillaud *et al.*, 1984/1985; Lazear 1984; Stone 1984; Thomas 1986; Newman 1986; Shtivelman 1988]. Among this work, Goupillaud, Grossman, and Morlet [1984/1985] tried to decompose signals using a basic wavelet by dilations and translations, which essentially was the foundation of the modern wavelet analysis. Further development of the modern wavelet theory and applications were first done by mathematicians (for instance, see [Daubechies 1988; Chui and Diamond 1990; Chui 1992a]), as well as engineers [Mallet 1989]. Since then, wavelet theory and applications have been developed rapidly. Hundreds of papers about wavelets were published in the last few years (for some of the literature, refer to Chui [1992a]; Chui [1992b]; Foufoula-Georgious and Kumar [1994]; Chui *et al.* eds. [1994]; Schumaker and Webb eds. [1994]).

The name *wavelet* today is different from the meaning before. It now narrowly refers to the decomposition of a signal by one basic wavelet (mother wavelet) with

dilation and translation. Although its meaning was narrowed down, wavelet analysis now forms a rigorous discipline having very rich contents. The complexity of the mathematics caused many people to refrain from learning its real physical meaning. When wavelet analysis was first introduced [Goupillaud *et al.* 1984/1985], the voice transform and the cycle-octave transform were introduced. These transforms were early versions of the wavelet transforms. The transforms introduced there have clear physical meanings that can be seen from the names. The physical meaning lies in the time and scale decomposition, which is used in the analysis of a signal at different resolution as desired. Such time-scale decomposition can be more easily be understood if combined with Fourier transform.

From the Fourier transform point of view, wavelet analysis uses multiple band filters (could be infinitely numbered) localized in the frequency and time domains in different scales. Different filter extracts different sized information of the signal. Therefore we may use wavelet method to extract the size information of the objects in IRAS data, and using them to separate cirrus from point or extended sources. The multiple band filtering with each band containing certain sized structures is also termed multi-resolution analysis since the resolution of the reconstructed signal can be controlled by combining appropriate filtering components. Looking back into the morphological sieving process, we find that it is a multi-resolution process. There, when the number of the growths ( $N$ ) increases, the sum  $\sum_{i=1}^{N-1} G_{i+1,i}$  may approach the original image  $I_o$  with any resolution desired.

In this chapter, introductory material about the wavelet transform (with emphasis on the continuous and semi-continuous wavelet transforms) is given. We try to obtain the filters which filter out different sized structures from an image using

wavelets and Fourier analysis. We start from a continuous wavelet, and discuss how to obtain the multiple filters I just mentioned. I also relate these filters with a discrete wavelet when the filters are obtained properly. Certain filters are combined to obtain scaling functions. The scaling functions represent the resolution lost.

This chapter is based on Fourier transform, therefore an understanding of Fourier transform is required in order to proceed.

$$f(x) = \sum_{a,b} \langle f, \psi_{b;a} \rangle \Psi^{b;a}(x) g(b, a), \quad (6.1)$$

where  $\psi(x)$  is called the mother wavelet, and  $\psi_{b;a}(x) = \frac{1}{\sqrt{|a|}} \psi\left(\frac{x-b}{a}\right)$  is the dilated and translated variant of  $\psi$  (parameters  $a$  and  $b$  are dilation and translation factors).  $\Psi^{b;a}$  is the dual function of  $\psi_{b;a}$ . The  $\sum$  can be integral or discrete sum.  $g(b, a)$  is the weight.  $\langle f, g \rangle$  denotes for the inner product. The dual of  $\psi_{b;a}$  is not unique. The only constrain for it is that for any function  $f$  Equation (6.1) holds. For simplicity, we always discuss the case that the dual of  $\psi_{b;a}$  is also a dilated and translated version of another wavelet  $\Psi$ . That is,  $\Psi^{b;a}(x) = \Psi_{b;a}(x) = \frac{1}{\sqrt{|a|}} \Psi\left(\frac{x-b}{a}\right)$ . Such cases, however, limit the choices of the mother wavelet  $\psi$ .

### Continuous Wavelet Transform

When both  $b$  and  $a$  are continuous, any function with the form of  $\Psi_{b;a} = \frac{1}{\sqrt{|a|}} \Psi\left(\frac{x-b}{a}\right)$  can be the dual function of  $\psi_{b;a}$ . In this case, we choose  $g(b, a) = g(a)$ , i.e.,  $g(b, a)$  is not related to  $b$  at all. Thus [Chui 1992a; Mallet 1989]

$$f(x) = \int_{-\infty}^{\infty} \int_0^{\infty} \langle f, \psi_{b;a} \rangle \Psi_{b;a} g(a) da db. \quad (6.2)$$

Taking the Fourier transform of the above equation, and noting that

$$\mathcal{F}[\psi_{b;a}(x)] = \frac{a}{\sqrt{|a|}} e^{-ib\omega} \hat{\psi}(a\omega), \quad (6.3)$$

where  $\hat{\psi}$  is the Fourier transform of  $\psi$ . Using the Parseval's identity, we get

$$\begin{aligned} \langle f, \psi_{b;a} \rangle &= \frac{1}{2\pi} \langle \hat{f}, \hat{\psi}_{b;a} \rangle, \\ &= \frac{a}{2\pi\sqrt{|a|}} \int_{-\infty}^{\infty} \hat{f}(\omega') e^{ib\omega'} \overline{\hat{\psi}(a\omega')} d\omega', \end{aligned} \quad (6.4)$$

where  $\overline{\hat{\psi}}$  is the complex conjugate of  $\hat{\psi}$ . Note that

$$\frac{1}{2\pi} \int_{-\infty}^{\infty} e^{ib(\omega' - \omega)} db = \delta(\omega' - \omega), \quad (6.5)$$

we obtain

$$\hat{f}(\omega) = \int_0^{\infty} \overline{\hat{\psi}(a\omega)} \hat{\Psi}(a\omega) |a| g(a) da \hat{f}(\omega). \quad (6.6)$$

where  $\hat{f}(\omega)$  is the Fourier transform of the function  $f(x)$ . This is an identity if

$$\int_0^{\infty} \overline{\hat{\psi}(a\omega)} \hat{\Psi}(a\omega) |a| g(a) da = 1. \quad (6.7)$$

Choosing  $g(a) = 1/(Ca^2)$  with

$$C = \int_0^{\infty} \overline{\hat{\psi}(t)} \hat{\Psi}(t) \frac{dt}{t}, \quad (6.8)$$

makes Equation (6.7) hold.

A special case is  $\Psi(x) = \psi(x)$ , thus

$$C = \int_0^{\infty} \frac{|\hat{\psi}(t)|^2}{t} dt. \quad (6.9)$$

Therefore, it is required that

$$\hat{\psi}(0) = 0, \quad (6.10)$$

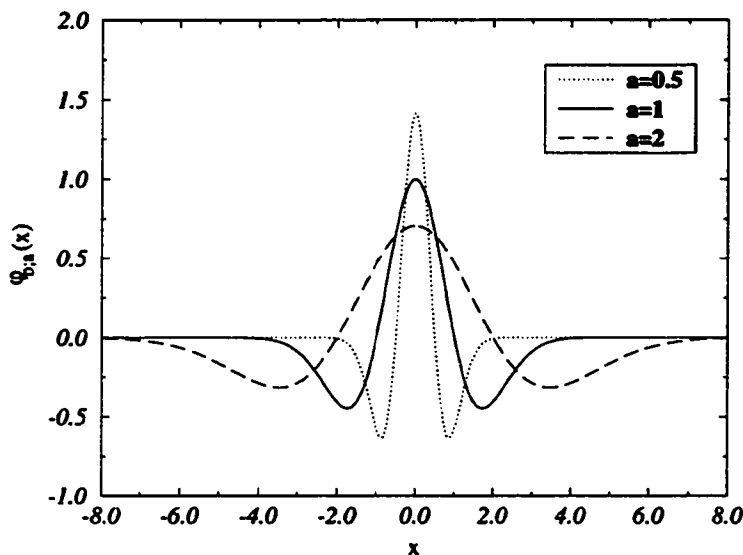


Figure 6.1: The dilated version of a function  $(1-x^2)e^{-x^2/2}$  with  $b = 0$ , and  $a = 0.5, 1$ , and 2

i.e.,

$$\int_{-\infty}^{\infty} \psi(x) dx = 0, \quad (6.11)$$

which is the *admissibility* condition of a wavelet. In wavelet analysis, the mother wavelet is chosen such that it is confined or localized in the time domain. Changing the parameter  $a$  in  $\psi_{;a}$  changes the confining region for the wavelet by scaling with a factor  $a$ . Thus, when  $a$  is small, the wavelet is more localized, when  $a$  is large, the wavelet is less localized. Figure 6.1 shows some of the dilated wavelets of the *Mexican-hat wavelet*  $(1-x^2)e^{-x^2/2}$ .

Wavelets are localized in the frequency domain too, which can be illustrated by the Mexican-hat wavelet again. Figure 6.2 shows the Fourier transform of  $\psi_{b;a}(x)$  with  $b = 0$ , and  $a = 0.5, 1$ , and 2. When  $a$  increases, the frequency response of the wavelet is more localized. It is easy to see that the localization of  $\psi_{;a}$  is proportional

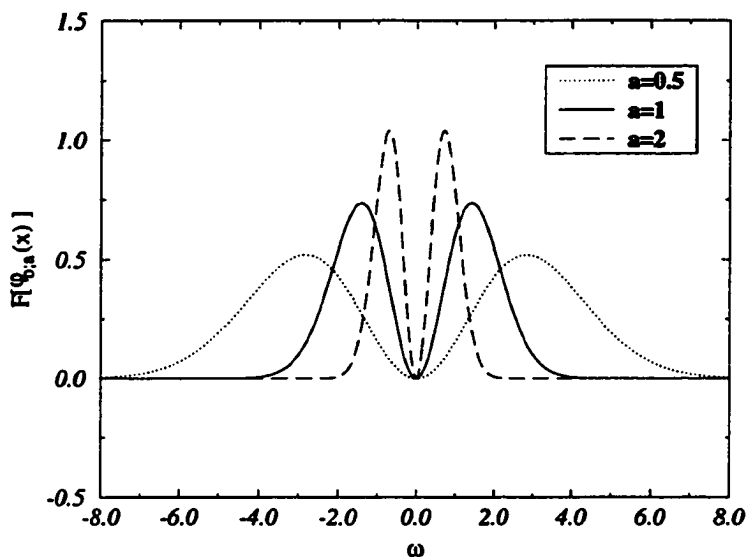


Figure 6.2: The Fourier transform of dilated version of function  $(1 - x^2)e^{-x^2/2}$  with  $b = 0$ , and  $a = 0.5, 1$ , and  $2$

to  $a$ , and the localization of  $\hat{\psi}_{b,a}$  is inversely proportional to  $a$ .

### Semi-continuous Wavelet Transform

As we have seen from the last section, any function  $\Psi$  can be the dual of the wavelet  $\psi$ . It implies an information redundancy which can be reduced by either relating  $a$  and  $b$  by certain functions, or limiting the available values for  $a$  and/or  $b$ . One common way to limit the available values for the parameters are discretization (or quantizing). Now, let's still take  $b$  as continuous, but  $a$  as discretized, again we choose  $g(b, a) = g(a)$ , then we have [Chui 1992a]

$$f(x) = \sum_a \int_{-\infty}^{\infty} db [(f, \psi_{b;a}) \Psi_{b;a}] g(a). \quad (6.12)$$

By a similar analysis as conducted in the last section, the above equation becomes,

$$\hat{f}(\omega) = \hat{f}(\omega) \sum_a \left[ |a| g(, a) \overline{\hat{\psi}(a\omega)} \hat{\Psi}(a\omega) \right]. \quad (6.13)$$

That is

$$\sum_a |a| g(, a) \overline{\hat{\psi}(a\omega)} \hat{\Psi}(a\omega) = 1. \quad (6.14)$$

This is the requirement for the dual wavelets  $\psi$  and  $\Psi$ .

The special case is the dyadic wavelet transform [Chui 1992a], in which  $a \in \{a_0 r^j, j \in \mathbb{Z}\}$ , and  $g(, a) = 1/|a|$ . For the dyadic wavelet transform, the dual wavelets need to satisfy

$$\sum_{j=-\infty}^{\infty} \overline{\hat{\psi}(a_0 r^j \omega)} \hat{\Psi}(a_0 r^j \omega) = 1, \quad (6.15)$$

### Discrete Wavelet Transform

The information redundancy can be further reduced when considering both  $a$  and  $b$  as discrete. In this case, the wavelet transform is stated as

$$f(x) = \sum_a \sum_b \langle f, \psi_{b;a} \rangle \Psi_{b;a} g(b, a). \quad (6.16)$$

Choosing  $g(b, a) = g(, a)$  and  $b = T_a \mathbb{Z}$ , where  $T_a$  is only related to  $a$ . Then

$$\hat{f}(\omega) = \sum_a \frac{1}{2\pi} \int_{-\infty}^{\infty} d\omega' \hat{f}(\omega') \overline{\hat{\psi}(a\omega')} \hat{\Psi}(a\omega) |a| \sum_{j=-\infty}^{\infty} e^{ijT_a(\omega' - \omega)} g(, a). \quad (6.17)$$

Note that [Oppenheim 1989] for

$$\sum_{j=-\infty}^{\infty} e^{ijT_a(\omega' - \omega)} = \sum_k \frac{2\pi}{|T_a|} \delta\left(\omega' - \omega - \frac{2\pi k}{T_a}\right), \quad (6.18)$$

we have

$$\hat{f}(\omega) = \sum_a \sum_k \overline{\hat{\psi}(a\omega + \frac{2\pi k a}{T_a})} \hat{\Psi}(a\omega) \hat{f}\left(\omega + \frac{2\pi k}{T_a}\right) g(, a) \frac{|a|}{|T_a|}. \quad (6.19)$$

Therefore the duals need to satisfy the following equation,

$$\sum_a \overline{\hat{\psi}(a\omega + \frac{2\pi ka}{T_a})} \hat{\Psi}(a\omega) g(, a) \frac{|a|}{|T_a|} = \delta_{k,0}, \quad (6.20)$$

where  $\delta_{k,0} = 1$  if  $k = 0$ , and  $\delta_{k,0} = 0$  if  $k \neq 0$ .

### Size Information Extraction by Continuous Wavelet

Multi-resolution analysis with the continuous wavelet transform depends on how we split the integral in equation (6.6). If we have a set of values  $\{a_i\}$  with  $i \in (-\infty, \infty)$ , and  $a_{i+1} > a_i$ ,  $a_{-\infty} = 0$  and  $a_{\infty} = \infty$ , then we may decompose the integral into

$$\hat{f}(\omega) = \frac{1}{C} \sum_{i=-\infty}^{\infty} \int_{a_i\omega}^{a_{i+1}\omega} \frac{|\hat{\psi}(t)|^2}{t} dt \hat{f}(\omega). \quad (6.21)$$

If we denote

$$H_i(\omega) = \frac{1}{C} \int_{a_i\omega}^{a_{i+1}\omega} \frac{|\hat{\psi}(t)|^2}{t} dt, \quad (6.22)$$

then

$$\hat{f}(\omega) = \sum_{-\infty}^{\infty} (H_i(\omega) \cdot \hat{f}(\omega)). \quad (6.23)$$

Thus, we can denote

$$f_i(x) = \mathcal{F}^{-1} (H_i(\omega) \hat{f}(\omega)) = \mathcal{E}_i(f(x)), \quad (6.24)$$

with  $\mathcal{E}_i$  denoting the size information extractor. We then have

$$f(x) = \sum_{i=-\infty}^{\infty} f_i(x) = \sum_{i=-\infty}^{\infty} \mathcal{E}_i(f(x)). \quad (6.25)$$

Let  $\Delta_\psi$  be the size of function  $\psi$ . Then the size of  $\psi_{;a}$  is  $a\Delta_\psi$ . Thus, each  $f_i(x)$  contains the size information between the  $\psi_{;a_i}$  (size of  $a_i\Delta_\psi$ ) and  $\psi_{;a_{i+1}}$  (size of

$a_{i+1}\Delta\psi$ ). The size information between  $\psi_{;a_i}$  (size of  $a_i\Delta\psi$ ) and  $\psi_{;a_j}$  (size of  $a_j\Delta\psi$ ) with  $j > i$  is denoted as,

$$G_{j,i} = \sum_{k=i}^{j-1} f_k. \quad (6.26)$$

This size information is very similar to the growth in the morphological sieving process, we will call it the growth as well. It is not difficult to find that the  $H_i$ 's are bi-directional and have  $p^+ = p^- = 0.5$ . That is, they are not polarized.

$H_i(\omega)$  has the following property,

$$\sum_{i=-\infty}^{\infty} H_i(\omega) = 1, \quad (6.27)$$

which gives

$$\sum_{i=-\infty}^{\infty} G_{i+1,i} = \mathcal{F}^{-1}(\hat{f}) = f. \quad (6.28)$$

If we denote  $\overline{\hat{h}_i(\omega)}\hat{h}^i(\omega) = H_i(\omega)$ , the decomposition can also be represented by  $h_i$  and  $h^i$ ,

$$f(x) = \int_{-\infty}^{\infty} db \left\{ \sum_{i=-\infty}^{\infty} \langle f(x'), h_i(x' - b) \rangle h^i(x) \right\}. \quad (6.29)$$

The function  $h^i$  is called the dual of  $h_i$ . This decomposition is not always a wavelet decomposition since no mother wavelet for all the terms exists.

We can make Equation (6.29) a wavelet decomposition under certain circumstances though. If we choose  $a_{i+1} = ra_i$ , where  $r$  is the root (a scalar), then  $a_i = r^i a_0$  (where  $r^i$  is the  $r$  with power of  $i$ ),

$$H_{i+1}(\omega) = H_i(r\omega). \quad (6.30)$$

Let  $\hat{h}_i(\omega) = \hat{h}^i(\omega)$ , then  $|\hat{h}_i(\omega)|^2 = H_i(\omega)$ ,  $|\hat{h}_{i+1}(\omega)|^2 = H_i(r\omega) = |\hat{h}_i(r\omega)|^2$ , thus  $|\hat{h}_i(\omega)|^2 = |\hat{h}_0(r^i\omega)|^2$ , where  $|\hat{h}_0(\omega)|^2 = H_0(\omega)$ , thus we have

$$\sum_{i=-\infty}^{\infty} |\hat{h}_0(r^i\omega)|^2 = 1. \quad (6.31)$$

That is,  $h_0(x) = \mathcal{F}^{-1}(\hat{h}(\omega))$  is a dyadic wavelet (see Equation (6.15) and replace  $a_0$  by 1). Thus, we can design a discrete wavelet from a continuous wavelet. The  $H_i$ 's are localized in frequency domain (see Figure 6.3), and their inverse Fourier transforms are localized in the time domain. Each  $H_i$  is localized at different frequency region, thus using  $H_i$ 's to filter a signal extracts the size information from this signal. That is,  $H_i$ 's form a multi-band filtering system, with each band extracting different localization information in the time domain.

### Scaling Functions

The signals in the real world can not have infinitely large size or infinitely small size. Thus the size information of extremely small and extremely large sizes are negligible, i.e.,  $\sum_{i=-\infty}^j G_{i+1,i}$  and  $\sum_{i=k+1}^{\infty} G_{i+1,i}$  are getting close to zero when  $j$  approaches negative infinity, and  $k$  approaches positive infinity. Such phenomena can be observed in terms of the scaling functions. Note in Equation (6.21), if we write

$$\overline{\hat{\phi}_j(\omega)} \hat{\phi}^j(\omega) = \frac{1}{C} \sum_{i=-\infty}^{j-1} \int_{a_i \omega}^{a_{i+1} \omega} \frac{|\hat{\psi}(t)|^2}{t} dt = \frac{1}{C} \int_0^{a_j \omega} \frac{|\hat{\psi}(t)|^2}{t} dt, \quad (6.32)$$

$$\overline{\hat{\Phi}_k(\omega)} \hat{\Phi}^k(\omega) = \frac{1}{C} \sum_{i=k+1}^{\infty} \int_{a_i \omega}^{a_{i+1} \omega} \frac{|\hat{\psi}(t)|^2}{t} dt = \frac{1}{C} \int_{a_{k+1} \omega}^{\infty} \frac{|\hat{\psi}(t)|^2}{t} dt, \quad (6.33)$$

where,  $\phi^j$  is the dual of  $\phi_j$ ,  $\Phi^k$  is the dual of  $\Phi_k$ , then from the above equations, Equation (6.21) and Equation (6.29), we have

$$\begin{aligned} f(x) &= \int_{-\infty}^{\infty} db \left\{ \sum_{i=j}^k \langle f(x'), h_i(x' - b) \rangle h^i(x - b) \right. \\ &\quad + \langle f(x'), \phi_j(x' - b) \rangle \phi^j(x - b) \\ &\quad \left. + \langle f(x'), \Phi_k(x' - b) \rangle \Phi^k(x - b) \right\}. \end{aligned} \quad (6.34)$$

The functions  $\phi_j$  and  $\Phi_k$  are small-size (high-resolution) and the large-size (low-resolution) scaling functions, respectively. It is not difficult to see that

$$\lim_{j \rightarrow -\infty} \overline{\hat{\phi}_j} \hat{\phi}_j = 0, \quad (6.35)$$

$$\lim_{k \rightarrow \infty} \overline{\hat{\Phi}_k} \hat{\Phi}_k = 0, \quad (6.36)$$

i.e., the information contained on both small- and large-sized sides are getting smaller and smaller when they approach the bounds. Thus, it is only necessary to conduct analysis for *limited* bands if error is allowed. By adjusting  $j$  and  $k$ ,  $\int_{-\infty}^{\infty} db \sum_{i=j}^k \langle f(x'), h_i(x' - b) \rangle h_i(x - b)$  can approach the original signal  $f$  with the resolution as high as desired.

Note that if  $h_i = h^i$ ,  $\phi_i = \phi^i$ , and  $\Phi_i = \Phi^i$ , then,  $|\hat{h}_i(\omega)|^2 = H_i(\omega)$ ,  $|\hat{\phi}_j(\omega)|^2 = \sum_{i=-\infty}^j H_i(\omega)$ , and  $|\hat{\Phi}_k(\omega)|^2 = \sum_{i=k+1}^{\infty} H_i(\omega)$ . Figure 6.3 shows  $|\hat{h}_i|^2$ ,  $|\hat{\phi}|^2$ , and  $|\hat{\Phi}|^2$ , with  $\psi(x) = (1 - x^2)e^{-x^2/2}$ , and  $a_i = 2^i$ .

Using the  $\phi_j$ ,  $\Phi_k$  and  $H_i$  with  $i=j+1, j+2, \dots, k$ , we conduct the multi-resolution analysis by adjusting  $j$  and  $k$ .

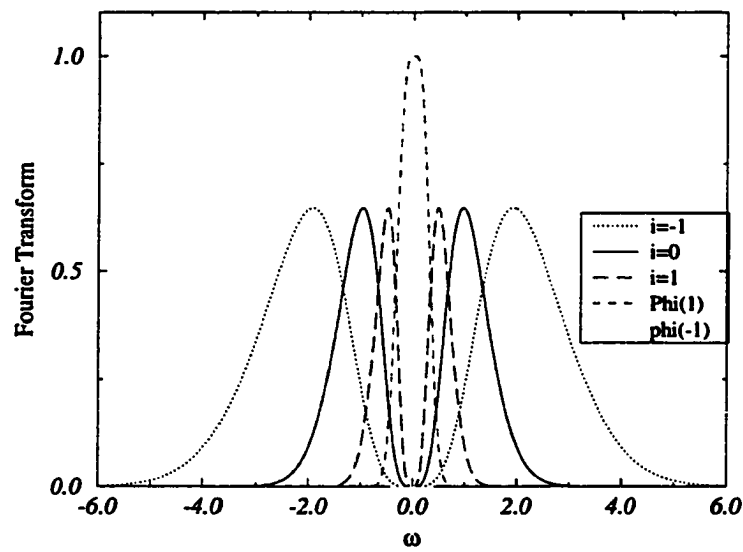


Figure 6.3: The illustrations of  $|\hat{\phi}_{-1}|^2$ ,  $|\hat{\Phi}_1|^2$ , and  $H_i$  with  $i = -1, 0$ , and  $1$

## CHAPTER 7. WAVELET SIZE INFORMATION EXTRACTORS

As we saw in the last chapter, the wavelet transform decomposes a function into combinations of the dilated and translated version of the mother wavelet. The mother wavelet is localized in both time and frequency domains. If we denote the localized size of the mother wavelet as  $\Delta_\psi$ , then the localization of  $\psi_{b;a}$  has a size of  $a\Delta_\psi$ . The size information from  $H_i$  then is between  $a_i\Delta_\psi$  and  $a_{i+1}\Delta_\psi$ , that from the scaling function  $\phi_j$  is between 0 and  $a_j\Delta_\psi$ , and that from the scaling function  $\Phi_k$  is between  $a_{k+1}\Delta_\psi$  and  $+\infty$ . Using  $H_i$  and the scaling functions, we are able to extract the size information for various sizes. This process is very much the same as the morphological sieving process, but with the growth  $G_{i+1,i} = \mathcal{F}^{-1}(H_i \hat{I}_o)$ , where  $I_o$  is the original image.

For the Mexican-hat wavelet, where  $\hat{\psi}(\omega) = \sqrt{2}\omega^2 e^{-\omega^2/2}$ , we have

$$H_i(\omega) = \frac{1}{C} \int_{a_i\omega}^{a_{i+1}\omega} \frac{|\hat{\psi}(t)|^2}{t} dt = (1 + a_i^2\omega^2)e^{-a_i^2\omega^2} - (1 + a_{i+1}^2\omega^2)e^{-a_{i+1}^2\omega^2}. \quad (7.1)$$

We may generalize the above  $H_i$  into

$$H_i(\omega) = (1 + a_i^m\omega^m)e^{-a_i^m\omega^m} - (1 + a_{i+1}^m\omega^m)e^{-a_{i+1}^m\omega^m}. \quad (7.2)$$

with  $m$  as an integer, since  $\sum_{i=-\infty}^{\infty} H_i = 1$  holds which can be seen from Equation (7.2).

We now use the extractors in Equation (7.2) to extract the size information from Figure 2.1, with  $m = 4$ ,  $a_0 = 0$ , and  $a_i = 1.189^i/2$  for  $i = 1, 2, 3, \dots$ . The

choice of  $a_0 = 0$  makes  $G_{i+1,i} = 0$  for  $i < 0$  since  $a_i = 0$  for  $i < 0$ , thus the growth layers here are indexed similarly to the sieving process. Figure 7.1 shows some size information extracted by  $H_i$ . Note that when  $i$  increases, the size information from larger structures are extracted.

From the  $a_i$  values given, and the definition of  $G_{i+1,i}$  in the beginning of this chapter, also use the definition of scaling functions in last chapter, we have

$$I_o = \sum_{j=0}^{M-1} G_{j+1,j} + \mathcal{F}^{-1}(|\hat{\Phi}_{M-1}|^2 \hat{I}_o), \quad (7.3)$$

where  $M$  is the number of dilation factors in use. Filtering of the original image can be similarly conducted by weighting images  $W_j$  (see Equation (2.2)).

$$I = \sum_{j=0}^{M-1} W_j \cdot G_{j+1,j} + W_M \mathcal{F}^{-1}(|\hat{\Phi}_{M-1}|^2 \hat{I}_o). \quad (7.4)$$

A simple weighting function was proposed in Equation (2.3). This step weight function was applied to the size information extracted by  $H_i$  with  $M = 16$ . Figure 7.2 shows the reconstructed images with different values of parameter  $K$  in Equation (2.3). Note that as  $K$  increases, more large-sized structures appear in the filtered image. When  $K = 12$ , the information in the filtered result is mainly from the point and extended sources. Also note the dark regions around the sources, which occur because of the admissibility of the wavelets. Thus,  $\int G_{j+1,j} dx dy = 0$ . That is, the average of the filtering result is zero.

### Cirrus Characterization and Removal

Because of the similarities between the process of size information extraction by wavelet methods and the sieving process mentioned in Chapters 2, 3, and 4, we

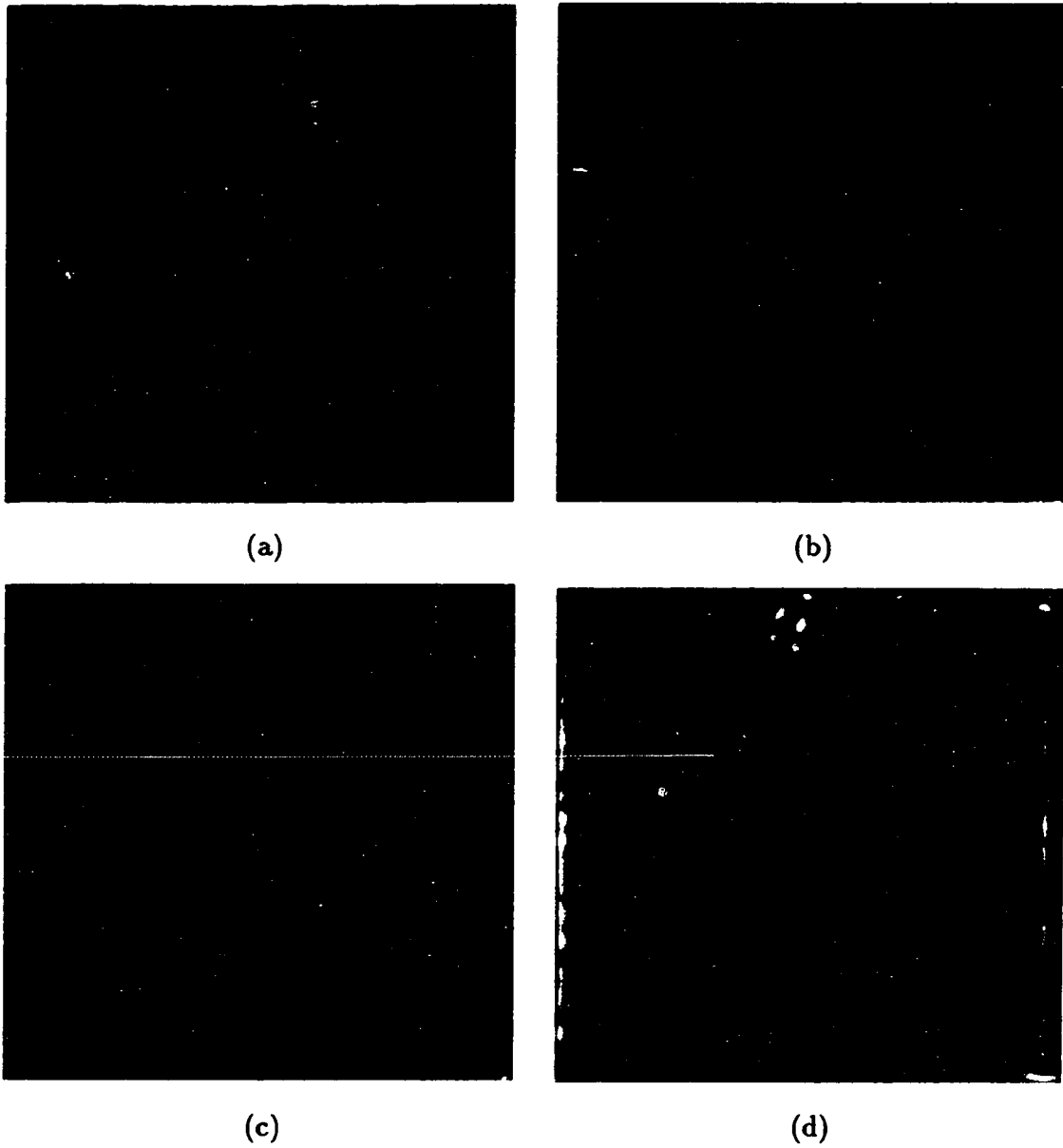


Figure 7.1: Several size information maps of the image in Figure 2.1 using the wavelet transform: (a) between  $i = 2$  and  $3$ ; (b) between  $i = 6$  and  $7$ ; (c) between  $i = 10$  and  $11$ ; and (d) between  $i = 15$  and  $16$

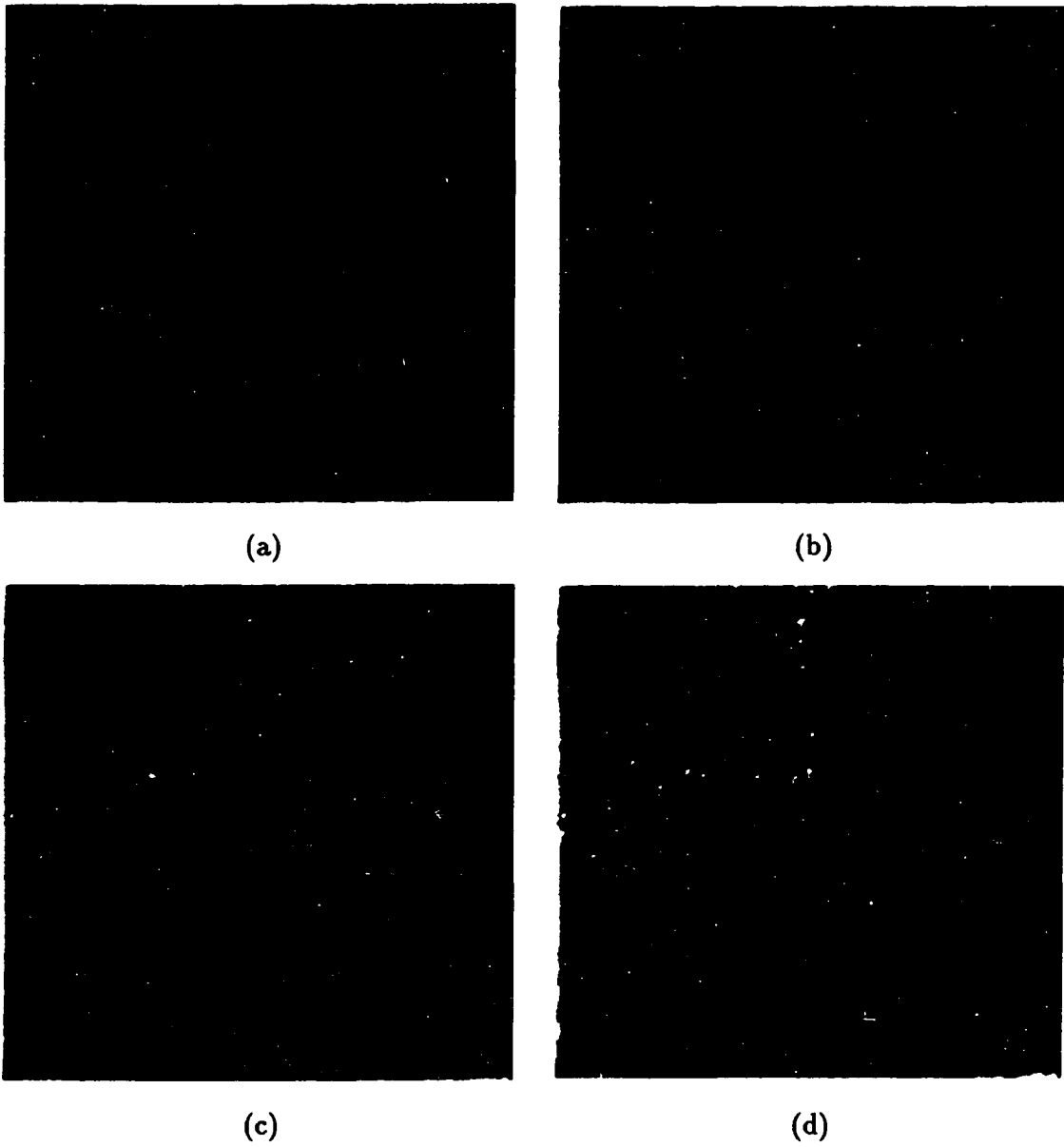


Figure 7.2: Reconstructed images using step function with: (a)  $K = 4$ ; (b)  $K = 8$ ; (c)  $K = 12$ ; and (d)  $K = 16$

use the same analysis strategy for the filtering process as before in Chapters 2 and 3. To refresh your memory, I will state the filtering process in sieving briefly. In the sieving process, the growths  $G_{i+1,i}$ ,  $i = 1, 2, \dots$ , were calculated by opening and stacked together to form a growth cube. The growths in the cube for each pixel of an image were then mapped into a feature space for classification using the k-means method. The growths of different classes after classification, together with the class maps, were used to determine the significant cirrus class, which were further used to remove cirrus components from each pixel. The final filtering consisted of determining a characteristic interval (CI) which indicated the growth layers where the growths for point sources were negligible, but were significant for Galactic cirrus. Using the growth information in the CI, we used the equal CI area method, non-overlapping method, or multi-cirrus filtering to remove the corresponding cirrus components from each pixel.

The cirrus characterization and removal process for size information extracted by wavelet SIEs were conducted similarly with only minor differences. The growths in consideration were calculated by the method stated in the last section with a total of 16 growth layers.

The k-means method was again employed to classify the growths. Since the extractors  $H_i$ 's are bi-directional (with  $p^+ = p^- = 0.5$ ) extractors, they extract both p- and n-directional size information without discrimination. If we have two peaks such that  $f_1(x) = -f_2(x)$ , then the size information of  $f_1$  will be the same as that of  $f_2$  except a negation is imposed. We want to treat size information in feature space and its reflection as the same. Thus, peaks in the p- and n- directions are to be extracted at the same time. Such data modification does not conflict with

cirrus characterization, and yet saves time in classification because fewer classes are required to distinguish cirrus from point and extended sources than when data were not modified. From our experiments, five classes are sufficient in the k-means method to distinguish the cirrus from point sources when data are modified in the way above. Figure 7.3 shows the areas of different classes after classification (i.e., class maps), and Figure 7.4 contains the growth profiles of the classes. As can be seen from Figure 7.3 and 7.4, Class 1 has large growths at small sizes, it corresponds to the point sources. Class 2 has strong growths at middle and higher growth layers, it corresponds to the extended sources. Class 4 corresponds to strong cirrus which surrounds the point and extended sources. Class 5 is the weakest cirrus which contains the information mainly from large structures. Class 3 is the area between Class 4 and Class 5, which is medium sized cirrus. Comparison of the growths of classes in the wavelet SIEs (Figure 7.4) and sieving SIEs (Figure 3.4), one finds that the sieving process produces cirrus growths which are more similar to each other (similar normalized growths), but the growths of cirrus in wavelet extraction have quite different normalized growths.

Remember the filtering process discussed in Chapter 3 is based on the linearities of the extractors. The equal CI area method with one cirrus class is based on the similarities between the cirrus classes. The non-overlapping method is based on uni-directional growths. The wavelet SIEs are linear, but they produce multiple cirrus growths which are quite different one from another. Also, they are not uni-directional. Thus, in the methods discussed in Chapter 3, only multi-cirrus filtering is suitable for the wavelet SIEs. To accomplish the multi-cirrus filtering, we first take Class 4 (strong cirrus) as the significant cirrus to filter pixels of Classes 1, 2, and 4 using the equal CI area method with  $CI = [14, 15, 16]$ . The reason for choosing this CI

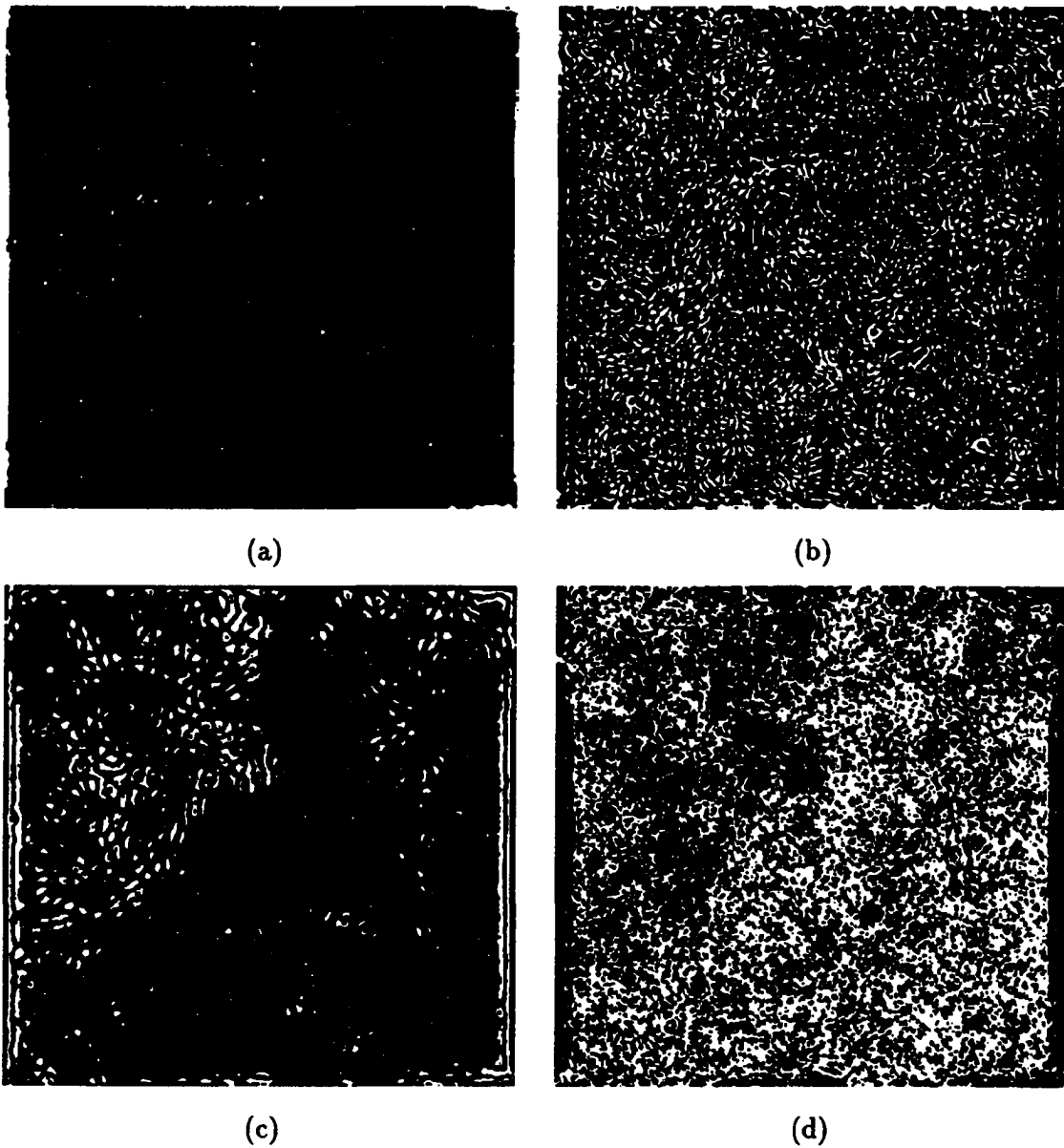


Figure 7.3: The areas for different classes using wavelet: (a) Class 1 and 2 shown as white area; (b) Class 3 shown as white; (c) Class 4 shown as white; (d) Class 5 shown as white

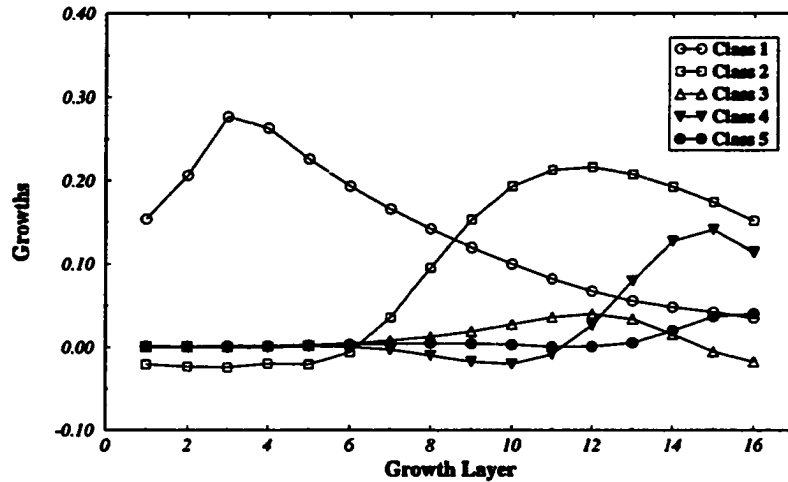


Figure 7.4: The growths for five classes using the wavelet transform

is that in this interval, the growths of Class 1 are smallest, yet the growths of Class 4 are very strong (see Figure 7.4). Pixels belonging to Class 3 are filtered using the growths of Class 3 and the equal CI area method with  $CI = [9, \dots, 14]$  (because the growths for Class 3 are strongest there). Pixels belonging to Class 5 are filtered using the growths of Class 5 with the equal CI area method with  $CI = [13, \dots, 16]$  (the growths for this class are significant there). Figure 7.5 shows the filtered result. Note that except at regions near the boundary, the filtering shows high quality with the cirrus reduced by a factor of 15. Due to the admissibility of the wavelet, which introduces dark regions around bright sources, the filtered image still contains some dark regions around the point sources. Such effects are difficult to avoid when the SIEs are bi-directional (especially when no polarity exists), and the filtering is linear.

The fluxes of the sources are not reliable as demonstrated from experiments. Figures 3.5(a) and (b) were filtered with the wavelet method. The results show that the point sources have fluxes of  $51.6 \pm 2.3 \text{ MJy sr}^{-1}$  (18% lower than the real flux),

and have FWHMs of  $2.85 \pm 0.09$  pixels (total deviation from true FWHM of 3.8%). The extended sources have fluxes of  $103.2 \pm 5.0$  MJy sr<sup>-1</sup> (37% lower than the real flux) and FWHMs of  $4.49 \pm 0.07$  pixels (10% deviation from true FWHM). Such losses of fluxes are due to the complicated mixing of the size information at high growth layers from both point or extended sources and the cirrus foreground. It is difficult to split them by simply using the equal CI area method, since the large growths for sources at higher layers. There are other ways to improve the fluxes of the sources, though, such as the predictive wavelet as will be mentioned soon.

A list of the fluxes and FWHMs for these point and slightly extended sources can be found in Appendix B, Table B.7.

### Other Extraction Methods Using Wavelets

Examining Figure 7.4 we see that the growth of Class 2 is very large at high layers. This means the extractors did not extract the size information efficiently enough. By recombining the size information, we are able to form new growths which are more efficient (i.e., the growth for point and extended sources have smaller growths at high layers). We present two methods of recombining the growths, one is called iterative wavelet, another is called predictive wavelet method. The iterative wavelet method is quite like the sequential sieving process discussed in Chapter 4, but in here, the image “free” of small size information at each step is processed (sieved) by the “new” as well as the “old” sieves, such that the small size information escaping from previous sieving can be capture again. The predictive wavelet method tries to predict the size information larger than the SIE at each step, and take the lost size information into consideration (by adding them into the SI of the last step). For point



Figure 7.5: The filtered image of Figure 2.1 using multi-cirrus filtering with the wavelet method

sources, it is possible to accelerate the extraction of SI with these recombinations of growths.

### Iterative wavelet

As stated before, iterative wavelet method is a sequential process, in which, at each step, the SI are updated. Just like in the sequential sieving process, at step  $i$  there exists an image  $I_i$  to be used for SI extraction. The  $I_i$  is free of size information smaller than  $a_i\Delta_\psi$ . The  $I_i$ 's are related to each other by the following equation,

$$I_{i+1} = I_i - \sum_{j=-\infty}^i \mathcal{F}^{-1}(H_j \hat{I}_i), \quad (7.5)$$

where  $H_i$  are extractors of normal wavelet method as discussed before. The above equation means that  $I_{i+1}$  is obtained from  $I_i$  by stripping size information smaller than  $H_i$ . At step  $i$ , only layers  $j \leq i$  have growths. The growths are updated by including the size information extracted from  $I_i$ . Thus, the growth of layer  $j$  at step  $i$  is

$$G_{j+1,j} = \mathcal{F}^{-1}(H_i \sum_{k=j}^i \hat{I}_k). \quad (7.6)$$

The growth obtained this way, with the same  $H_i$  and  $a_i$  as we used in last sections, is classified in the same way using the k-means method. Figure 7.6 shows the growths of the different classes from the SI of Figure 2.1 by iterative wavelet. Again, Class 1 corresponds to point sources, Class 2 corresponds to extended sources, Class 5 is the regions around Class 1 and 2 (i.e., it is strong cirrus), Class 4 is the weakest cirrus, and Class 3 is the medium cirrus. Note the growths of the extended sources (Class 2) are smaller at higher layers now compared to Figure 7.4. The growth of Class 1 is more concentrated at low layers which is a evidence that the iterative wavelet has higher extraction efficiency than the normal wavelet method has. Using multi-cirrus

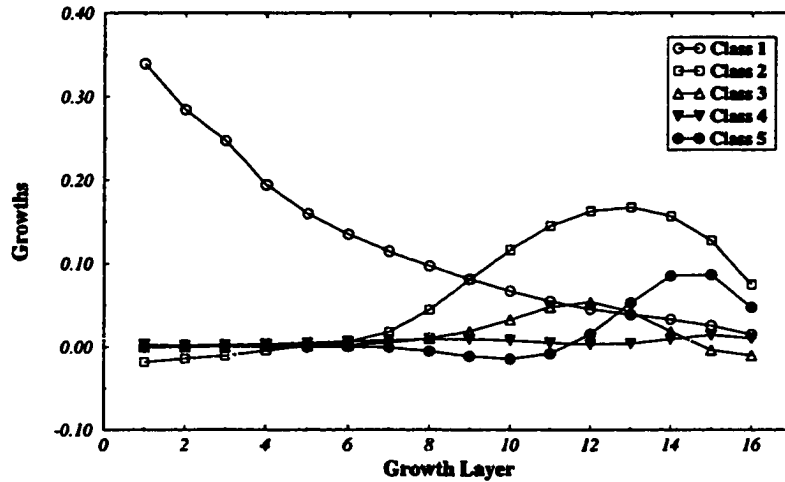


Figure 7.6: The growths for five classes using iterative wavelet

filtering, the image Figure 2.1 was filtered using the SIs by iterative wavelet SIEs. The result is shown in Figure 7.7. The cirrus is reduced by a factor of 15 in comparison with the original image. But the areas with negative values are increased by a factor of 3 when compared with the normal wavelet method. The fluxes from the filtered images of Figure 3.5(a) and (b) show that this method retain more fluxes than the method mentioned in last section. The point sources have fluxes of  $52.3 \pm 4.3 \text{ MJy sr}^{-1}$  (17% lower than the real flux), and the extended sources have fluxes of  $110.7 \pm 5.4 \text{ MJy sr}^{-1}$  (34% lower than the real flux). The FWHMs for the point sources are  $2.87 \pm 0.07$  pixels (3.6% deviation from the true FWHM), and those for the extended sources are  $4.52 \pm 0.09$  pixels (9.8% deviation from the true FWHM of the extended source). The reason for the losses is the same as discussed in the last section.

A list of the fluxes and FWHMs for these point and slightly extended sources can be found in Appendix B, Table B.8.



**Figure 7.7:** The filtered image of Figure 2.1 using multi-cirrus filtering with iterative wavelet method

### Predictive wavelet

The predictive wavelet method tries to predict the lost size information for a certain size at a growth layer, and put this lost size information into the growth. Suppose we have a signal which is a  $\delta$ -function, i.e.,  $f(x) = \delta(x)$ . Then the coefficients  $\langle \delta(x), \psi_{0;a} \rangle = \frac{1}{\sqrt{|a|}}\psi(0)$ , i.e.,  $\langle \delta(x), \psi_{0;a} \rangle \psi_{0;a}$  is proportional to  $\frac{1}{|a|}$ . With the feature extractors  $H_i$ , if we choose  $a_i = a_0 r^i$  (where  $r$  is a root), we may predict the remaining intensity for the  $\delta$ -function as

$$L_i = G_{i+1,i} \cdot \sum_{j=1}^{\infty} r^{-j} = G_{i+1,i} \cdot \frac{1}{r-1}. \quad (7.7)$$

Let  $R = 1/(r-1)$ , then the new growth at layer  $i$  is

$$G'_{i+1,i} = (1+R)G_{i+1,i} - RG_{i,i-1}. \quad (7.8)$$

In two dimensional case, the  $R$  is related to  $r$  differently by,

$$R = \frac{1}{r^2-1}. \quad (7.9)$$

For  $a_i = 1.189^i/2$ , we have  $R = 2.414$ . Using Equation (7.8), we calculated the new growths. They are then classified using the same classification mechanism discussed in last section. Figure 7.8 shows the growths of different classes, from the SI of Figure 2.1. Again, Class 1 is point sources, Class 2 is extended sources, Class 3 is the regions around Class 1 and 2 (i.e., it is strong cirrus), Class 4 is the weakest cirrus, and Class 5 is the medium cirrus. Note the growth of the extended sources (Class 2) is smaller at higher layers now compared to Figure 7.4, but is much larger than Figure 7.6. The growth of Class 1 is more concentrated at low layers compared with the normal wavelet method. The double maxima in the growth of Class 1 might

be an evidence that it can distinguish peaks with sizes close to each other. Using multi-cirrus filtering, the image Figure 2.1 was filtered using the SIs by predictive wavelet SIEs. Figure 7.9 shows the filtered image. The fluxes of sources by this method are retained even better than with the normal wavelet method, and iterative wavelet. From the filtered images of Figure 3.5(a) and (b), we found that the 16 point sources have fluxes of  $53.7 \pm 5.0$  MJy sr<sup>-1</sup>, (16% lower than the real flux), and the fluxes for the 16 extended sources are  $133.0 \pm 9.3$  MJy sr<sup>-1</sup> (20% lower than the real flux). The FWHMs for the point sources are  $2.88 \pm 0.08$  pixels (3.6% deviation from the true FWHM), and those for the extended sources are  $4.75 \pm 0.09$  pixels (5.4% deviation from the true FWHM of the extended source). Its better performance can be observed from the growths of the classes, because point sources and extended sources have more concentrated growths at lower layers. The cirrus is reduced by a factor of 13. The areas containing negative values are similar to that of the normal wavelet method but 2/3 smaller than that of iterative wavelet method.

A list of the fluxes and FWHMs for these point and slightly extended sources can be found in Appendix B, Table B.9.

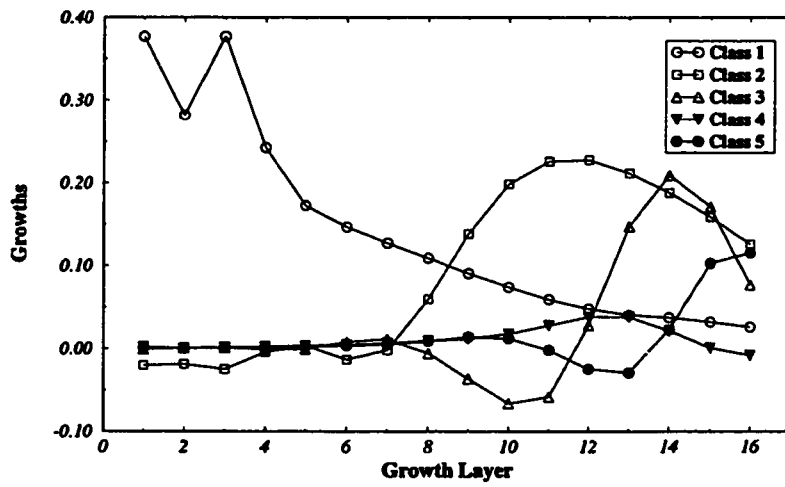


Figure 7.8: The growths for five classes using predictive wavelet

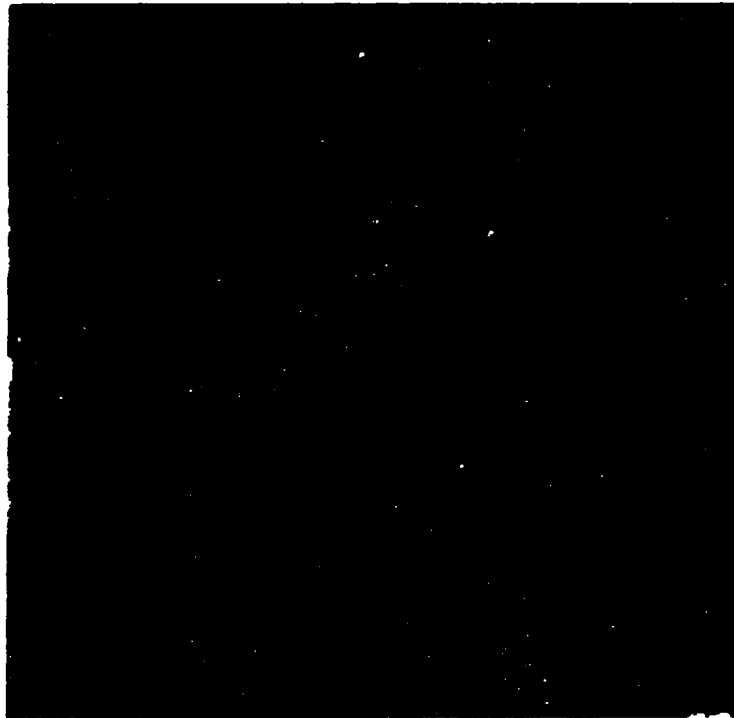


Figure 7.9: The filtered image of Figure 2.1 using multi-cirrus filtering with predictive wavelet method

## **CHAPTER 8. JUSTIFYING SIZE INFORMATION EXTRACTORS**

In previous chapters, we have seen size information extractors (SIEs) in sieving processes and wavelet multi-resolution analysis. We also saw that the size information (or growths) extracted by different SIEs were quite different. Using reasonable linear filtering (such as the equal CI area method, non-overlapping method, and multi-cirrus filtering method), the growths were recombined to obtain the information mainly on point sources and extended sources. The cirrus intensity in the original image is reduced by a factor of more than 13, which could be up to 30. Such filtering process have proven to be quite successful in both object identification and flux retention. The success of the linear filtering lies first on the growths which are capable of distinguishing the cirrus from point and extended sources, secondly on the accurate or approximate linearities of the SIEs which makes the flux retention possible.

In this chapter, I attempt to discuss the abilities of the SIEs to tell sharp peaks and smooth structures apart by extracting the SI from a prototype peak and analyzing it in the SIE size domain and spatial domain. The linearity of the wavelet SIE is obvious, no further need to discuss this more. The linearity of a morphological SIE does not hold most of the time, thus more discussion is needed.

### Linearity of Size Information Extractor

In order to justify a SIE quantitatively, we need first to define size information. This certainly is not unique. One way to get around this problem is by using one standard set of SIEs to define the standard size information (SI). Other SIEs would be compared to the standard SIs for reference. For instance, the SIEs of morphological sieving with the cylindric SEs have a very simple meaning of size information extraction. Examine Figure 8.1, where a peak with the form  $f(x) = -k|x|$ , with  $k = 10/7$  is shown. The reasons for choosing this prototype peak are that it has fixed slope and it is simple to analyze in the sieving process. Changing the slope  $k$ , the function  $f(x)$  simulates various parts of the Gaussian shaped peak, or some real peaks. To use this prototype peak to analyze real peaks, however, requires more work because various slopes needs to be considered. For a sieving process, an SE with width  $w$  produces an accumulative SI at position  $x$  from peak  $f(x)$  ( $\sum_{i=0}^n G_{i+1,i}$ , where the  $(n+1)$ th SE has width of  $w$ ), denoted as  $s(x, w, f)$ . For cylindric SEs and the function  $f(x)$  in Figure 8.1, we have the accumulative size information of

$$s(x, w, f) = \begin{cases} 0, & |x| \geq w/2, \\ kw/2 - k|x|, & |x| < w/2. \end{cases} \quad (8.1)$$

The differential SI (for short, DSI) is defined as

$$s_d(x, w, f) = \frac{\partial s(x, w, f)}{\partial w}. \quad (8.2)$$

For the case of cylindric SEs, the sieving process has

$$s_d(x, w, f) = \begin{cases} 0 & w \leq 2|x|, \\ k/2 & w > 2|x|. \end{cases} \quad (8.3)$$

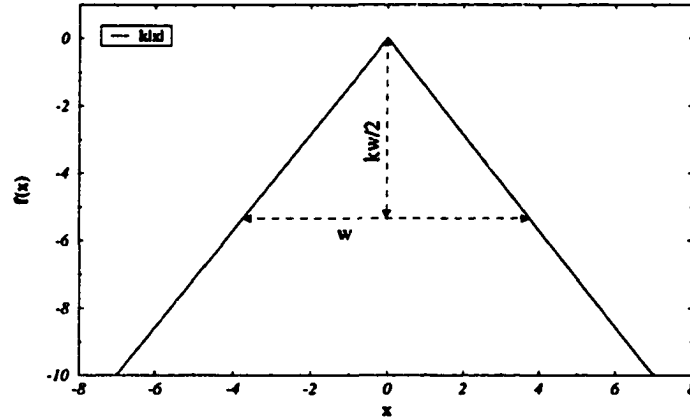


Figure 8.1: A prototype peak  $f(x) = -k|x|$

If we have two peaks  $f_1(x) = -k_1|x|$  and  $f_2(x) = -k_2|x|$ , with  $k_1, k_2 > 0$ , then for the cylindric sieving, if  $k_3, k_4 > 0$ , we have

$$s(x, w, k_3 f_1 + k_4 f_2) = k_3 \cdot s(x, w, f_1) + k_4 \cdot s(x, w, f_2), \quad (8.4)$$

i.e.,  $s(x, w, \cdot)$  is a linear operator. It is not difficult to verify that  $s_d(x, w, \cdot)$  is linear too. It should be kept in mind though, that this linearity is not valid for all types of peaks. For instance, if  $f_1(x) = -k_1|x|$ , but  $f_2(x) = -k_2|x - x_0|$ , with  $x_0 \neq 0$ , the linearity stated above does not hold. For most of the cases, however, an approximate linearity of the cylindric sieving can be assumed.

When comparing the SIs from two SIEs, it only makes sense when the sizes of the SIEs are equal or similar. The sizes of the SIEs can be defined by the size of the SE, in the sieving process, or the size of the wavelet with the dilation factor  $a$ , in the wavelet methods (i.e.,  $a\Delta_\psi$ ). We denote the size of a SIE  $\mathcal{E}$  by  $S(\mathcal{E})$ .

Figure 8.2 shows the accumulative size information by different extractors from  $f(x)$  at  $x = 0$ . The horizontal axis is for  $w$ , the size. Cylind means cylindric struc-

turing elements, Gauss 1 means Gaussian shaped structuring elements with height 1, Gauss 10 means height 10, and Hemisphere uses hemispheric structuring elements. Wave-norm is normal wavelet method, Wave-iter is wavelet iterative, and Wave-pred is the predictive wavelet method. We see that for the morphological methods with cylindric and hemispheric structuring elements, the size information is linearly dependent on the size of the structuring elements. Gaussian shaped structuring elements extract the size information linearly only when the structuring elements are big enough or the height of the peak is small enough. The speed of the extraction is reflected from the differential size information. Figure 8.3 shows the differential size information for different extractors. The horizontal axis is for  $w$ , the size. Morphological methods with cylindric and hemispheric structuring elements have constant differential size information, the Gaussian shaped structuring elements with height 1 and 10 have constant DSI after  $w = 5$  and 13, respectively. The constant DSIs for cylindric and Gaussian shaped structuring elements are the same (which is  $k/2$ ), and the constant DSI for hemispheric structuring elements is smaller (around  $k/4$ ). Normal wavelet, iterative wavelet and predictive wavelet methods yield very similar results. They all yield large DSIs when  $w < 1$ , then decrease as  $w$  increases.

For a morphological sieving SIE  $\mathcal{E}$ , with an  $SE=S$ , for any constant  $a > 0$ , for any  $f$ , we have

$$a\mathcal{E}(f) = \mathcal{E}^a(af), \quad (8.5)$$

where  $\mathcal{E}^a$  is a sieving SIE with an  $SE=kS$  (i.e., an SE by scaling  $S$  in the vertical direction by a factor of  $a$ ). If  $\mathcal{E}^a$  is linear, then  $\mathcal{E}^a(af) = a\mathcal{E}^a(f)$ , then we have

$$\mathcal{E}^a(f) = \mathcal{E}(f). \quad (8.6)$$

For instance, if  $\mathcal{E}$  is chosen from Gauss 1, then  $\mathcal{E}^{10}$  is found in Gauss 10 with the

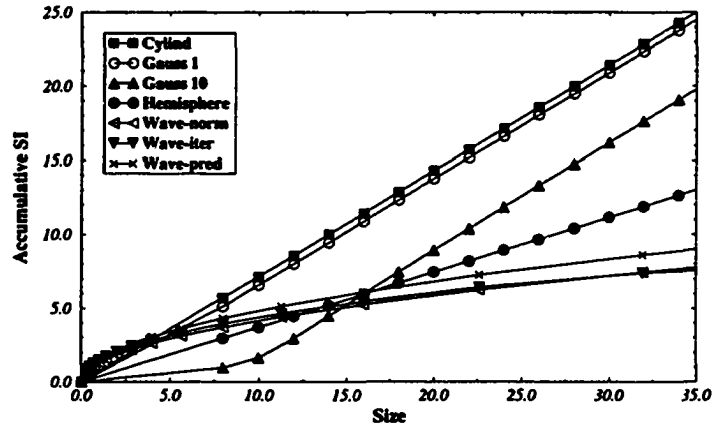


Figure 8.2: Accumulative size information by various extractors at  $x = 0$

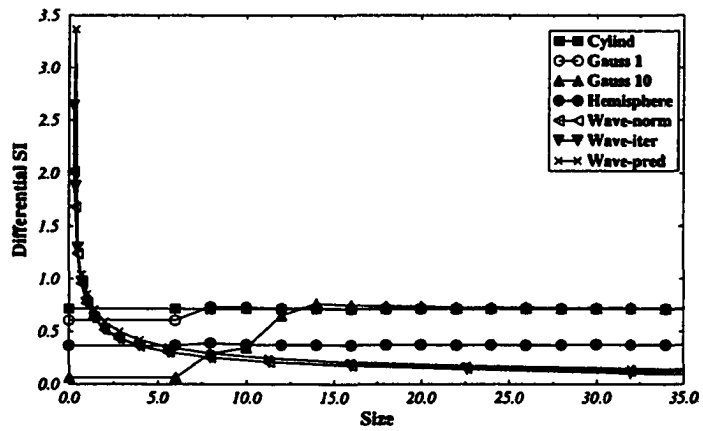


Figure 8.3: Differential size information by various extractors at  $x = 0$

same SE size. The cylindric sieving with the same SE size is  $\mathcal{E}^0$ . Gauss 1 sieving has almost the same SI as that from the cylindric SIEs at  $w > 5$ . Gauss 10 sieving has almost the same SI as that from the cylindric sieving, but with  $w > 13$ . We also know that cylindric SIEs are almost linear, then we conclude that Gauss 1 and Gauss 10 are almost linear too at  $w > 5$  and  $w > 13$ , respectively, when  $k > 10/7$ .

The linearity of hemispheric sieving can be found similarly. Let  $\mathcal{E}$  be the SIE by hemispheric SE, then SIE by cylindric SE with the same size is  $\mathcal{E}^0$ . Because the SI extracted by hemispheric SIE is half of that by cylindric SIE, we conclude that hemispheric SIEs are all non-linear. If the the slope of the peak  $k$  increases, the SI by the hemispheric sieving is getting closer to that by the cylindric sieving. Thus, the hemespheric sieving approaches to a linear operator as  $k$  increases to infinity.

We have been discussing the linearity of the extractors for size information at  $x = 0$ . When  $x \neq 0$ , the linearity existing at  $x = 0$  may vanish. For instance, we plot differential SIs at  $x = 10$  in Figure 8.4 from different SIEs with the horizontal axis as  $w$ , the size. The linearity of the cylindric sieving is still there. The linearity of Gauss 1 sieving can still be approximated because its size information extracted are almost the same as those of the cylindric sieving. Gauss 10, however, is non-linear up to  $w = 35$  or higher layers.

### Spatial Discrimination of SIE

An SIE extracts SI from the peak  $f(x)$  differently at different  $x$ . This is why we use the SIEs to tell peaks and smooth structures apart. Such spatially discriminating capability for SIEs will be discussed quantitatively.

Figure 8.5 and 8.6 show the accumulative and differential SIs extracted by the

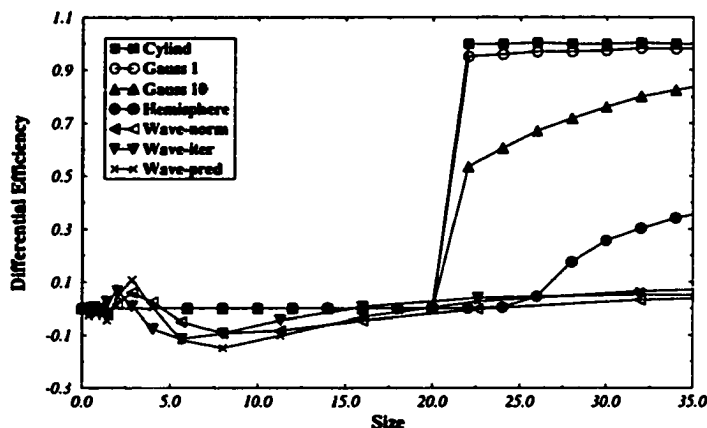


Figure 8.4: Differential size information by various extractors at  $x = 10$

SIEs of different methods (sieving processes and wavelet method) where the horizontal axis has units of the size of the SIE. The size of the SIE in sieving process is the size of the SE in use, the size of the SIE in wavelet method is the dilation factor  $a_i$ , which is related to  $H_i$ . We denote the size of an SIE  $\mathcal{E}$  as  $S(\mathcal{E})$ . In Figure 8.5, the cylindric SE sieving process produces the best accumulative SI spatial discrimination since its accumulative SI at  $x = 0$  is larger than that of other SIEs, yet at position  $x > 0.5S(\mathcal{E})$  is similar to that of other SIEs (with values close to zero). Gauss 1 SIEs perform similarly to cylindric SIEs. Gauss 10 SIEs have weaker spatial discrimination ability viewed from the accumulative SIs. The ability of the hemispheric SIEs are even weaker. The wavelet SIEs perform similarly, and their discriminating abilities are lower than any morphological sieving process.

The last paragraph discussed the spatial discriminating abilities by accumulative SIs. The discriminating ability of a single growth SIE can also be judged by the differential SI as shown in Figure 8.6. For the cylindric method, DSI is constant at  $|x| < 0.5S(\mathcal{E})$ , and zero otherwise. Gauss 1 has decreasing DSI with respect to  $x$ , but

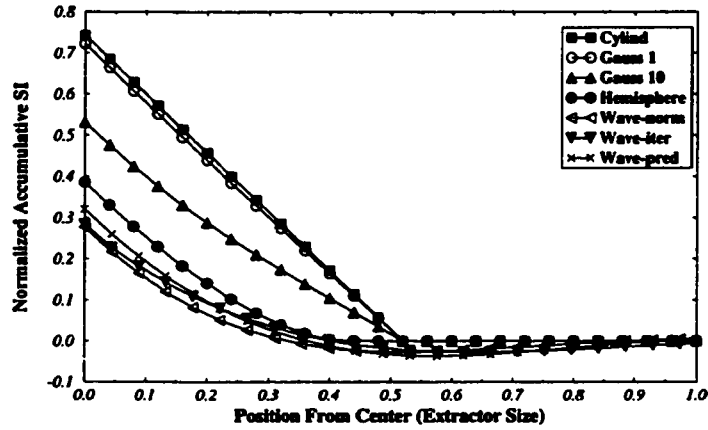


Figure 8.5: Accumulative size information represented spatially by various extractors

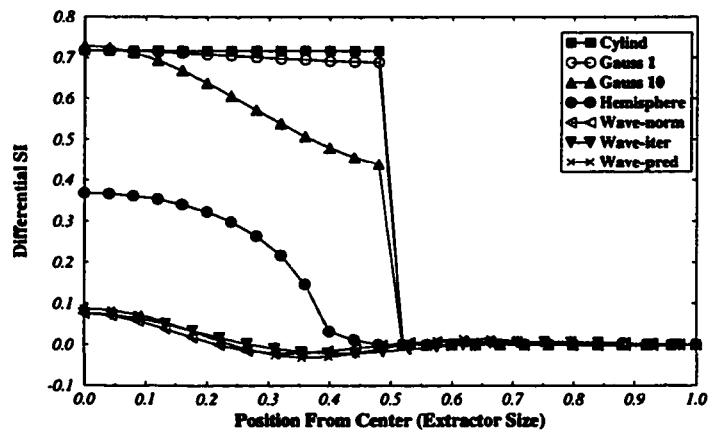


Figure 8.6: Differential size information represented spatially by various extractors

this slope is very small. Gauss 10 shows rapid decreasing with increasing  $x$ . The DSI from the hemispheric method is smaller, but the slope is large. The wavelet methods show similar performance with small DSI, but medium decreasing slope. All of the methods show very small DSIs at  $|x| > 0.5S(\mathcal{E})$ . Thus, the abilities of the SIEs to distinguish the regions  $|x| < 0.5S(\mathcal{E})$  and  $|x| > 0.5S(\mathcal{E})$  is *Cylindric* > *Gauss 1* > *Gauss 10* > *Hemispheric* > *Wavelet Methods*. The abilities of the SIEs to tell the peak  $x = 0$  from the smooth structures at  $x \neq 0$  within  $|x| < 0.5S(\mathcal{E})$  can be judged by  $(DSI_{max} - DSI_{min})$ , where  $DSI_{max}$  and  $DSI_{min}$  are the maximum and minimum DSIs extracted. From the values of  $(DSI_{max} - DSI_{min})$  in Figure 8.6, we found the abilities to distinguish  $x = 0$  and  $x \neq 0$  are *Hemispheric* > *Gauss 10* > *Wavelet Methods* > *Gauss 1* > *Cylindric*.

### Orthogonality of SIEs

In the size information extraction process there might exist a set of SIEs  $\mathcal{E}_i$ ,  $i = 0, 1, 2, \dots$ , which are complete and orthogonal, i.e., for any function  $f(x)$ , we have

$$f = \sum_i \mathcal{E}_i f, \quad (8.7)$$

with

$$\mathcal{E}_k(\mathcal{E}_m f) = \mathcal{E}_k f \cdot \delta_{km}, \quad (8.8)$$

i.e.,  $\mathcal{E}_i$  are orthogonal and idempotent.

In a morphological sieving process, such SIEs produce the same results with sequential and parallel sieving algorithms. In a wavelet method, such SIEs produce the same results with the normal wavelet method and the wavelet iterative method.

An example of the orthogonal SIEs in the sieving process is cylindrical sieving.

The orthogonal SIEs in the wavelet method are any  $H_i$  satisfying  $\sum_i H_i = 1$ , and  $H_i^2 = H_i$ . In Equation (7.2), when  $m$  approaches infinity, the  $H_i$ 's meet the above requirements. That is,

$$H_i(\omega) = \begin{cases} 1, & \frac{1}{a_{i+1}} < \omega \leq \frac{1}{a_i}, \\ 0, & \text{otherwise,} \end{cases} \quad (8.9)$$

thus these wavelet extractors are orthogonal.

## CHAPTER 9. SUMMARY AND FUTURE WORK

This dissertation addresses the removal of cirrus clouds from the  $100\ \mu\text{m}$  IRAS images. It is a continuation, generalization, and improvement of the ASB filtering [Appleton *et al.* 1993]. The objectives of this dissertation are to improve the performance of the sieving process, to introduce more size information extractors which can be used to remove the cirrus clouds from IRAS data, and to analyze the performance of the size information extractors or the filtering process as quantitatively as possible. The first objective was done by incorporating classification into the sieving process. By the classification of the size information, we are able to discuss the cirrus clouds more quantitatively, which is part of the third objective. The classification also enabled a multiple filtering process which improves the filtering results. New extractors were obtained by generalized morphological operations and by using multi-resolution analysis of wavelet. The characterization of the size information extractors are analyzed using a fixed-slope peak. This chapter summarizes the major contributions and suggests areas of future work.

### Summary of Major Contribution

First of all, this dissertation describes an improvement of the ASB filtering and creates a self-consistent filtering process based on size information extraction, classi-

fication, and cirrus noise reduction.

The size information extractions are the most important parts in this filtering process. We employed morphological size information extractors based on different structuring elements. When structuring elements in the sieving process are chosen properly, one is able to obtain purely positive growths. Such a case is granulometry, where larger structuring elements can be decomposed into smaller structuring elements. Another approach to uni-directional extraction is the sequential sieving process.

Classification of the growths was done by the k-means method, where the fractional norm and entropy were introduced to initialize the process. Such initializations produce smaller costs than random initializations. Fractional norm and entropy act as metrics between a vector and a set of vectors.

Based on the classification results, we filter the growth cube which includes cirrus components, estimation and removal. The cirrus estimation methods are the equal characteristic interval area method (by ASB), non-overlapping method, and multiple cirrus estimation. The cirrus removal process is simply a subtraction process. Using appropriate weighting (which is related to a parameter representing the closeness between each pixel and the cirrus) on the cirrus components estimated, we were able to retain the fluxes of the sources to a certain degree. For instance, the flux of a point source with FWHM of 4.2 arc minutes can be retained within a few percent of error. The fluxes of slightly extended sources (FWHM of 7.49 arc minutes), however, due to the insufficiently large structuring elements, and the over-estimation of the cirrus components, can be only retained with less than 20% error. The retentions of the shapes of objects are also studied using simulations. Square-like and long-ellipsis-like

structures are imposed onto I029. The corresponding filtered results reveal that the shapes of the structures imposed are almost perfectly retained if the flux is not a factor in consideration.

The hit-or-miss transform was generalized in this dissertation. A special example of the generalized hit-or-miss transform gave us parameterized erosion ( $\gamma$ -erosion), which bridges the traditional erosion and dilation. The  $\gamma$ -erosion is increasing and translation invariant.  $\gamma$ -erosion was then used for parameterizing closing ( $\gamma$ -closing). Parameterized closing bridges traditional opening and closing. The generalization of the morphological operations enriches the operators available in signal analysis. Also,  $\gamma$ -erosion, and  $\gamma$ -closing behave like median filters when  $\gamma$  is chosen properly. The sieving process was generalized using  $(1 - \gamma)$ -closing in order to obtain bi-directional size information extractors with certain polarities.

This dissertation also gives a guide into the concepts of wavelet theory. The equations relating to the wavelet theory here are more general than those in most of the books about wavelets. For instance, the scaling functions in this dissertation included both low-resolution and high-resolution scaling functions. With the continuous transitions from the continuous wavelet to the semi-continuous wavelet and then to discrete wavelet, one can design one wavelet from another easily.

The wavelet size information extractors are introduced based on a continuous wavelet transform. They are then applied to the problem of cirrus removal, which were proven to be successful. However, their performances were not as good as the morphological sieving process. One very important reason for this is that they are non-polarized. For a case like the IRAS data, we are mostly interested in uni-directional information. Thus, uni-directional size information extractors perform

better. The fluxes lost in the wavelet cases are severe. Even for the point sources, the loss might be up to more than 18%. Two techniques (iterative wavelet and predictive wavelet methods) were introduced to improve the performance, but the improvements were small.

The performance of different size information extractors were discussed based on the size information extracted from a prototype peak. From there, we were able to determine the extracting efficiencies, linearity, and the spatial discrimination of the size information extractors, and thus determine which extractors are good for certain problems such as the IRAS case.

This dissertation discussed the classification (clustering) criterion function design also. This design approach is based on the charge and potential models in physics. Two design models (attraction and repulsion models) were introduced which can be used to design new classifiers.

The following is a summary on the filtering results by various methods with a single image (Figure 9.1, which is the same as Figure 2.1).

When Figure 9.1 was filtered by the sieving process of Gaussian shaped structuring elements (SEs) with equal CI (characteristic interval) area method and  $CI = [10, \dots, 16]$ , we obtained filtered image shown in Figure 9.2 (the same as Figure 3.6(a)). When sigmoidal cirrus weighting is considered, the fluxes of point sources are within 2% of error, the FWHMs of the point sources are within 2.5% of error. The fluxes of slightly extended sources are within 21% of error, the FWHMs of the slightly extended sources are within 9% of error. The cirrus intensity is reduced by a factor of 30 compared with the original image.

When Figure 9.1 was filtered by the sieving process of Gaussian shaped SEs

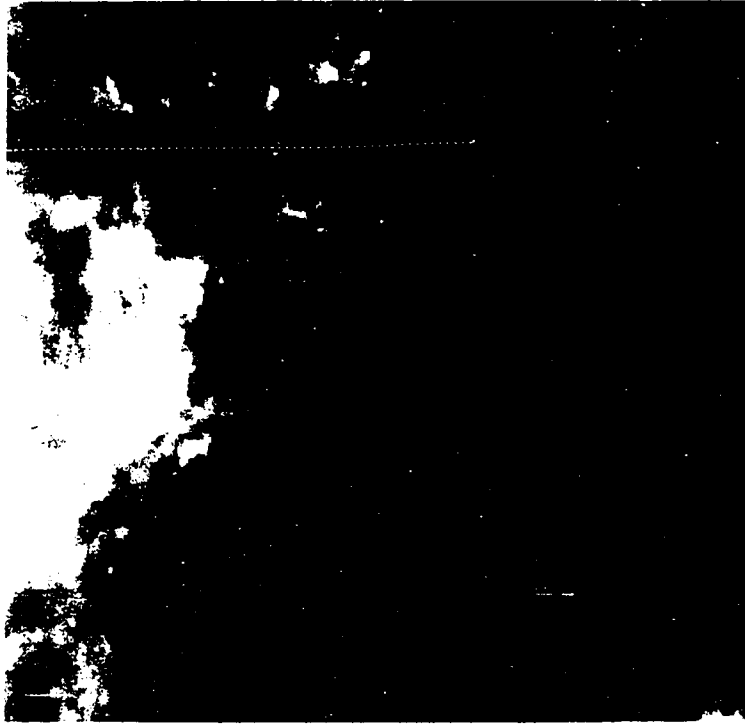


Figure 9.1: The image of ISSA field I029 at  $\lambda = 100\mu m$

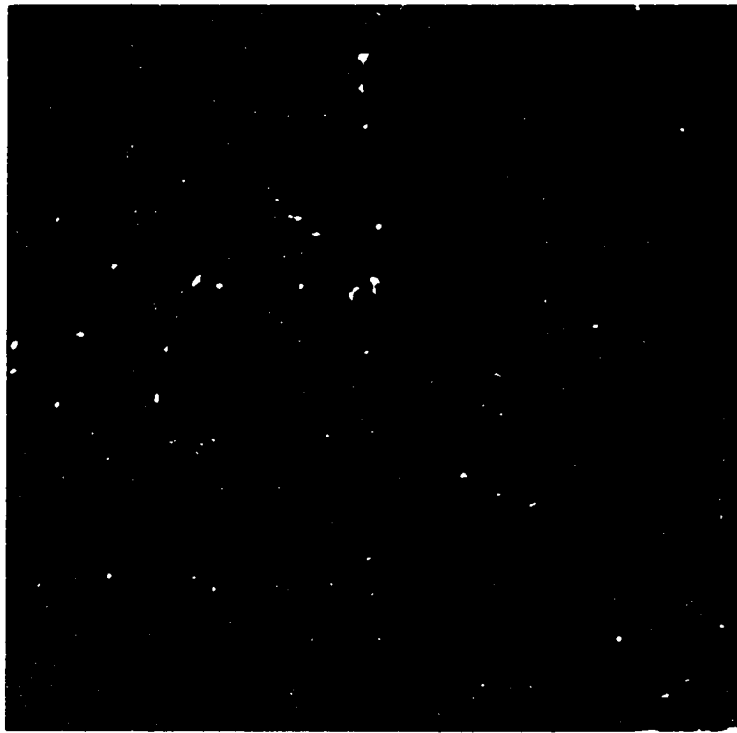


Figure 9.2: The filtered results of Figure 9.1 using equal CI area method

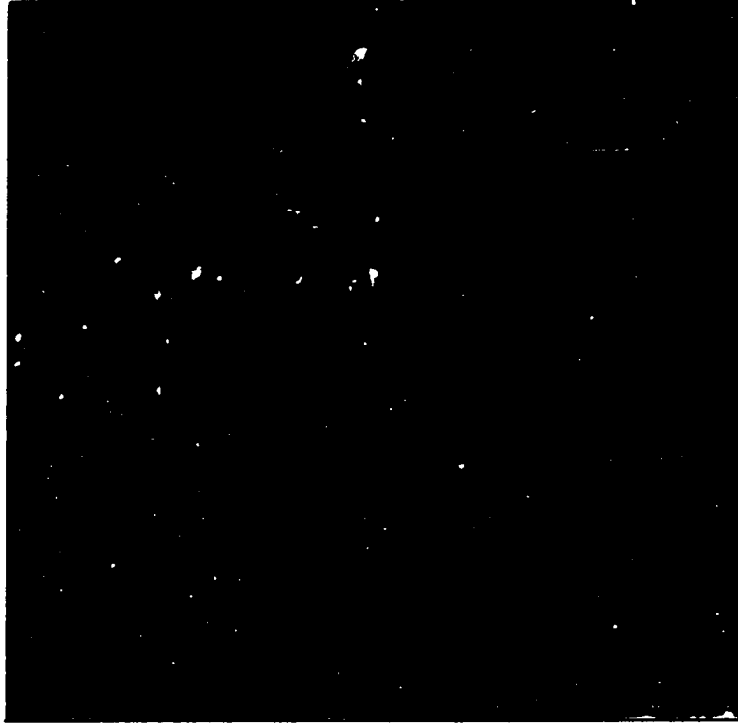


Figure 9.3: The filtered results of Figure 9.1 using non-overlapping method

with the non-overlapping method and  $CI = [13, \dots, 16]$ , we obtained the filtered image shown in Figure 9.3 (the same as Figure 3.8). The fluxes of point sources are within 2% of error, the FWHMs of the point sources are within 3.2% of error. The fluxes of slightly extended sources are within 15% of error, the FWHMs of the slightly extended sources are within 5.8% of error. The cirrus intensity is reduced by a factor of around 15.

When Figure 9.1 was filtered by the sieving process of Gaussian shaped SEs with the multi-cirrus filtering method, we obtained filtered image shown in Figure 9.4 (the same as Figure 3.9). When the sigmoidal cirrus weighting is considered, the fluxes of point sources are within 1.4% of error, the FWHMs of the point sources are within



Figure 9.4: The filtered results of Figure 9.1 using multi-cirrus filtering method

1.8% of error. The fluxes of slightly extended sources are within 18% of error, the FWHMs of the slightly extended sources are within 10% of error. The cirrus intensity is reduced by a factor of around 35.

It is obvious that the retentions of the intensity and FWHM are in conflict with the reduction of cirrus intensity. Therefore, a choice of the method to be used is based on whether we emphasize object identification or flux and shape measurements. Whichever methods chosen, the filtering can have a performance acceptable by the astronomers.

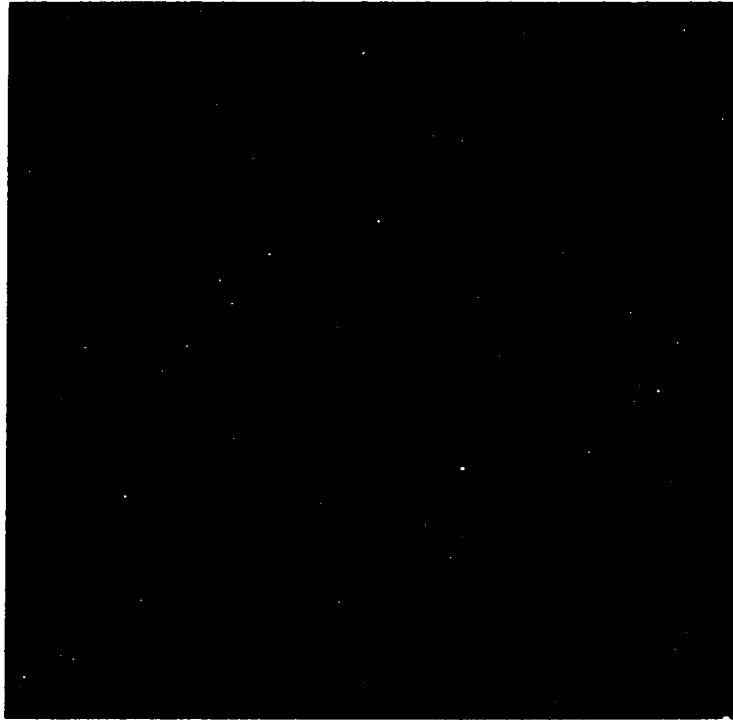
Structuring elements with the shapes of cylinders and hemispheres were also used in the sieving process. When Figure 9.1 was filtered by the sieving process



Figure 9.5: The filtered image of Figure 9.1 with hemispheric structuring elements using the equal CI area method

using hemispherical shaped SEs with the equal CI area method and  $CI = [8, \dots, 12]$ , we obtained the filtered image shown in Figure 9.5 (the same as Figure 4.3). When the sigmoidal cirrus weighting is considered, the fluxes of point sources are within 2% of error, the FWHMs of the point sources are within 2.9% of error. The fluxes of slightly extended sources are within 27% of error, the FWHMs of the slightly extended sources are within 10.6% of error. The cirrus is reduced by a factor of around 30.

When Figure 9.1 was filtered by the sieving process using cylindrical shaped SEs with the equal CI area method and  $CI = [8, \dots, 12]$ , we obtained the filtered image



**Figure 9.6:** The filtered image of Figure 9.1 with cylindric structuring elements using the equal CI area method

shown in Figure 9.6 (the same as Figure 4.4). The fluxes of point sources are within 1.5% of error, the FWHMs of the point sources are within 6% of error. The fluxes of slightly extended sources are within 0.6% of error, the FWHMs of the slightly extended sources are within 2.6% of error. The cirrus intensity is reduced by a factor of around 7.

Different structuring elements have different information extraction efficiencies. When cylindrical structuring elements are used, the extractions have large efficiencies which give better intensity retention on extended objects. The cirrus intensity after the filtering, however, is much stronger than the results by hemispherical and

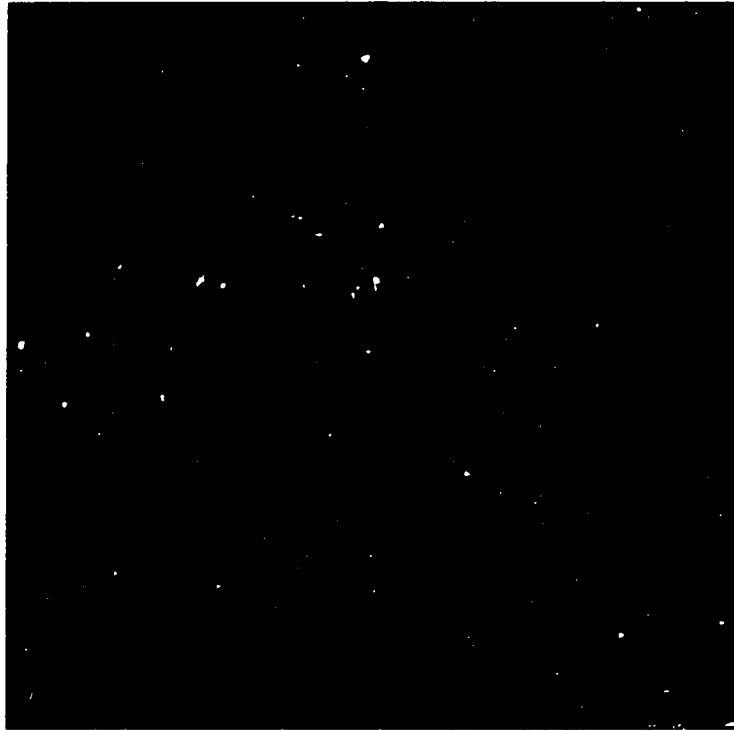


Figure 9.7: The filtered image of Figure 9.1 by sequential sieving process, Gaussian SEs, equal CI area method, and sigmoidal noise weighting

Gaussian structuring elements.

We also processed the image in Figure 9.1 by Gaussian shaped SEs in a *sequential* sieving process. The filtered image is shown in Figure 9.7 (the same as Figure 4.6). The fluxes of point sources are within 6% of error, the FWHMs of the point sources are within 1.4% of error. The fluxes of slightly extended sources are within 33% of error, the FWHMs of the slightly extended sources are within 14% of error. The cirrus is reduced by a factor of around 20. The sequential sieving usually has smaller extraction efficiency than the corresponding parallel sieving process.

Three wavelet methods, namely, normal wavelet, iterative wavelet, and predictive

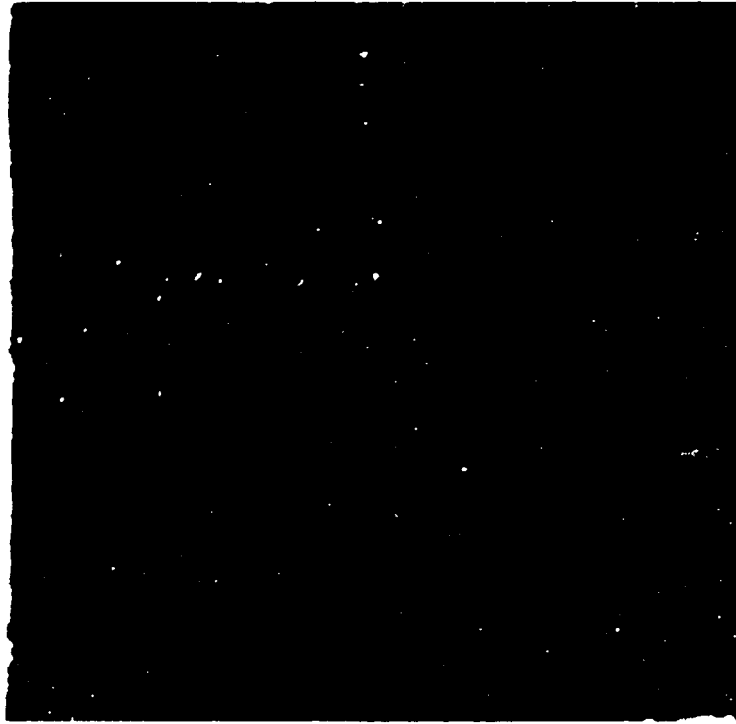


Figure 9.8: The filtered image of Figure 9.1 using multi-cirrus filtering with the normal wavelet method

wavelet methods were employed to filter the cirrus noise. The wavelet methods did not give good performance compared with the morphological methods.

Figure 9.8 (the same as Figure 7.5) shows the filtered image of Figure 9.1 by the normal wavelet method. The fluxes of point sources are within 18% of error, the FWHMs of the point sources are within 3.8% of error. The fluxes of slightly extended sources are within 37% of error, the FWHMs of the slightly extended sources are within 10% of error. The cirrus intensity is reduced by a factor of around 15.

Figure 9.9 (the same as Figure 7.7) shows the filtered image of Figure 9.1 by the iterative wavelet method. The fluxes of point sources are within 17% of error, the



**Figure 9.9:** The filtered image of Figure 9.1 using multi-cirrus filtering with the iterative wavelet method

FWHMs of the point sources are within 3.6% of error. The fluxes of slightly extended sources are within 34% of error, the FWHMs of the slightly extended sources are within 9.8% of error. The cirrus intensity is reduced by a factor of around 15.

Figure 9.10 (the same as Figure 7.9) shows the filtered image of Figure 9.1 by the predictive wavelet method. The fluxes of point sources are within 16% of error, the FWHMs of the point sources are within 3.6% of error. The fluxes of slightly extended sources are within 20% of error, the FWHMs of the slightly extended sources are within 5.4% of error. The cirrus intensity is reduced by a factor of around 13.

The errors for the fluxes and FWHMs of the point and slightly extended sources



**Figure 9.10:** The filtered image of Figure 9.1 using multi-cirrus filtering with the predictive wavelet method

determined by various methods are summarized in Table 9.1. In the first row of this table, "G-EA" means Gaussian with equal CI area method, "G-NO" means Gaussian with non-overlapping method, "G-MF" means Gaussian with multi-cirrus filtering, "Hemi" means hemispheric SE sieving process, "Cylin" means cylindrical SE sieving process, G-SF means Gaussian sequential filtering, "Wa-N" means normal wavelet method, "Wa-I" means iterative wavelet method, and "Wa-P" means predictive wavelet method. In the first column of this table, "Flux-P" means the fluxes of the point sources, "FWHM-P" means FWHMs of the point sources, "Flux-E" means the fluxes of the slightly extended sources, and "FWHM-E" means the FWHMs of the slightly extended sources. From the numbers in the table, we see that the Gaussian equal CI area method, the Gaussian non-overlapping method, the Gaussian multi-cirrus filtering, and cylindrical SE sieving are superior than the other five methods. The Gaussian non-overlapping method and cylindrical SE sieving preserve fluxes and FWHMs better than other methods. But they do not reduce the cirrus intensities (by factors of 15 and 7 for the Gaussian non-overlapping method and cylindrical SE sieving, respectively) so well as the Gaussian equal CI area method (by a factor of 30) and the Gaussian multi-cirrus filtering (by a factor of 35). We recommend the Gaussian equal CI area method and the Gaussian multi-cirrus filtering because they reduce cirrus intensities dramatically which enables us to identify sources easily, and because they also give reasonable flux and FWHM retentions. The reasons mentioned above motivated our all-sky filtering of the IRAS data using the Gaussian equal CI area method. Among the other five methods, the Gaussian sequential filtering performs better than the hemispherical SE sieving process. The three wavelet methods perform similarly, their performance are much worse than any morphological method.

**Table 9.1: The errors for the fluxes and FWHMs of the point and slightly extended sources determined by various methods**

	G-EA	G-NO	G-MF	Hemi	Cylin	G-SF	Wa-N	Wa-I	Wa-P
<b>Flux-P</b>	2%	2%	1.4%	2%	1.5%	6%	18%	17%	16%
<b>FWHM-P</b>	2.5%	3.2%	1.8%	2.9%	6%	1.4%	3.8%	3.6%	3.6%
<b>Flux-E</b>	21%	15%	18%	27%	0.6%	33%	37%	34%	20%
<b>FWHM-E</b>	9%	5.8%	10%	10.6%	2.6%	14%	10%	9.8%	5.4%

### **Future Work**

There are many investigations to be continued based on this dissertation. We can use the generalized hit-or-miss transform by defining different relation kernels  $\mathcal{R}_1$  and  $\mathcal{R}_2$  to find more morphological operators. Secondly, we need to pursue the justifications of the size information extractors, especially using prototypes with varying sloped peaks. Thirdly, the cirrus removal is not perfect due to the non-linearity of the sieving process. Thus, a non-linear filtering process might help to improve the performance of the filter.

## APPENDIX A. SET THEORY AND MATHEMATICAL MORPHOLOGY

Mathematical morphology was created in 1964 when G. Matheron was investigating the relationships between the geometry of porous media and their permeabilities, and when J. Serra was quantifying the petrography of iron ores. This new discipline of image analysis deals with the geometry of an object with sets. Since the birth of mathematical morphology, the field of image analysis and processing has benefited so much. For example, mathematical morphology was employed to extract the edge of an image, to obtain the size information of images, to obtain the skeleton of images, to thin, etc. [Serra 1982].

Geometry of an object is represented by a set in mathematical morphology, thus the morphological operations are based on set operations [Serra 1982; Matheron 1975]. In order to understand the concepts of morphology, one first needs to understand the concepts of set theory. In this Appendix, we will introduce the concepts of set theory. After the introduction of set theory, we then discuss the hit-or-miss transform. Afterwards, basic morphological operators erosion, and dilation are introduced. Closing and opening are then discussed using dilation and erosion. The morphological concepts are extended into gray-scale images thereafter.

Part of the material in this Appendix follows Hrbacek and Jech [1978], Serra

[1982], and Dougherty [1992].

### Set Theory

Set theory deals with collections of objects [Hausdorff 1978; Hrbacek and Jech 1978].

**Definition A.1** *A set  $S$  is a collection of a whole definite, distinct objects of our intuition or thought. The objects are called elements or members of the set  $S$ . If  $x$  is one of the elements of  $S$ , then we say  $x \in S$  ( $x$  is in  $S$ ).*

There are some important set operators such as union, intersection, complementary, difference, symmetric difference, etc.

**Definition A.2** *For two sets  $S_1$  and  $S_2$ ,*

- (1) *The union of two sets  $S_1$  and  $S_2$  is the collection of the distinct elements in  $S_1$  or  $S_2$ , denoted as  $S_1 \cup S_2$ .*
- (2) *The intersection of sets  $S_1$  and  $S_2$  is the collection of the distinct elements which belongs to  $S_1$  and  $S_2$ , denoted as  $S_1 \cap S_2$ .*
- (3) *If all the elements of  $S_1$  belong to  $S_2$ , and we take  $S_2$  as the entire set (or whole set, or universe) in consideration, then the complementary set of  $S_1$  is the collection of elements in  $S_2$  but not in  $S_1$ , denoted as  $S_1^c$ .*
- (4) *The difference of  $S_1$  and  $S_2$  is the collection of elements of  $S_1$  which do not belong to  $S_2$ , denoted as  $S_1 - S_2$ .*

(5) The symmetric difference of  $S_1$  and  $S_2$  is defined as  $S_1 \Delta S_2 = (S_1 - S_2) \cup (S_2 - S_1)$ .

We can also define other operators on sets. All the operators form an operator set  $\mathcal{O}$ .

Figure A.1 shows graphically two sets  $A$  and  $B$ ,  $A \cap B$ ,  $A \cup B$ ,  $A^c$ , and  $(A - B)$ .

Some of the properties of the operators are listed below.

**Proposition A.1** *The set operators  $\cup$  and  $\cap$  have following properties.*

(1) *Commutativity*

$$A \cap B = B \cap A, \quad (\text{A.1})$$

$$A \cup B = B \cup A. \quad (\text{A.2})$$

(2) *Associativity*

$$(A \cap B) \cap C = A \cap (B \cap C), \quad (\text{A.3})$$

$$(A \cup B) \cup C = A \cup (B \cup C). \quad (\text{A.4})$$

(3) *Distributivity*

$$A \cap (B \cup C) = (A \cap B) \cup (A \cap C), \quad (\text{A.5})$$

$$A \cup (B \cap C) = (A \cup B) \cap (A \cup C). \quad (\text{A.6})$$

(4) *DeMorgan's Laws*

$$C - (A \cap B) = (C - A) \cup (C - B), \quad (\text{A.7})$$

$$C - (A \cup B) = (C - A) \cap (C - B). \quad (\text{A.8})$$

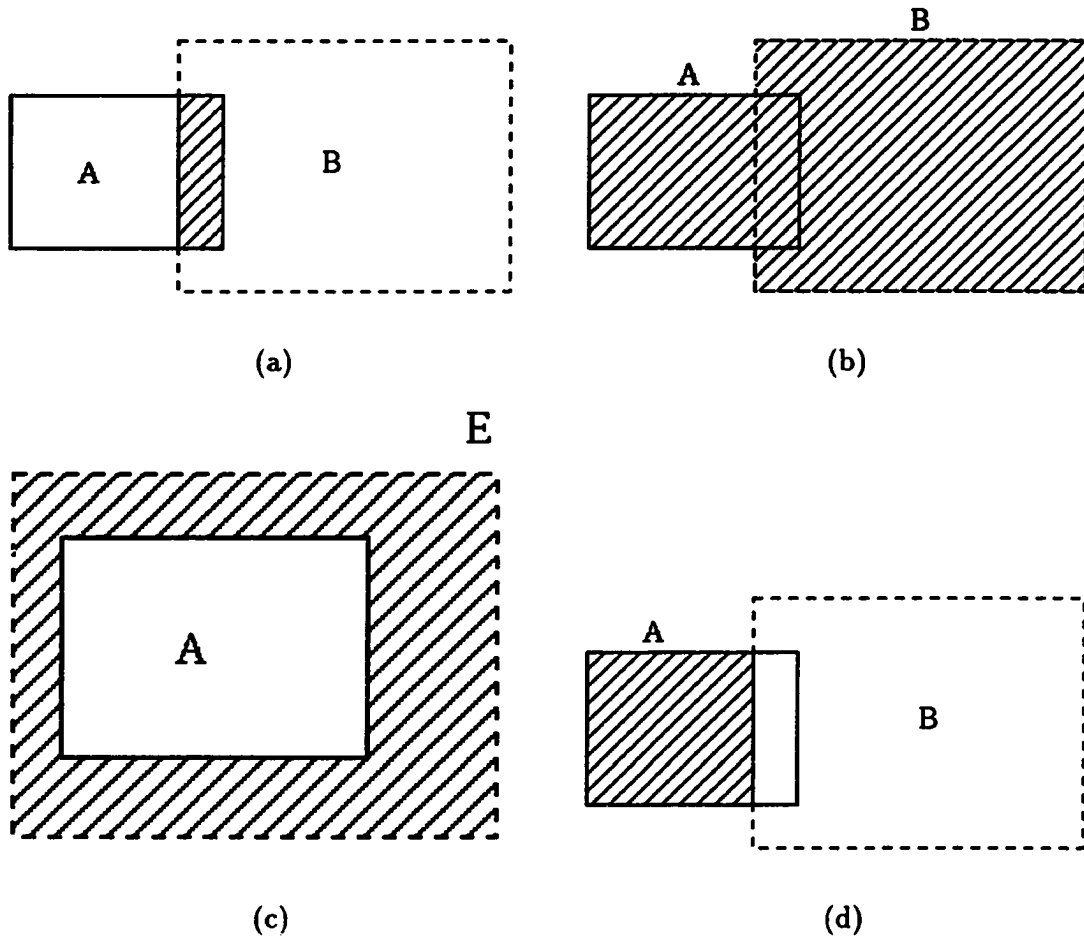


Figure A.1: Operations between sets  $A$  (solid-lined rectangle) and  $B$  (dashed-lined rectangle): (a)  $A \cap B$  (shaded); (b)  $A \cup B$  (shaded); (c)  $A^c$  (whole set is  $E$ , the dashed-lined rectangle; result is shaded); and (d)  $A - B$  (shaded)

The proof for these relations can be found in [Hrbacek and Jech 1978].

Sets are related to each other by relation kernels.

**Definition A.3** *If we have two sets  $S_1$  and  $S_2$ , then we say*

(1)  $S_1 = S_2$ , if the collection of elements of  $S_1$  is identical to that of  $S_2$ , we denote “not =” as  $\neq$ .

(2)  $S_1 \subseteq S_2$  if all the elements of  $S_1$  belong to  $S_2$ , we denote “not  $\subseteq$ ” as  $\not\subseteq$ .

(3)  $S_1 \subset S_2$  if  $S_1 \subseteq S_2$  and  $S_1 \neq S_2$ , we denote “not  $\subset$ ” as  $\not\subset$ .

*All the relation kernels form a relation set  $\mathcal{R}$ .*

### Hit-or-Miss Transform

Mathematical morphology is based on the *hit-or-miss transform* [Serra 1982; Heijmans 1994] introduced by Serra from the set theory point of view. Before we introduce the hit-or-miss transform, we define the translation and reflection of a set first.

**Definition A.4** *If we denote the whole set (universe) in consideration as  $E$ , then*

(1) *For an element  $h \in E$ , if a set  $X = \{x\}$  has the property that  $x + h \in E$  for all  $x \in X$ , then  $X_h = \{x + h; x \in X\}$  is called the translation of set  $X$  by  $h$ .*

(2) *For a scalar  $\lambda$ , a set  $X = \{x\}$ , if  $\lambda x \in E$ , for all  $x \in X$ , then  $\lambda X = \{\lambda x; x \in X\}$  is called the homothetic of set  $X$  by the scalar  $\lambda$ .*

(3) *The origin of the set  $E$  is 0 if  $X_0 = X$ , for all  $X \subset E$ .*

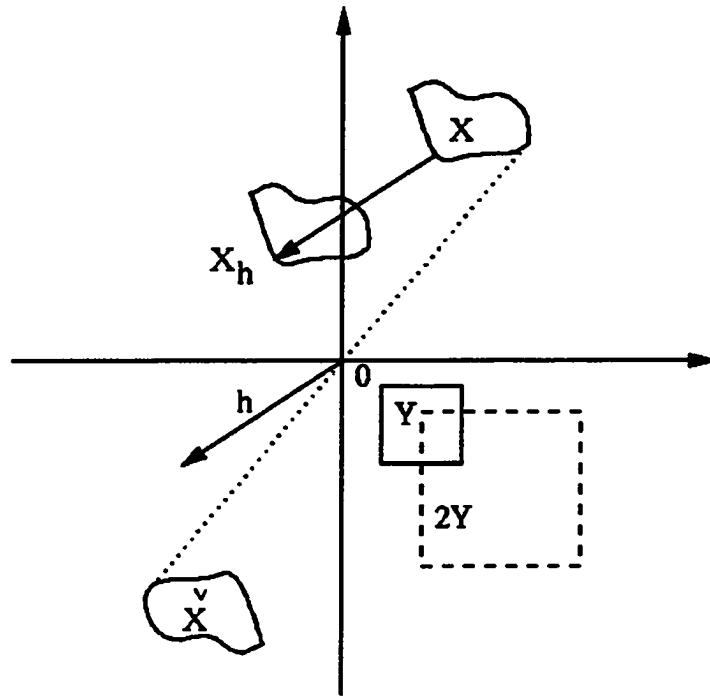


Figure A.2: Translation, homothetic and reflection of sets. The origin  $0$  is denoted as  $0$ ,  $X_h$  is the translation of  $X$  by  $h$ ,  $\check{X}$  is the reflection of  $X$ , and  $2Y$  is the homothetic of  $Y$  with a factor of 2

- (4) The reflection of an element  $x \in X$  is denoted as  $(-x)$ , if it has the property that  $(-x) + x = 0$ . The collection of the reflections of elements in  $X$  forms the reflection of  $X$  and is denoted as  $\check{X} = \{-x; x \in X\}$ .

Figure A.2 shows the concepts mentioned above.

With the definitions above, we are now ready for the definition of hit-or-miss transform.

**Definition A.5** Let the universe be  $E = \{x\}$ . A structuring element is  $B = (B^1, B^2)$ , with  $B^1 \cap B^2 = \emptyset$  (the notation  $\emptyset$  means empty set, i.e., it contains no

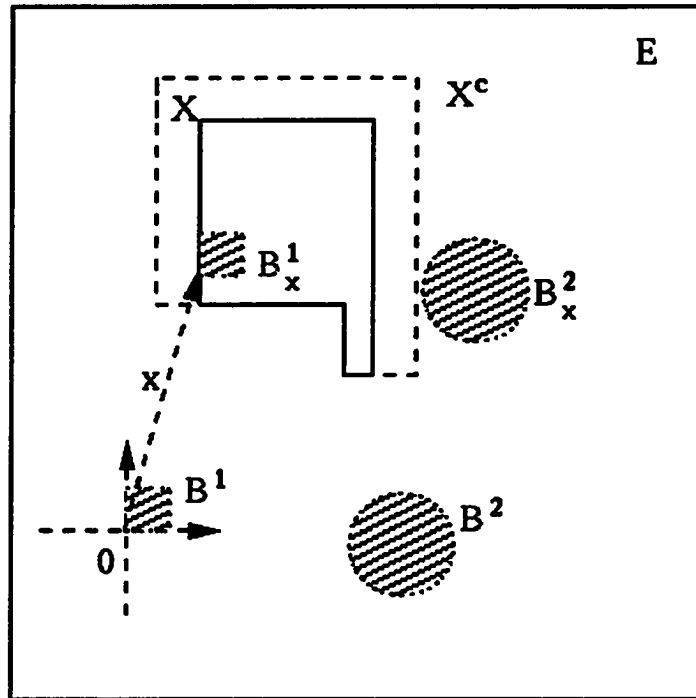


Figure A.3: Hit-or-miss transform of  $X$  (dashed lined) with structuring elements  $B = (B^1, B^2)$  (shaded). The result is shown as solid lines

element at all). For a set  $X \subseteq E$ , the hit-or-miss transform of  $X$  with structuring element  $B$  is

$$X \circledast B = \{x : B_x^1 \subset X; B_x^2 \subset X^c; x \in E\} \quad (\text{A.9})$$

where  $B_x^1$  and  $B_x^2$  are translations of sets  $B^1$  and  $B^2$  by  $x$ ,  $X^c$  is the complementary set of set  $X$ .

Figure A.3 is an illustration of hit-or-miss transform.

### Erosion and Dilation

In the hit-or-miss transform, if we choose  $B^2 = \emptyset$ , then  $B_x^2 = \emptyset \in X^c$  holds for all  $x \in \mathcal{E}$ . This special case of hit-or-miss transform is called erosion [Serra 1982]. If we denote the erosion of  $X$  by  $B$  as  $X \ominus B$  (be careful with the notation  $\ominus$ , because in different literature it was used to denote Minkowski subtraction or erosion), then we have

$$X \ominus B = \{x : B_x \subset X\}. \quad (\text{A.10})$$

In mathematical morphology, each operation  $\Psi$  has its dual operation  $\Psi^*$  with the relation [Serra 1982; Heijmans 1994]

$$\Psi^*(X, B) = [\Psi(X^c, B)]^c, \quad (\text{A.11})$$

where the superscript  $c$  again denotes the complementary operation.

Dilation is the dual operation of erosion, therefore if we denote dilation of  $X$  by  $B$  as  $X \oplus B$ , then we have

$$X \oplus B = [X^c \ominus B]^c. \quad (\text{A.12})$$

Figure A.4 shows erosion and dilation of set  $X$  by  $B$ .

Erosion and dilation are closely related to Minkowski subtraction  $\ominus_m$  and addition  $\oplus_m$  [Minkowski 1903; Hadwiger 1957; Serra 1982] defined by

$$X \ominus_m B = \bigcap_{b \in B} X_b, \quad (\text{A.13})$$

$$X \oplus_m B = \bigcup_{b \in B} X_b. \quad (\text{A.14})$$

Erosion is expressed in terms of  $\ominus_m$  by the following equation,

$$X \ominus B = \{x : B_x \subset X\} = \bigcap_{y \in B} X_{-y} = \bigcap_{-y \in B} X_y = X \ominus_m \check{B}. \quad (\text{A.15})$$

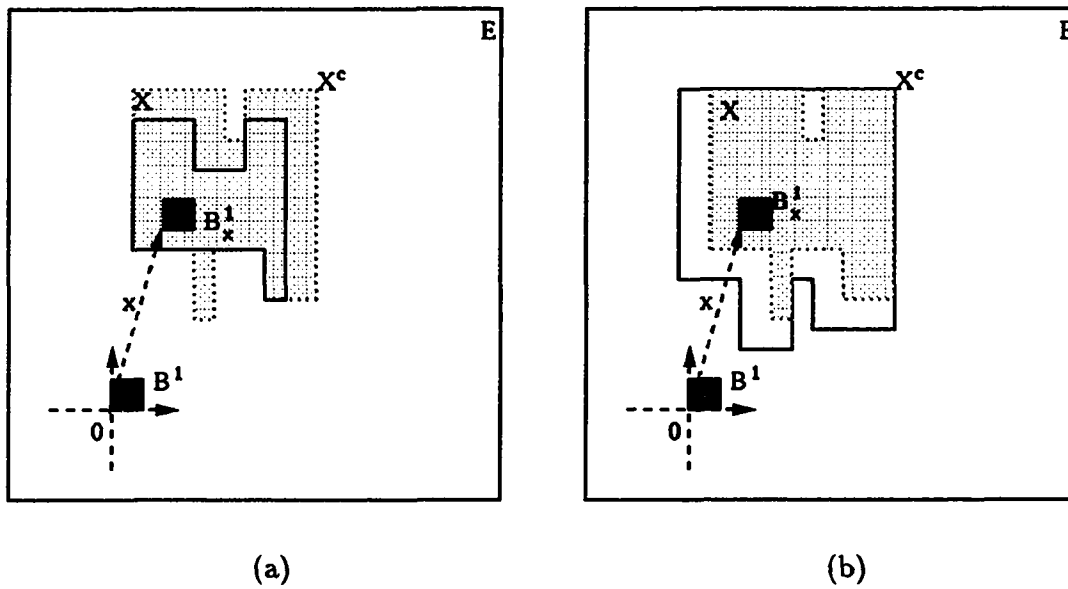


Figure A.4: Erosion (a) and dilation (b) of  $X$  by  $B$ . The results are shown as solid lines,  $X$  as shaded area

Using the duality between erosion and dilation, Equations (A.3), (A.4), (A.7), and (A.8), it is not difficult to prove that

$$X \oplus B = \bigcup_{v \in \check{B}} X_v = X \oplus_m \check{B}. \quad (\text{A.16})$$

**Proposition A.2** *Dilation and erosion have some unique properties [Serra 1982],*

(1) *Dilation and erosion of set  $X$  by a point  $x$  are the same,*

$$X \oplus \{x\} = X \ominus \{x\} = X_{-x} \quad (\text{A.17})$$

(2) *Distributivity*

$$X \oplus (B \cup B') = (X \oplus B) \cup (X \oplus B'), \quad (\text{A.18})$$

$$X \ominus (B \cup B') = (X \ominus B) \cap (X \ominus B'), \quad (\text{A.19})$$

$$\lambda(X \oplus B) = (\lambda X) \oplus (\lambda B), \quad (\text{A.20})$$

$$\lambda(X \ominus B) = (\lambda X) \ominus (\lambda B), \quad (\text{A.21})$$

*i.e., the homothetic of dilation (or erosion) of  $X$  by  $B$  can be obtained by taking homothetic of  $X$  and  $B$  first, dilation (or erosion) second.*

(3) *Iterativity*

$$(X \ominus B) \ominus B' = X \ominus (B \oplus \check{B}'), \quad (\text{A.22})$$

$$(X \oplus B) \oplus B' = X \oplus (B \oplus \check{B}'). \quad (\text{A.23})$$

(4) *Increasing and inclusive*

*If  $X \subset X'$ , then*

$$X \ominus B \subset X' \ominus B, \quad (\text{A.24})$$

$$X \oplus B \subset X' \oplus B. \quad (\text{A.25})$$

If  $B \subset B'$ , then

$$X \ominus B \supset X \ominus B', \quad (\text{A.26})$$

$$X \oplus B \subset X \oplus B'. \quad (\text{A.27})$$

(5) *Translation invariant*

$$X_{\mathbf{v}} \oplus B = (X \oplus B)_{\mathbf{v}}, \quad (\text{A.28})$$

$$X_{\mathbf{v}} \ominus B = (X \ominus B)_{\mathbf{v}}. \quad (\text{A.29})$$

Figure A.5 shows some of the properties mentioned above. For more detailed discussion on the properties of dilation and erosion, please refer to [Serra 1982].

### Opening and Closing

Dilation and erosion are one step operations between two sets  $X$  and  $B$ . Two step operations between two sets give us opening and closing [Serra 1982].

Opening of set  $X$  by structuring element  $B$  is defined as

$$X \circ B = (X \ominus B) \oplus \check{B}. \quad (\text{A.30})$$

The dual operation of opening is called closing

$$X \bullet B = [X^c \circ B]^c = (X \oplus B) \ominus \check{B}. \quad (\text{A.31})$$

Opening and closing have following properties.

**Proposition A.3** *The properties of opening and closing are,*

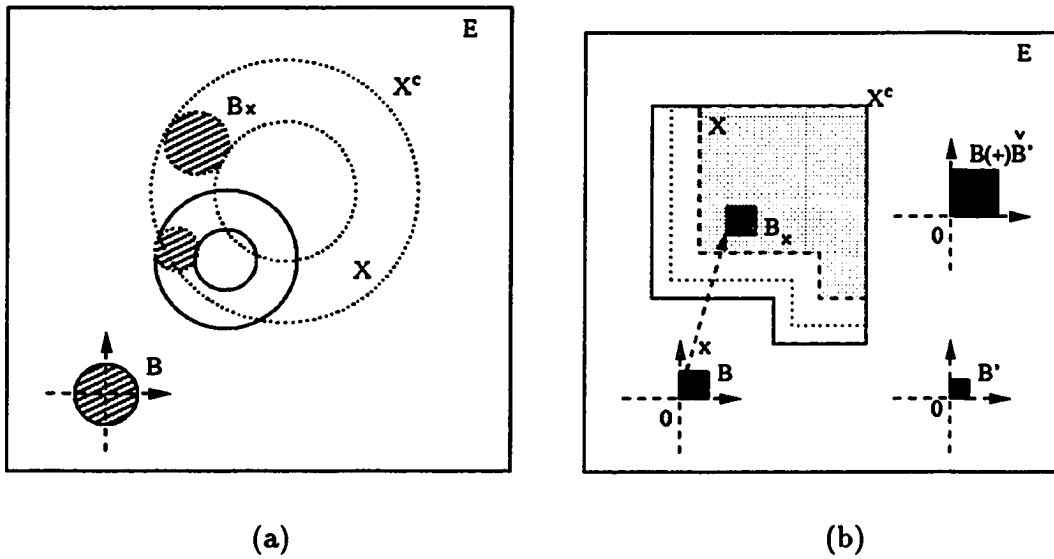


Figure A.5: (a) Homothetic of  $X \ominus B$  (small dotted-lined circle) by a factor  $\lambda$  (small solid-lined circle) is equivalent to homothetic of  $X$  and  $B$  followed by erosion; and (b) dilation of  $X$  by  $B \oplus B'$  (solid lines) is equivalent to dilation by  $B$  (dotted lines) and then dilation by  $B'$  (solid lines)

**(1) Extensivity**

$$X \circ B \subset X, \quad (\text{A.32})$$

$$X \bullet B \supset X. \quad (\text{A.33})$$

**(2) Increasing**

If  $X' \subset X$ , then

$$X' \bullet B \subset X \bullet B, \quad (\text{A.34})$$

$$X' \circ B \subset X \circ B. \quad (\text{A.35})$$

**(3) Idempotent**

$$(X \bullet B) \bullet B = X \bullet B, \quad (\text{A.36})$$

$$(X \circ B) \circ B = X \circ B, \quad (\text{A.37})$$

*i.e., opening or closing a set  $X$  by structuring element  $B$  more than once is not necessary.*

**(4) Translation invariant**

$$X_y \bullet B = (X \bullet B)_y, \quad (\text{A.38})$$

$$X_y \circ B = (X \circ B)_y. \quad (\text{A.39})$$

### **An Example: Small Particle Extraction Using Opening**

Opening and closing are very useful in removing small particles embedded inside a large matrix. One example is the void extraction from composite material [He et

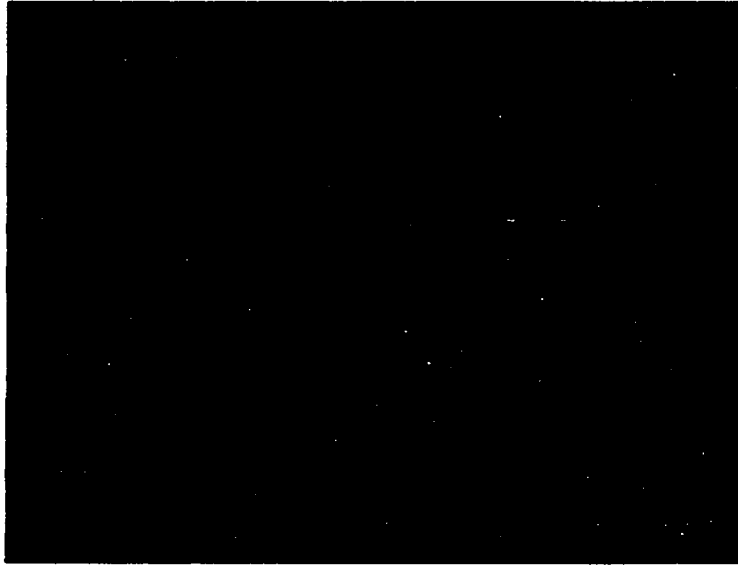


Figure A.6: A photograph of composite material

*al.* 1994b]. Figure A.6 is a photograph taken by a microscope from a NiFeAl/W composite material.

The circular objects are W (tungsten) fibers, and the materials surrounding the W fibers are NiFeAl alloy matrix. In the NiFeAl matrix, there are voids produced in the alloying process (voids are small dark particles). Since the fraction of voids in the material is closely related to the mechanical properties of the composite material, our objective is to find the void fractions at different sites of the composite material. The sample is thin and long, so we took 27 photographs from the sample with the size of photograph similar to that of Figure A.6. In order to count the area of the voids, we first digitized the photographs, and then used a painting program to paint the inside of the W fibers giving Figure A.7. Figure A.7 was thresholded to get Figure A.8.

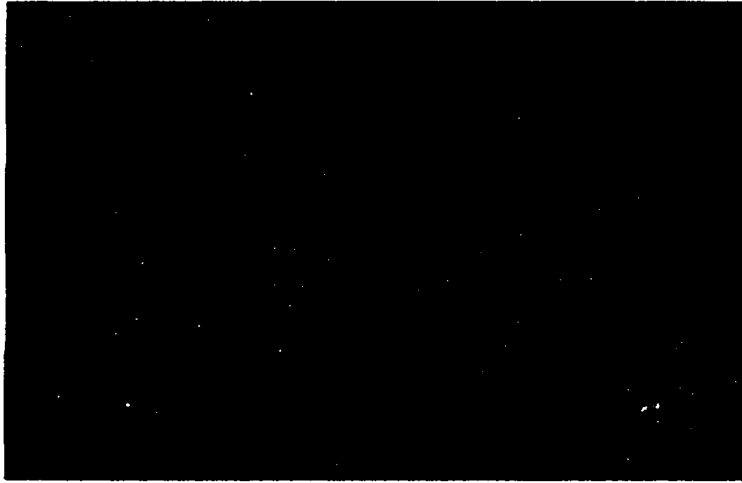


Figure A.7: The W fibers (circles) are painted black

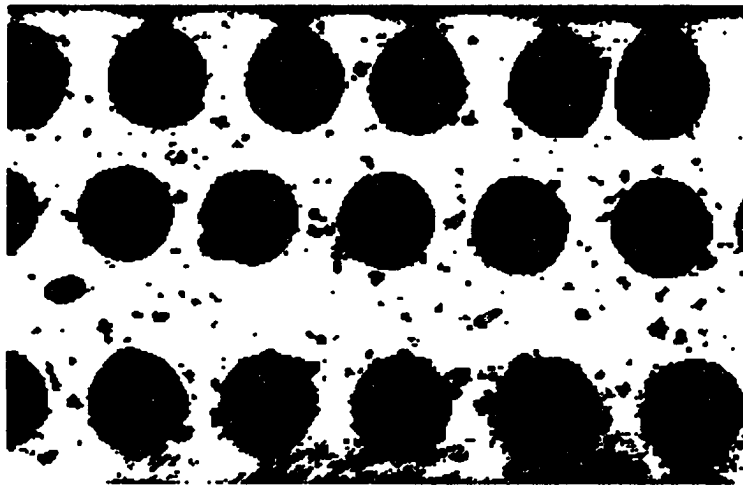


Figure A.8: Figure A.7 is thresholded

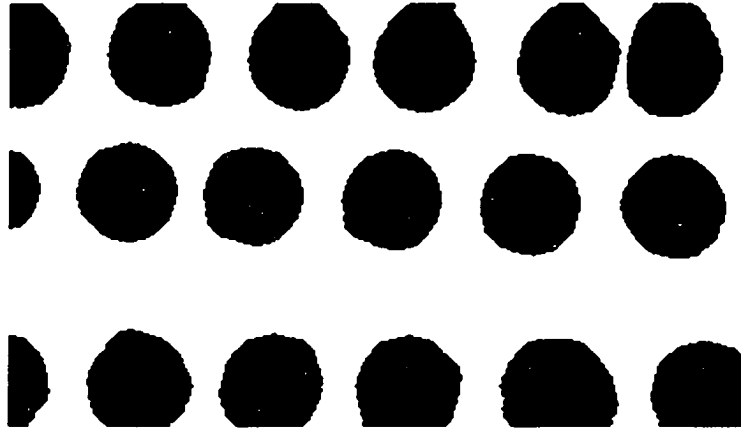


Figure A.9: Using opening to remove small particles

Using the opening with a circular structuring element which is larger than the size of voids and smaller than the size of the W fibers, we obtained Figure A.9. It is obvious that in Figure A.9, the voids are totally removed. Subtracting Figure A.9 from Figure A.8, we got Figure A.10 which contains only voids.

But in Figure A.10, there still were some circular traces of the W fibers. These traces consist of very small sized objects, so we applied opening to Figure A.10 with a circular structuring element which is a little bit larger than the size of the objects in the W fiber traces. In this way, we obtained Figure A.11.

Counting the area of the voids from Figure A.11 is easy now.

### Gray-scale Mathematical Morphology

#### Top-surface and umbra transforms

In this section, we are going to discuss the top-surface and umbra transforms in the  $n$ -dimensional real space  $\mathbb{R}^n$ , with its vector  $\vec{x} = \{x_1, x_2, \dots, x_n\}$ . The results are

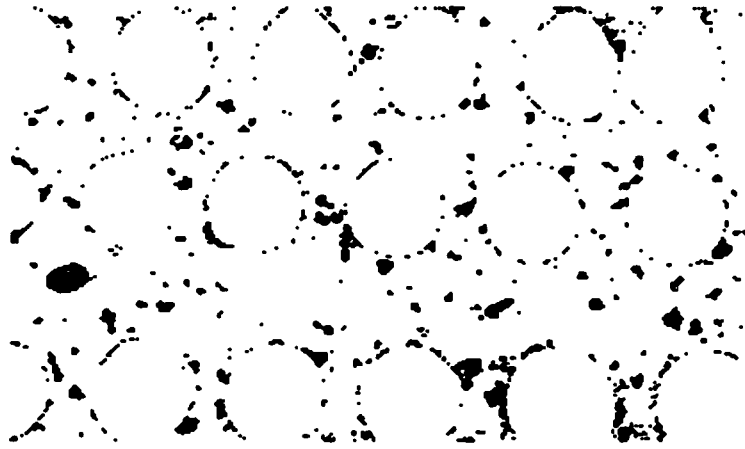


Figure A.10: Subtraction of Figure A.8 by Figure A.9 to obtain voids



Figure A.11: Applying opening on Figure A.10, we remove circular traces of W fibers

extensible to other linear spaces without too much confusion.

First we define a 1-dimensional direction in  $\mathbb{R}^n$  as *the top direction*. Without loss of generality, we choose the positive direction of the  $n$ th real axis as the top direction. The top-surface and umbra transforms of a set in the space  $\mathbb{R}^n$  are then defined as following [Heijmans 1994; Dougherty 1992].

**Definition A.6** For a set  $X \subset \mathbb{R}^n$ , the top-surface transform of the set  $X$  is

$$\mathcal{T}(X) = \{\vec{x} : x_n \geq y_n; \text{ if } x_1 = y_1, \dots, x_{n-1} = y_{n-1}; \vec{x}, \vec{y} \in \partial X\}, \quad (\text{A.40})$$

where  $\partial X$  is the boundary of  $X$ .

The umbra transform is defined as

$$\mathcal{U}(X) = \{\vec{x} : x_n \leq y_n; \vec{y} = \mathcal{T}(X); \text{ if } x_1 = y_1, \dots, x_{n-1} = y_{n-1}\}. \quad (\text{A.41})$$

Figure A.12 is an illustration of the top-surface and the umbra of set  $X$ .

### Gray-scale morphology by top-surface and umbra transforms

Gray-scale mathematical morphology can be explained by the top-surface and umbra transforms [Dougherty 1992]. First we need to emphasize that the top direction is the positive gray-scale direction. We denote the gray-scale image by  $X$  and gray-scale structuring element by  $B$ , then gray-scale dilation and erosion are defined as

$$\text{Dilation: } X \oplus B = \mathcal{T}(\mathcal{U}[X] \oplus \check{\mathcal{U}}[B]), \quad (\text{A.42})$$

$$\text{Erosion: } X \ominus B = \mathcal{T}(\mathcal{U}[X] \ominus \mathcal{U}[B]). \quad (\text{A.43})$$

Gray-scale opening and closing are then defined as

$$\text{Opening: } X \odot B = (X \ominus B) \oplus \check{B}, \quad (\text{A.44})$$

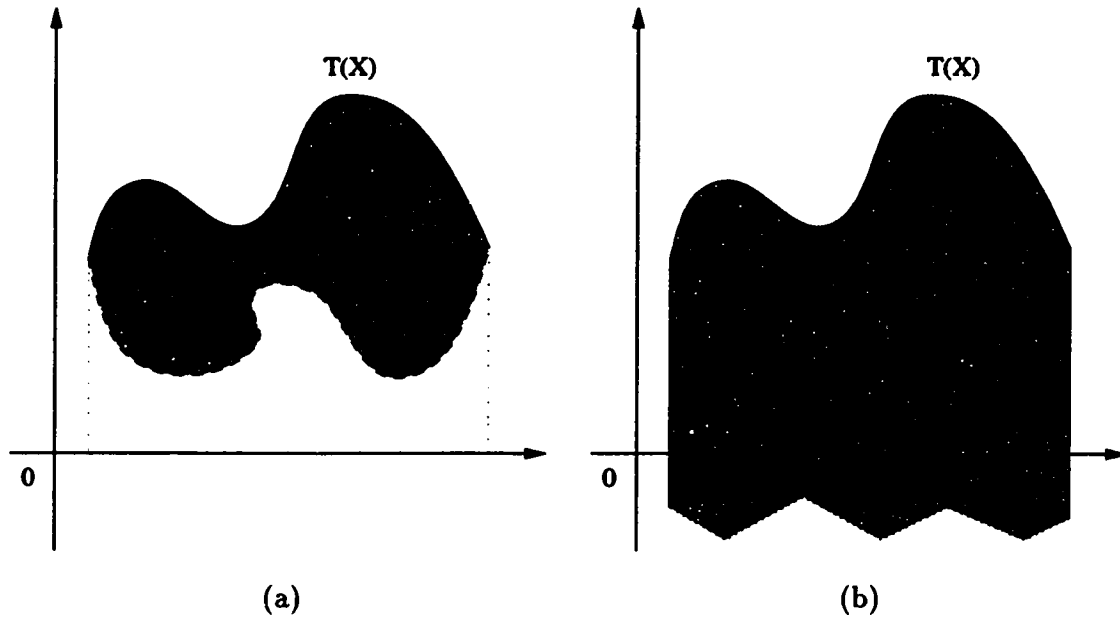


Figure A.12: Top-surface (a) and umbra (b) transforms of set  $X$

$$\text{Closing: } X \odot B = (X \oplus B) \ominus \check{B}. \quad (\text{A.45})$$

### Gray-scale morphology by minimum and maximum operators

Gray-scale erosion and dilation can also be formulated more simply if  $X$  and  $B$  themselves are boundaries. Without loss of generality, we discuss the one-dimensional gray-scale morphology. We denote the top-surface of the image as  $(x, f(x))$ , and the top-surface of the structuring element as  $(x, g(x))$ . Then the erosion of the image  $f$  by  $g$  is [Dougherty 1992]

$$(f \ominus g)(x) = \bigvee \{y : g_x + y \ll f\}, \quad (\text{A.46})$$

where  $\vee$  means maximum, and  $g \ll f$  means function  $g$  lies beneath  $f$  at all the positions, i.e.,  $g - f \leq 0$ .

Gray-scale dilation is

$$(f \oplus g)(x) = \bigwedge \{y : \check{g}_x + y \gg f\}, \quad (\text{A.47})$$

where  $\bigwedge$  means minimum,  $g \gg f$  means the function  $g$  lies above the function  $f$  at all the positions, i.e.,  $g - f \geq 0$ .  $\check{g}(x) = -g(-x)$ , i.e., the reflection of  $g(x)$ . Figure A.13 shows the gray-scale dilation and erosion in terms of minimum and maximum operations.

Gray-scale opening is then defined as

$$f \circ g = (f \ominus g) \oplus g, \quad (\text{A.48})$$

and gray-scale closing is defined as

$$\begin{aligned} f \bullet g &= (f \oplus g) \ominus g, \\ &= -[(-f) \circ (\bar{g})], \quad \text{with } \bar{g}(x) = g(-x). \end{aligned} \quad (\text{A.49})$$

The definitions in previous section are more general, and these in the present section are easier to handle with computers.

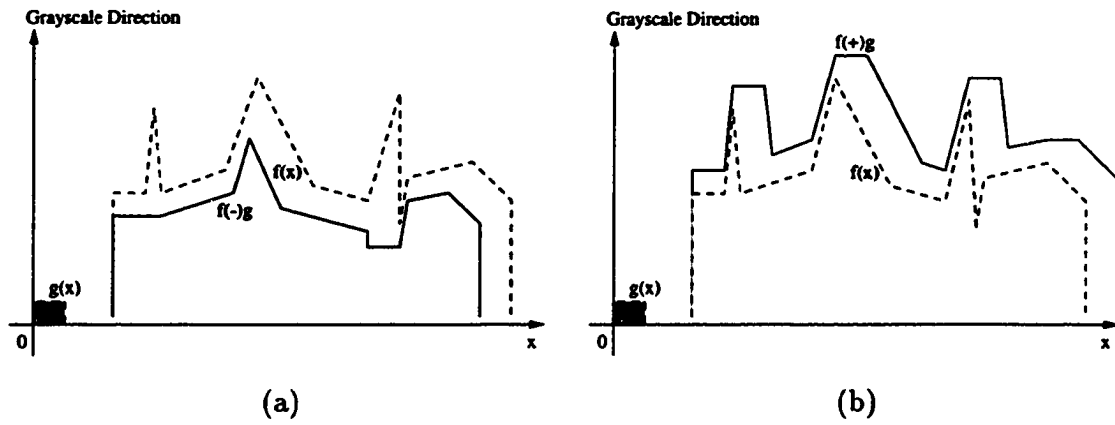


Figure A.13: Gray-scale erosion (a) and dilation (b) of  $f(x)$  by  $g(x)$

**APPENDIX B. FLUXES AND *FWHMS* FOR THE POINT AND SLIGHTLY EXTENDED SOURCES BY VARIOUS METHODS**

This appendix contains the fluxes and *FWHMs* for the point and slightly extended sources after filtering Figure 3.5 by various methods. The filtering methods involved in this dissertation are Gaussian SE sieving by equal CI area method, by non-overlapping method, by multi-cirrus filtering, and by sequential filtering, hemispherical SE sieving, cylindrical SE sieving, normal wavelet method, iterative wavelet method, and predictive wavelet method. For the morphological methods, sigmoidal cirrus weighting are imposed except for non-overlapping method and cylindrical SE sieving. The fluxes and *FWHMs* of the point and slightly extended sources for each method are listed in a table in the same format. Each table contains data in a format of 4×4 grid which corresponds spatially to the 4×4 sources in Figure 3.5. Each box in the table has four numbers which are arranged in the order of, flux of point source, *FWHM* of point source, flux of slightly extended source, and *FWHM* of slightly extended source, from top down. The tables are presented in the order of the first appearance of the methods in the dissertation.

**Table B.1:** The fluxes and FWHMs of the point and extended sources after filtering Figure 3.5 using Gaussian SEs with equal CI area method. The row and column format of the table follows the row and column grid structure of the source in Figure 3.5

<b>Flux-P</b>	65.2	64.9	65.2	62.1
<b>FWHM-P</b>	2.9	2.88	2.98	2.92
<b>Flux-F</b>	131.6	124.3	129.1	123.2
<b>FWHM-E</b>	4.86	4.72	4.76	4.67
<b>Flux-P</b>	61.2	62.0	62.3	57.1
<b>FWHM-P</b>	2.81	2.83	2.91	2.8
<b>Flux-E</b>	136.6	137.9	134.0	122.2
<b>FWHM-E</b>	4.69	4.9	4.66	4.56
<b>Flux-P</b>	59.1	59.8	60.4	58.7
<b>FWHM-P</b>	2.79	2.9	2.94	2.8
<b>Flux-E</b>	129.7	134.8	126.1	137.3
<b>FWHM-E</b>	4.7	4.71	4.62	4.77
<b>Flux-P</b>	59.5	61.4	62.0	62.3
<b>FWHM-P</b>	2.79	2.91	2.81	2.83
<b>Flux-E</b>	140.7	129.6	138.8	130.2
<b>FWHM-E</b>	4.72	4.65	4.72	4.6

**Table B.2:** The fluxes and FWHMs of the point and extended sources after filtering Figure 3.5 using Gaussian SEs with non-overlapping method

Flux-P	64.2	61.8	64.5	64.8
FWHM-P	2.90	2.88	2.98	2.92
Flux-E	140.2	131.8	137.8	131.4
FWHM-E	4.85	4.73	4.77	4.67
Flux-P	61.2	62.9	63.8	56.0
FWHM-P	2.81	2.83	2.91	2.80
Flux-E	141.8	145.4	140.3	129.6
FWHM-E	4.70	4.91	4.67	4.57
Flux-P	58.9	61.3	62.3	56.6
FWHM-P	2.79	2.90	2.94	2.80
Flux-E	141.7	142.9	132.9	145.6
FWHM-E	4.70	4.71	4.62	4.77
Flux-P	59.5	61.8	62.9	63.8
FWHM-P	2.79	2.91	2.81	2.83
Flux-E	147.9	135.9	149.6	137.6
FWHM-E	4.71	4.65	4.72	4.61

**Table B.3:** The fluxes and FWHMs of the point and extended sources after filtering Figure 3.5 using Gaussian SEs with multi-cirrus filtering

Flux-P	63.9	64.4	63.8	60.4
FWHM-P	2.86	2.87	2.94	2.83
Flux-E	127.3	120.3	124.5	119.2
FWHM-E	4.64	4.51	4.57	4.48
Flux-P	60.3	61.0	61.1	56.4
FWHM-P	2.78	2.81	2.86	2.79
Flux-E	129.5	117.9	123.1	130.2
FWHM-E	4.50	4.40	4.37	4.55
Flux-P	58.3	58.8	59.2	57.8
FWHM-P	2.76	2.84	2.83	2.80
Flux-E	121.6	131.7	136.0	124.4
FWHM-E	4.50	4.40	4.40	4.37
Flux-P	58.9	60.4	60.3	61.0
FWHM-P	2.78	2.8	2.78	2.81
Flux-E	133.8	125.3	129.5	117.9
FWHM-E	4.47	4.58	4.52	4.49

**Table B.4:** The fluxes and FWHMs of the point and extended sources after filtering Figure 3.5 using hemispherical SEs with equal CI area method

Flux-P	64.0	65.3	65.5	61.9
FWHM-P	2.86	2.88	3.00	2.91
Flux-E	114.6	111.7	115.6	117.9
FWHM-E	4.53	4.46	4.55	4.51
Flux-P	61.4	61.9	61.9	57.2
FWHM-P	2.82	2.81	2.88	2.81
Flux-E	122.0	114.2	119.0	122.5
FWHM-E	4.45	4.36	4.38	4.50
Flux-P	59.6	60.2	60.0	58.6
FWHM-P	2.80	2.87	2.84	2.83
Flux-E	118.7	129.0	128.3	120.2
FWHM-E	4.48	4.62	4.44	4.49
Flux-P	59.6	61.4	61.4	61.9
FWHM-P	2.79	2.89	2.81	2.88
Flux-E	126.0	121.5	114.2	119.0
FWHM-E	4.46	4.39	4.38	4.50

**Table B.5:** The fluxes and FWHMs of the point and extended sources after filtering Figure 3.5 using cylindrical SEs with equal CI area method

Flux-P	63.8	66.0	58.1	60.0
FWHM-P	3.06	2.94	2.99	2.94
Flux-E	173.8	163.7	165.4	171.9
FWHM-E	5.13	5.02	4.99	5.08
Flux-P	58.9	58.3	66.7	60.9
FWHM-P	2.95	2.94	2.81	3.04
Flux-E	150.1	168.9	174.9	147.0
FWHM-E	4.79	4.99	5.01	4.74
Flux-P	62.7	66.6	58.2	60.9
FWHM-P	3.03	2.97	2.92	2.98
Flux-E	173.8	163.0	165.7	171.2
FWHM-E	5.21	5.07	4.95	5.01
Flux-P	60.9	58.0	58.5	66.2
FWHM-P	2.94	2.96	2.85	3.07
Flux-E	150.1	168.3	174.2	147.9
FWHM-E	4.93	4.79	5.11	4.81

**Table B.6:** The fluxes and FWHMs of the point and extended sources after filtering Figure 3.5 using Gaussian SEs with sequential sieving

Flux-P	61.5	63.5	60.7	59.0
FWHM-P	2.84	2.85	2.89	2.83
Flux-E	99.4	100.0	106.8	109.6
FWHM-E	4.24	4.27	4.36	4.36
Flux-P	58.8	59.2	61.4	54.9
FWHM-P	2.79	2.80	2.88	2.77
Flux-E	113.1	104.6	116.2	112.3
FWHM-E	4.28	4.21	4.33	4.33
Flux-P	56.5	56.9	57.8	56.4
FWHM-P	2.75	2.80	2.80	2.79
Flux-E	101.2	122.9	124.2	115.7
FWHM-E	4.20	4.46	4.36	4.37
Flux-P	57.7	58.6	59.3	61.0
FWHM-P	2.78	2.81	2.89	2.83
Flux-E	117.9	109.1	113.1	104.6
FWHM-E	4.31	4.19	4.28	4.21

**Table B.7:** The fluxes and FWHMs of the point and extended sources after filtering Figure 3.5 using normal wavelet method

Flux-P	47.9	47.3	54.6	53.3
FWHM-P	2.73	2.84	2.79	2.97
Flux-E	94.3	98.3	103.0	106.3
FWHM-E	4.47	4.58	4.44	4.46
Flux-P	53.5	50.6	53.8	54.0
FWHM-P	2.75	2.93	2.80	2.81
Flux-E	103.5	106.4	100.9	110.3
FWHM-E	4.43	4.64	4.47	4.41
Flux-P	54.3	53.7	50.2	53.1
FWHM-P	2.91	2.73	3.07	2.81
Flux-E	110.9	108.7	99.9	107.1
FWHM-E	4.49	4.46	4.48	4.44
Flux-P	47.6	54.4	53.8	50.2
FWHM-P	2.73	3.05	2.82	2.73
Flux-E	98.5	102.5	106.8	100.1
FWHM-E	4.43	4.47	4.42	4.68

**Table B.8:** The fluxes and FWHMs of the point and extended sources after filtering Figure 3.5 using iterative wavelet method

Flux-P	40.4	48.2	39.4	44.9
FWHM-P	2.82	2.92	2.91	2.79
Flux-E	83.1	81.0	84.7	75.1
FWHM-E	4.63	4.46	4.52	4.42
Flux-P	39.7	44.5	39.3	41.4
FWHM-P	2.97	2.81	2.75	2.80
Flux-E	84.3	75.7	94.8	89.6
FWHM-E	4.43	4.52	4.70	4.47
Flux-P	39.9	41.3	47.4	46.0
FWHM-P	2.79	2.83	3.05	2.92
Flux-E	81.3	85.5	76.3	95.0
FWHM-E	4.42	4.68	4.45	4.49
Flux-P	46.4	47.0	43.4	47.5
FWHM-P	3.01	2.89	2.82	2.93
Flux-E	75.5	94.2	89.3	86.0
FWHM-E	4.59	4.40	4.63	4.39

**Table B.9:** The fluxes and FWHMs of the point and extended sources after filtering Figure 3.5 using predictive wavelet method

Flux-P	50.2	62.2	47.4	51.9
FWHM-P	2.86	2.97	2.90	2.75
Flux-E	121.5	127.6	139.7	137.7
FWHM-E	4.74	4.73	4.94	4.77
Flux-P	45.4	52.9	50.1	56.5
FWHM-P	2.73	2.82	2.89	2.91
Flux-E	135.7	120.3	148.4	130.6
FWHM-E	4.76	4.65	4.79	4.72
Flux-P	52.9	49.2	56.5	58.5
FWHM-P	2.76	2.79	2.92	2.95
Flux-E	144.7	123.3	122.7	126.6
FWHM-E	4.81	4.58	4.64	4.83
Flux-P	63.5	46.9	49.2	57.7
FWHM-P	2.83	2.92	2.93	2.99
Flux-E	138.7	138.7	136.7	121.3
FWHM-E	4.96	4.87	4.79	4.76

**BIBLIOGRAPHY**

- Allen, D. A., 1975, *Infrared: the New Astronomy*, Keith Reid Ltd., Devon, England.
- Appleton, P. N., Siqueira, P. R., and Basart, J. P., 1993, "A morphological filter for removing 'cirrus-like' emission from far-infrared extra-galactic IRAS fields," *Astronomical Journal*, vol. 106, p. 1664.
- Aumann, H. H., Fowler, J. W., Melnyk, M., 1990, "A maximum correlation method for image construction of IRAS survey data," *Astronomical Journal*, vol. 99, p. 1674.
- Bain, L. J., and Engelhardt, M., 1992, *Introduction to Probability and Mathematical Statistics*, PWS-KENT Publishing, Boston.
- Ball, G. H. and Hall D. J., 1965, "ISODATA, a novel method of data analysis and pattern classification," *Stanford Research Institute Technical Report*, Stanford, California.
- Barnsley, M., 1993, *Fractals Everywhere*, Academic, San Diego.
- Batchelor, B. G., 1974, *Practical Approach to Pattern Classification*, Plenum Press, London and New York.
- Beichman, C. A., *et al.*, 1988, *Infrared Astronomical Satellite (IRAS) Catalogs and Atlases*, Scientific and Technical Information Division, National Aeronautics and Space Administration, Washington, DC
- Bhattacharya, P., Zhu, W., and Qian, K., 1995, "Shape recognition method using morphological hit-or-miss transform," *Optical Engineering*, vol. 34, p. 1718.
- Bok, B. J., and Bok, P. F., 1981, *The Milky Way*, Harvard University Press, Cambridge.

- Bontekoe, T.J. R., 1990, "Image construction from the IRAS survey and data fusion," Presented at the *Workshop on Restoration of HST Images and Spectra*, Baltimore, MD, 21-22 Aug. 1990.
- Boulanger, F., and van Albada, G. D., 1985, "Warm dust in the neutral interstellar medium," *Astrophysics and Astronomy*, vol. 144, p. L9.
- Charif-Chefchaoui, M., and Schonfeld, D., 1993, "Morphological bounds on order-statistics filters," *Proc. Soc. Photo-Opt. Instrum. Eng.*, vol. 2030, p. 24.
- Chen, Y., and Dougherty, E. R., 1994, "Gray-scale morphological granulometric texture classification," *Optical Engineering*, vol. 33, p. 2713.
- Chester, T., 1986, "A statistical analysis and overview of the IRAS Point Source Catalog (IR)," *Light on Dark Matters*, F. P. Israel, ed., D. Riedel Publishing, Boston, p. 3.
- Chui, C. K., 1992a, *An Introduction to Wavelets*, Academic, San Diego.
- Chui, C. K., ed., 1992b, *Wavelets: A Tutorial in Theory and Applications*, Academic, San Diego.
- Chui, C. K., Montefusco, L., and Puccio, L., eds., 1994, *Wavelets: Theory, Algorithms, and Applications*, Academic, San Diego.
- Cline, W. M., 1984, "Wavelet composition program useful when cyclical fluctuations must be evaluated," *Oil & Gas Journal*, vol. 82 (Dec. 3 '84), p. 93.
- Cox, P., and Mezger, P. G., 1987, "The origin of the diffuse galactic IR/Submm emission: revisited after IRAS," *Star Formation in Galaxies*, NASA Conference Publication 2466. NASA, Washington D. C.
- David, L., Dooling, D., 1984, "The infrared universe," *Space World*, vol. U-2-242, p. 4.
- Desert, F. X., Bazell, D., Boulanger, F., 1988, "An all-sky search for molecular cirrus clouds", *Astrophysical Journal*, vol. 334, p. 815.
- Dougherty, E. R., 1992, *An Introduction to Morphological Image Processing*, SPIE, Bellingham, Washington.

- Dougherty, E. R., Gader, P. D., and Serra, J. C., eds., 1993, *Image Algebra and Morphological Image Processing IV*, 12-13, July, 1993, San Diego, California, SPIE Proc. vol. 2030, SPIE, Bellingham, Wash., USA.
- Dougherty, E. R., and Serra, J. C., eds., 1992, *Image Algebra and Morphological Image Processing III*, July, 1992, San Diego, California, SPIE Proc. vol. 1769, SPIE, Bellingham, Wash., USA.
- Duda, R. O., and Hart, P. E., 1973, *Pattern Classification and Scene Analysis*, John Wiley & Sons, New York.
- Dunford, N., and Schwartz, J. T., 1958, *Linear Operators, Part I: General Theory*, Interscience Publishers, Inc., New York.
- Egger, O., Li, W., and Kunt, M., 1995, "High compression image coding using an adaptive morphological subband decomposition," *Proceedings of the IEEE*, vol. 83, p. 272.
- Elliott, R. S., 1993, *Electromagnetics: History, Theory, and Applications*, IEEE Press, Piscataway, New Jersey.
- Foufoula-Georgious, E., and Kumar, P., eds., 1994, *Wavelets in Geophysics*, Academic, San Diego.
- Gabor, D., 1946, "Theory of communication," *J. IEE (London)*, vol. 93, p. 429.
- Gader, P. D., ed., 1990, *Image Algebra and Morphological Image Processing*, 10-12, July, 1990, San Diego, California, SPIE Proc. vol. 1350, SPIE, Bellingham, Wash., USA.
- Gader, P. D., and Dougherty, E. R., eds., 1991, *Image Algebra and Morphological Image Processing II*, July, 1991, San Diego, California, SPIE Proc. vol. 1568, SPIE, Bellingham, Wash., USA.
- Geman, S., and Geman, D., 1984, "Stochastic relaxation, Gibbs distribution, and the Bayesian restoration of images," *IEEE Trans. on Pattern Analysis and Machine Intelli.*, vol. PAMI-6, no. 6, p. 721.
- Giardina, C. R., and Dougherty, E. R., 1988, *Morphological Methods in Signal and Image Processing*, Prentice Hall, Englewood Cliffs, New Jersey.

- Goldberg, R. R., 1965, *Fourier Transform*, Cambridge University Press, Cambridge.
- Gonsalves, R. A., Lyons, T. D., Price, S. D., Levan, P. D., Aumann, H. H., 1987, "Infrared Astronomical Satellite (IRAS) image reconstruction and restoration," *Advances in Image Processing, Proceedings of the Meeting, The Hague, Netherlands, Mar. 31-Apr. 3, 1987 (A88-50319 21-35)*, Bellingham, WA, Society of Photo-Optical Instrumentation Engineers, 1987, p. 16.
- Goupillaud P., Grossmann, A., and Morlet, J., "Cycle-octave and related transforms in seismic signal analysis," *Geoexploration*, vol. 23, 1984/1985, p. 85.
- Grosbol, P., Harten, R. H., Greisen, E. W., Wells, D. C., 1988, "Generalized extensions and blocking factors for FITS," *Astronomy and Astrophysics Suppl. Series*, vol. 73, p. 359.
- Grossmann, A., and Morlet J., 1984, "Decomposition of Hardy functions into square integrable wavelets of constant shape," *SIAM J. Math. Anal.*, vol. 15, p. 723.
- Hadwiger, H., 1957, *Vorlesungen uber Inhalt, Oberflache und Isoperimetrie*, Springer-Verlag, Berlin.
- Han, K. S., 1980, "IR signal processing under zodiacal light background," *Infrared Image Sensor Technology*, Proceedings of the Seminar, Washington, DC, April 8-9, 1980, Bellingham, WA, Society of Photo-Optical Instrumentation Engineers, 1980, p. 131.
- Harten, R. H., Grosbol, P., Greisen, E. W., Wells, D. C., "The FITS tables extension," 1988, *Astronomy and Astrophysics Suppl. Series*, vol. 73, p. 365.
- Hausdorff, F., 1978, *Set Theory*, Chelsea Publishing, New York.
- He, L. X., Appleton, P. N., and Basart, J. P., 1994a, "Designing morphological filter for removing 'cirrus' emission from far-IR extra-galactic IRAS fields," *Proc. 3rd Annual Midwest Electro-Technology Conf.*, p 43-46.
- He, L. X., Basart, J. P., Appleton, P. N., and Pedelty, J. A., 1995, "A self-consistent mathematical morphological filter for removing 'cirrus' noise from far-infrared astronomical images," *Neural, Morphological, and Stochastic Methods in Image and Signal Processing*, Sylvia S. Shen, Edward R. Dougherty, Francoise Preteux, Editors, SPIE Proc. vol. 2568, p. 104.

- He, L. X., Hsu, D. K., and Basart, J. P., 1994b, "Extraction of void fraction in metal matrix composite using morphological image processing," *Advanced Composite Letters*, vol. 3, p. 51.
- Heijmans, H. J. A. M., 1994, *Morphological image operators*, Academic Press, New York.
- Heijmans, H. J. A. M., and Toet, A., 1991, "Morphological sampling," *CVGIP: Image Understanding*, vol. 54, p. 384.
- Hemdal, J. F., Loughheed, R. M., 1991, "Morphological approaches to the automatic extraction of phonetic features," *IEEE Transactions on Signal Processing*, vol. 39, p. 490.
- Hrbacek, K., and Jech, T., 1978, *Introduction to Set Theory*, Marcel Dekker, Inc., New York.
- Jackson, J. D., 1975, *Classical Electromagnetics*, New York, Wiley.
- Kaufmann, W. J. III., 1978, *Stars and Nebulas*, W. H. Freeman, San Francisco.
- Kaufmann, W. J. III., 1979, *Galaxies and Quasars*, W. H. Freeman, San Francisco.
- Kaufmann, W. J. III., 1985, *Universe*, W. H. Freeman, New York.
- Khalil, H. K., 1992, *Nonlinear Systems*, Macmillan Publishing Company, New York.
- Kraan-Korteweg, R. C., Loan, A. J., Burton, W. B., Lahav, O., Ferguson, H.C., Henning, P.A., and Lynden-Bell, D., 1994, *Nature*, vol. 372, p. 77.
- Lantuejoul, C., and Serra, J., 1982, "M-filters," *Proc. 1982 IEEE Int. Conf. Acoust., Speech, Signal Processing*, Paris, p. 2063.
- Lazear, G. D., 1984, "An examination of the exponential decay method of mixed-phase wavelet estimation," *Geophysics*, vol. 49, p. 2094.
- Liang, S. Ahmadi, M., and Shridhar, M., 1994, "A morphological approach to text string extraction from regular periodic overlapping text/background images," *CVGIP: Graphical Models and Image Processing*, vol. 56, p. 402.
- Lippmann, R. P., 1987, "An introduction to computing with neural nets," *IEEE ASSP Magazine*, April, p. 4.

- Low, F. J., *et al.*, 1984, "Infrared cirrus: new components of the extended emission," *Astrophys. Journal*, vol. 278, p. L19.
- MacQueen, J., 1967, "Some methods for classification and analysis of multivariate observations," *Proc. Fifth Berkeley Symposium on Math Stat. and Prob.*, I., Berkeley and Los Angeles, Calif.
- Mallet, S., 1989, "A theory of multi-resolution signal decomposition: the wavelet representation," *IEEE Trans. Patt. Anal. Mach. Intell.*, vol. PAMI-11, p. 674.
- Maragos, P., 1986, "Tutorial on advances in morphological image processing and analysis," *Proc. SPIE, Vis. Commun. Image Processing*, vol. 707, p. 64.
- Maragos, P., 1989, "A representation theory for morphological image and signal processing," *IEEE Trans. Patt. Anal. Mach. Intell.* vol. PAMI-11, p. 701.
- Maragos, P., and Schafer, R. W., 1986, "Applications of morphological filtering to image processing and analysis," *Proc. 1986 IEEE Int. Conf. Acoust., Speech, Signal Processing*, Tokyo, Japan, p. 2067.
- Maragos, P., and Schafer, R. W., 1987, "Morphological filters - part I: their set-theoretic analysis and relations to linear shift-invariant filters," *IEEE Trans. Acoust., Speech, Signal Processing*, vol. ASSP-35, p. 1153.
- Maragos, P., and Schafer, R. W., 1987, "Morphological filters - part II: their relations to median, order-statistics, and stack filters," *IEEE Trans. Acoust., Speech, Signal Processing*, vol. ASSP-35, p. 1170.
- Maragos, P., and Sun, F.-K., 1993, "Measuring the fractal dimension of signals: morphological covers and iterative optimization," *IEEE Transactions on Signal Processing*, vol. 41, p.108.
- Maragos, P. A., 1985, "A unified theory of translation-invariant systems with applications to morphological analysis and coding of images," *Ph. D. Dissertation*, School of Electrical Engineering, Georgia Institute of Technology, Atlanta, GA.
- Matheron, G., 1975, *Random Sets and Integral Geometry*, Wiley, New York.
- Minkowski, H., 1903, "Volume und oberflache," *Math. Annalen.*, vol. 57, p. 447.

- Neugebauer, G., *et al.*, 1984a, "Infrared astronomical satellite (IRAS) mission," *Astrophysical Journal*, vol. 278, p. L1.
- Neugebauer, G., *et al.*, 1984b, "Early results from the Infrared Astronomical Satellite", *Science*, vol. 224, p. 14.
- Newman, B., J., 1986, "Deconvolution of noisy seismic data - a method for prestack wavelet extraction," *Geophysics*, vol. 51, p. 34.
- Nyquist, H., 1928, "Certain topics in telegraph transmission theory," *AIEE Trans.*, p. 617.
- Oppenheim, A. V., and Schaffer, R. W., 1989, *Discrete-time Signal Processing*, Prentice, Englewood Cliffs, New Jersey.
- Pai, T.-W., and Hansen, J. H. L., 1994, "Boundary-constrained morphological skeleton minimization and skeleton reconstruction," *IEEE Transactions on Pattern Analysis and Machine Intelligence*, vol. 16, p. 201.
- Pal S. K. and Majumder D. K. D., 1986, *Fuzzy Mathematical Approach to Pattern Recognition*, Wiley, New York.
- Percival, D. B., and Walden, A. T., 1993, *Spectral Analysis for Physical Applications*, Cambridge University Press, London.
- Pratt, W. K., 1991, *Digital Image Processing*, Wiley, New York.
- Preston, K., Jr., 1983, "Ξ-filters," *IEEE Trans. Acoust., Speech, Signal Processing*, vol. ASSP-31 (Aug.), p. 861.
- Puget, J. L., Perault, M., Boulanger, F., and Falgarone, E., 1987, "Diffuse infrared emission of the galaxy: large scale properties," *Star Formation in Galaxies*, NASA Conference Publication 2466, NASA, Washington D. C.
- Rose, K., Gurewitz, E., and Fox, G. C., 1993, "Constrained clustering as an optimization method," *IEEE Trans. on Patt. Anal. Mach. Intell.*, vol. PAMI-15, p. 785.
- Salembier, P., Torres, L., and Meyer, F., 1995, "Region-based video coding using mathematical morphology," *Proceedings of the IEEE*, vol. 83, p. 843.

- Schonfeld, D., 1994, "Optimal structuring elements for the morphological pattern restoration of binary images," *IEEE Transactions on Pattern Analysis and Machine Intelligence*, vol. 16. p. 589.
- Schumaker, L. L., and Webb, G., eds., 1994, *Recent Advances in Wavelet Analysis*, Academic, San Diego.
- Serra, J., 1982, *Image Analysis and Mathematical Morphology*, Academic, New York.
- Serra, J., (ed.), 1988, *Image Analysis and Mathematical Morphology*, vol. 2, Academic Press, New York.
- Shen, S. S., Dougherty, E. R., Preteux F., eds., *Neural, Morphological, and Stochastic Methods in Image and Signal Processing*, SPIE Proc. vol. 2568, SPIE, Bellingham, Wash., USA.
- Shtivelman, V. L. D., 1988, "Source wavelet estimation by upward extrapolation," *Geophysics*, vol. 53, p. 158.
- Siqueira, P. R., 1989, "Signal and image processing in astronomy using gray-scale morphology, phase corrections, and the maximum entropy method," Thesis, Iowa State University, Ames, Iowa.
- Stein, E. M., and Weiss, G., 1971, *Introduction to Fourier Analysis on Euclidean Spaces*, Princeton University Press, Princeton, New Jersey.
- Stone, D. G., 1984, "Wavelet estimation," *Proceedings of IEEE*, vol. 72, p. 1394.
- Therrien, C. W., 1989, *Decision Estimation and Classification*, Wiley, New York.
- Thomas, J. E., 1986, "Multichannel estimation of the seismic wavelet," *Geophysics*, vol. 51, p. 838.
- Wheelock, S. L., et al., 1994a, *IRAS Sky Survey Atlas: Explanatory Supplement*, National Aeronautics and Space Administration, Jet Propulsion Laboratory, California Institute of Technology, Pasadena, California.
- Wheelock, S. L., et al., 1994b, *IRAS Sky Survey Atlas (CD-ROM)*, vol. 2, CD0 and CD1, National Aeronautics and Space Administration, Jet Propulsion Laboratory, California Institute of Technology, Pasadena, California.

Yager R. R. and Zadeh L. A., 1992, *An Introduction to Fuzzy Logic Applications in Intelligent Systems*, Kluwer Academic, Boston.

Zadeh, L. A., 1965, "Fuzzy sets," *Information and Control*, vol. 8, p. 338.